

Politecnico di Torino

Master of Science in Mechanical Engineering A.Y. 2024/2025 Graduation Session October 2025

Machine Learning-Based Optimization of a Quad-Finger Energy Harvester Design

Supervisor: Candidate:

Prof. Eugenio Brusa

Laura Pesaresi

Supervisors at University of Groningen:

Dr. Mahmoud Askari

Prof. Maryam Ghandchi Tehrani

Acknowledgements

I would like to express my deepest gratitude to Prof. Eugenio Brusa, Prof.ssa Maryam Ghandchi Tehrani and Dr. Mahmoud Askari, who offered me the exciting opportunity to contribute to this research work. Your constant support, helpfulness, and valuable advice guided me at every step of the journey, allowing me to successfully complete this work.

To the entire Dynamic and Vibration Research Unit of the university of Groningen, who warmly welcomed me and always made me feel as a member of the research group.

To my parents, the pillars of strength in my life, who have always supported me with love and pride, bringing serenity and gratification to each step on the way.

To my sister, my greatest source of inspiration and my right-hand partner in the most important decisions in life. Thank you for your constant support, even when physical distance separates us, always managing to make it appear as if none exists.

To my grandparents, both those who are still with me and those who look over me, for never failing to make me feel their pride and warmth.

To my lifelong friends, with whom I am tied by indissoluble and lasting bonds. In particular to Caterina and Lorenzo, who have been sharing everything since childhood; to "API"; and to my high school classmates, who are still part of my life. Each of you, in your own way, has brought joy and genuine friendship into my life, while also teaching me determination, discipline, and dedication in my studies, constantly inspiring me to do my best.

To my friends in Turin, who in such a short time have made this city my second home.

To my study partner since my bachelor's degree, Veronica. Thank you for showing me that working through difficulties together makes everything seem easier and more achievable.

Finally, to Enrico, with whom I have grown and shared every milestone. Much of my personal growth and the confidence I have gained along this journey is thanks to you. You make me feel that every success of mine is also yours, and vice versa. Looking forward to building many more future achievements side by side.

Laura Pesaresi

Abstract

The growing development of electronic devices and the need for sustainable energy solutions have stimulated research into alternatives to traditional batteries. In this context, piezoelectric energy harvesters (PEHs) represent a promising technology, capable of converting environmental vibrations into electrical energy to supply low-power devices. However, PEH performance significantly depends on geometry and electrical parameters, and since traditional optimization based on Finite Element (FE) models involves very high computational costs, more efficient strategies are developed. To address this, the thesis proposes a hybrid approach combining machine learning models with genetic algorithms for the optimization of the geometric and electrical parameters of a Quad-Finger multimodal energy harvester. Both single-output and multi-output datasets, generated by an experimentally validated FE model, are used to train three supervised regression models: Random Forest Regression (RFR), Gradient Boosting Regression Tree (GBRT), and Extreme Gradient Boosting Regression (XGBR). After validation, the ML models are integrated with a genetic algorithm to develop a fully data-driven optimization process. Among the models evaluated, GBRT shows the highest predictive accuracy. Overall, the proposed methodology not only ensures reliable response prediction for different harvester configurations, but also refines the design parameters to enhance power extraction.

Contents

Li	st of	Figures	IV		
Li	List of Tables				
1	Inti	roduction	1		
2	Sys	tem Modeling	5		
	2.1	Smart Structures and Smart Materials	5		
	2.2	Piezoelectric Materials	8		
	2.3	Energy Harvesters	15		
	2.4	Piezoelectric-Based Energy Harvesters	18		
		2.4.1 Energy Condition Circuits	23		
		2.4.2 Experimental Setup	25		
	2.5	Starting Piezoelectric Harvesting Structure	26		
	2.6	Machine Learning	31		
		2.6.1 Data Preparation for Machine Learning Models	33		
	2.7	Ensemble Supervised Algorithms	35		
		2.7.1 Random Forest Regression RFR	35		
		2.7.2 Gradient Boosting Regression Tree GBRT	37		
		2.7.3 Extreme Gradient Boosting Regression XGBR	38		
	2.8	Optimization Problem	39		
		2.8.1 Optimal Design	39		
		2.8.2 Genetic Algorithm	40		
	2.9	Related Work	42		
		2.9.1 Structural Validation of the Energy Harvester	42		
		2.9.2 Machine Learning for Energy Harvester Optimization	42		
		2.9.3 Genetic Algorithms Combined with Machine Learning Techniques	43		
3	Ma	in Contribution of the Thesis	45		
	3.1	First Approach: Optimization of beam lengths only with excitation fre-			
		quencies sweep	46		
	3.2	Second Approach: Optimization with discrete excitation frequencies and			
		load resistance sweep	47		
	3.3	Third Approach: Multimodal optimization with the introduction of beam			
		distances and all modes	48		

	3.4	Validation of the Hybrid Optimization Model	48
4	Exp	perimental versus Numerical Validation	51
	4.1	First Approach: Optimization of beam lengths only with excitation fre-	
		quencies sweep	51
		4.1.1 Methodology	51
		4.1.2 Numerical Results	56
	4.2	Second Approach: Optimization with discrete excitation frequencies and	
		load resistance sweep	60
		4.2.1 Methodology	60
		4.2.2 Numerical Results	63
	4.3	Third Approach: Multimodal optimization with the introduction of beam	
		distances and all modes	73
		4.3.1 Methodology	73
		4.3.2 Numerical Results	77
	4.4	Validation of the Hybrid Optimization Model	101
		4.4.1 Methodology	101
		4.4.2 Numerical Results	103
5	Con	aclusion 1	.09
B	ibliog	graphy 1	13

List of Figures

2.1	Smart Structures in a set-based diagram [31]
2.2	Poling process: (a) randomly oriented dipoles, (b) alignment under an
	external electric field, (c) stable orientation of dipoles after poling. [37] .
2.3	Resulting polarization versus electric field: typical hysteretic cycle of a
	piezoelectric material [46]
2.4	Longitudinal strain versus electric field diagram of piezoelectric materials
	$[46]. \ldots \ldots$
2.5	Phase diagram of lead zirconate - lead titanate compounds [27] 1
2.6	MFC composition [6]
2.7	Classification of energy harvesting [27] 1
2.8	Energy harvesters based on mechanical motion. Reproduced from [5,7,12,
	14, 15, 19, 20]
2.9	PEH applications. Reproduced from [7]
2.10	1 01 00 [1
	Unimorph cantilever energy harvester [8]
2.12	Unimorph energy harvester electrical circuit model [7]
2.13	Bimorph PZT cantilever beam
2.14	Piezoelectric bimorphs configurations: (a) Inward series bimorph, (b) out-
	ward series bimorph, (c) parallel bimorph, (d) heterogeneous bimorph [45] 2
2.15	Geometrical improvements [38] [8]
2.16	Piezoelectric energy harvester with a simple resistor [6]
2.17	Read-out circuit for a single generator [6]
2.18	Series and Parallel connections [36]
2.19	Schematic diagram of the experimental setup [6]
2.20	MFC microstructure [6]
2.21	MFC-based Quad-Finger multi-modal energy harvester [6] 2
2.22	Power management circuit of the structure under study
2.23	Fabricated prototype of the starting structure
2.24	AI classification [52]
2.25	ML classification [52]
2.26	RL scheme [52]
2.27	Train/Test split [52]
2.28	Decision tree scheme
2.29	RFR flowchart [47]

	L 1	37 40
3.1	Optimization procedure flowchart adapted from [10]	46
4.1	Actual versus Predicted values comparison of a part of test set: (a) RFR model, (b) GBRT model, (c) XGBR model	57
4.2	First approach: Evolution of the best fitness value across genetic algorithm	59
4.3		63
4.4	Stress distribution and vibration pattern at first eigenfrequency for config-	65
4.5		66
4.6	•	67
4.7	•	67
4.8	•	68
4.9	•	68
4.10		68
4.11	Second approach: Evolution of the best fitness value across genetic algo-	70
4.12	Optimized geometry obtained with the second approach, corresponding to the maximum predicted power output using the GBRT-based genetic	
		71
4.13	Von Mises stress distribution of the optimized configuration (Second ap-	71
4.14	Exploratory data analysis of beam length variables $(L_1 \text{ to } L_4)$, showing	79
4.15	Exploratory data analysis of inter-beam distance variables (d_1, d_2, d_3) ,	80
4.16	Exploratory data analysis of resistive load values, highlighting the distri-	81
4.17	Exploratory data analysis of P_{tot} , highlighting the distribution with mean	81
4.18		83
		83
	• • • •	84
		84
		85
		85
		86
	Third approach: Evolution of the best fitness value across genetic algo-	88
4.26	P_{tot} versus Resistive load of the optimized structure : vertical axis is P_{tot} expressed in mW and horizontal axis represents the resistive load R ex-	89

4.27	Geometrical configuration of the energy harvester obtained by modifying	
	the structure obtained with the third approach optimization	92
4.28	Comparison between extracted power curves of the modified final structure	
	(a) and the starting structure (b)	93
4.29	Mode shapes of the modified structure: first and second eigenfrequencies.	95
4.30	Mode shapes of the modified structure: third and fourth eigenfrequencies.	96
4.31	Von Mises stress distribution of the modified configuration when excited	
	at its first eigenfrequency.	99
4.32	Feature importance for the Gradient Boosting Regressor (multi-output)	
	trained with reduced dataset	100
4.33	Fitness history of the simplified traditional optimization	103
4.34	Extracted power versus resistive load diagram of the optimized structure.	104
4.35	Fitness history of the traditional optimization without "injection"	105
4.36	Symmetry detection in genetic algorithm generations. Horizontal axis rep-	
	resents the number of generation within the genetic algorithm. Vertical	
	axis represent the percentage of symmetric individuals with respect to the	
	total number of individuals within the generation	106
4.37	Fitness history of the final traditional optimization algorithm	107

List of Tables

2.1	Smart materials [22]	7
2.2	Different piezoelectric materials [11]	8
2.3	Piezoelectric materials and their properties [55]	14
2.4	Geometrical parameters of the starting structure [6]	28
2.5	Mechanical and electrical properties of components' materials [6] $[17]$	29
4.1	Summary of hyperparameters used for each model [39,42]	54
4.2	First four eigenfrequencies for two extreme configurations of beam lengths.	56
4.3	R^2 scores for each ML models	56
4.4	Comparison between predicted and simulated output voltage for the optimal configuration.	58
4.5	Description of the indexes introduced during the feature engineering process.	61
4.6	Comparison of reliability metrics for the three ensemble models: Random Forest Regressor (RFR), Gradient Boosting Regression Tree (GBRT), and	cc
4 7	Extreme Gradient Boosting Regressor (XGBR)	66
4.7	Relative feature importance for the three ensemble models: Random Forest Regressor (RFR), Gradient Boosting Regression Trees (GBRT), and Extreme Gradient Boosting Regression (XGBR)	69
4.8	Comparison between the initial structure and the optimal configuration found by the genetic algorithm, showing input parameters and both the	69
4.9	predicted and simulated output power	76
4.10		77
4.11	* *	' '
	Squared Error (MSE)	82
4.12	Feature importance percentages (in %) for Random Forest Regressor (RFR), Gradient Boosting Regressor (GBRT), and XGBoost Regressor (XGBR)	
	multi-output models, rounded to two significant figures	86
4.13	Comparison between the initial and the optimized configuration using the third approach with the multi-output GBRT model. Power values refer to	0.0
	the sum of the extracted powers over the first four eigenfrequencies	88

4.14	Output powers comparison $(P_1, P_2, P_3, P_4, \text{ and } P_{tot})$ between the optimal	
	structure obtained with the Second Approach and the one obtained with	
	the Third Approach	90
4.15	Output powers $(P_1, P_2, P_3, P_4, \text{ and } P_{tot})$ of the modified structure	91
4.16	First four resonance frequencies (eigenfrequencies) of the modified and	
	starting structure, namely λ_1 , λ_2 , λ_3 and λ_4	92
4.17	Output powers $(P_1, P_2, P_3, P_4, \text{ and } P_{tot})$ of the starting structure	94
4.18	Amplitude comparison of the power versus excitation frequency curves	
	between the starting and the modified structure	97
4.19	Comparison of the power extracted from the two configurations (start-	
	ing structure and modified structure) at the eigenfrequencies of the initial	
	structure (17.9, 22.2, 25.4 and 27.9 Hz)	98
4.20	Performance metrics for multi-output GBRT model trained with a reduced	
	dataset: coefficient of determination (R^2) , Mean Absolute Error (MAE),	
	and Mean Squared Error (MSE)	99
4.21	Comparison between the optimized configuration through the use of full	
	dataset and the one that uses the reduced dataset. Power values refer to	
	the sum of the extracted powers over the first four eigenfrequencies	101
4.22	Optimization results for the simplified validation case	103
4.23	Optimization results without injection of the hybrid approach solution	105
4.24	Optimized parameters and output power from the final traditional opti-	
	mization.	107

Chapter 1

Introduction

In recent decades, there has been a rapid and constant evolution in electronic devices, which have now become essential tools in many areas: from everyday use to industrial applications and scientific research. The growing spread of these technologies has led to an increase in demand for power supply systems, particularly batteries, for portable devices, applications in hard-to-reach areas, or other situations where a direct connection to the power grid is not feasible.

In parallel with the growing use of electronic devices, there has also been a rise in concern over serious environmental issues caused by the production and disposal of batteries. Alongside these significant drawbacks, there are also other inherent limitations, such as limited life span, the need for periodic replacement or recharging, and size constraints. In critical applications, these conditions can even compromise the functionality of the device itself [30,55].

For these reasons, interest in energy harvesting devices has grown in recent years. These are systems capable of converting energy from the surrounding environment into electrical energy, reducing or even eliminating the use of traditional batteries.

Several natural energy sources can be exploited for electricity generation. An immediate and well-known example is sunlight, which is the basis for the functioning of photovoltaic panels. In addition to light radiation, thermal gradients and mechanical vibrations are also potentially feasible energy sources. In particular, the extraction of energy from environmental vibrations aims to collect and transform into electricity phenomena that would otherwise be dispersed. For this purpose, piezoelectric energy harvesters (PEHs) have become a well-established technique. Unlike solar or thermal systems, PEHs can operate continuously in environments where ambient vibrations are always present, such as near industrial machinery or structural components.

These devices exploit piezoelectric materials, which are capable of converting mechanical deformations into electrical charge thanks to their crystalline structure. A typical configuration of these systems consists of a cantilever beam coated with piezoelectric material: when the beam is placed in a vibrating body, it deforms, generating electrical energy.

PEHs are mainly suited for low-power applications typically in the microwatt to milliwatt range, which is sufficient to supply small-scale devices such as sensors [30, 55].

Nevertheless, they can be integrated into vibrating systems of very different scales, ranging from pacemakers or motors, up to large infrastructures such as bridges or buildings, where environmental vibrations would otherwise be wasted.

The variety of possible fields of applications has driven research towards the development of different structural configurations, with particular attention to the geometry, the dimensions, and the electrical parameters of the device, which directly influence performance and versatility. The simplest PEHs, based on a single cantilever, exploit only the first vibration mode and are mainly efficient when the environmental vibration frequency matches the resonance frequency of the device. However, since environmental vibrations are often random and distributed over a wide spectrum, these configurations are limited. To overcome these constraints, multimodal geometries have been developed that can exploit multiple modes of vibration of the structure, thus expanding the range of frequencies from which energy can be extracted [48].

Given the critical role of structural and electrical parameters, researchers have studied and proposed several configurations, both for single-modal and multimodal piezoelectric energy harvesters, by using analytical, numerical methods and, increasingly, finite element (FE) simulations, often conducted using commercial software such as COMSOL Multiphysics or ANSYS [30,55]. These software tools allow PEH models to be recreated and validated through experiments in order to reliably predict the electromechanical responses of the devices. In this way, it is also possible to use FE simulations to perform an optimization process with the aim of adjusting the design parameters and maximizing electrical performance, such as the power extracted or the voltage generated [41].

Although the electromechanical response of arbitrarily shaped piezoelectric devices can be reliably predicted using FE simulations, the latter are not always the most practical solution if optimization is the final goal. In fact, even if they provide accurate results, FE simulations are extremely computationally expensive. In optimization processes, where parametric sweeps or a large number of iterative simulations need to be carried out to find the optimal configurations, computation times and memory requirements become very high. This makes large-scale application difficult and limits their competitiveness in industrial contexts, where it may be necessary to identify the optimal parameters for specific operating conditions quickly.

To tackle these critical issues associated with the high computational times and costs of numerical simulations, research in recent years has been focused on using data-driven approaches for response predictions and optimizations. These methods are particularly suitable in systems characterized by non-linearity and multi-variable interactions that are difficult to model analytically. In this context, Machine Learning (ML) models are emerging as tools of great interest because, after being trained on a limited amount of data, they are able to provide reliable predictions on previously unseen data [23, 24, 43]

For vibration-based piezoelectric energy harvesters, performance of the device is a function of numerous parameters. These include geometric and operating parameters, material properties, and excitation frequency. Accurately describing the relationships between the variables using analytical models or FEM simulations can be extremely time-consuming and computationally expensive, and can also result in poor generalization over large design spaces. Therefore, ML models represent a promising alternative to traditional

methods, as they allow to predict the electromechanical response of PEHs in never-before-studied configurations while significantly reducing computational costs. Models are trained from initial datasets, which can be derived from experimental measurements or numerical simulations, which in any case require less effort than the whole optimization process from FEM alone [18].

In the context of optimization, once ML models are trained to predict outputs of interest, such as output power or voltage, those quantities can be taken as objective functions to be maximized (or minimized). However, due to the large number of variables involved, PEHs' objective function typically does not have a single maximum (or minimum) but rather multiple local minima and maxima. This makes traditional optimization algorithms ineffective, since they risk converging to suboptimal solutions. To avoid this limitation, more and more studies are turning to evolutionary algorithms, namely Genetic Algorithms (GAs). These algorithms, founded on the principles of natural selection, are distinguished by their ability to discover global maxima and minima and not get stuck in local optima [10].

This thesis fits into this background and focuses on the analysis of a Quad-Finger multimodal piezoelectric energy harvester developed and built by Askari et al. [6]. The harvester had previously been simulated with COMSOL Multiphysics and experimentally validated. The present work aims to further explore the system by developing a reliable data-driven framework to optimize the device parameters. The model is based on a hybrid approach, where a dataset is initially constructed using FE simulations and then used to train Machine Learning models, specifically Random Forest Regressor (RFR), Gradient Boosting Regression Trees (GBRT) and Extreme Gradient Boosting Regressor (XGBR), both in single-output and multi-output configurations for the final goal of predicting the power output of the device as a function of geometric and operational parameters. The most reliable trained ML model is then integrated as an objective function in a genetic algorithm (GA) whose goal is to determine the best configuration to achieve maximum extracted power.

Since no specific field of application for the device is selected, the focus of the thesis is not limited to efficiency in a particular frequency range, but rather to the general maximization of the system's energy performance with significantly less time required than optimization conducted solely through FE simulations.

To develop the hybrid model for the optimization of the Quad-Finger energy harvester, a methodological process is followed, which is described in detail in the following chapters. Briefly, the process consists of three consecutive phases: a first approach based on a simplified, single-output dataset, characterized by a reduced number of input parameters to be optimized; a second one, single-output again but considering different parameters with respect to the previous analysis; and finally, a third approach based on a multi-output dataset, with all the input parameters involved. This last step represents the overall analysis that is the subject of this work, where is taken into account the multimodal nature of the structure.

This thesis is organized as follows. Chapter 2 has the goal of presenting the starting structure for the proposed hybrid optimization process, the Quad-Finger PEH. For this purpose, the chapter provides the essential theoretical background to fully understand the

alternative approach for the optimization, first introducing the fundamental concepts related to energy harvesting and piezoelectric devices, and then discussing machine learning methodologies and genetic algorithms in greater depth. In this way, all the preliminary knowledge needed to fully understand the designed work and optimization process is provided. Finally, the chapter concludes with a review of the main related scientific works, highlighting the contributions made, the contexts of application, and the differences with respect to the approach developed in this thesis.

Chapter 3 outlines the original contribution of this thesis, presenting the methodological process followed to develop the hybrid optimization method. In particular, the three progressive approaches needed to reach the final framework are described, starting from a simplified configuration and ending with a complete multimodal analysis. Finally, a validation phase is introduced, where the reliability of the results obtained by the proposed approaches is compared to the ones obtained using traditional methods.

Chapter 4 is dedicated to the numerical and experimental evaluation of the proposed hybrid optimization framework. Each of the three approaches is presented in detail, including both the methodology and the numerical results. In particular, the methodology section details all the steps involved in creating the datasets and building the algorithms, both machine learning and genetic algorithms. In addition, an in-depth description of the validation is provided at the end of the chapter, with the aim of confirming the reliability and effectiveness of the framework developed.

Chapter 5, which concludes the thesis, summarizes the key findings and presents possible directions for future research and implementation.

Chapter 2

System Modeling

This chapter aims to provide the necessary background for an in-depth understanding of the energy harvesting design optimization process developed in this thesis. The structure of this chapter is as follows. Section 2.1 provides a general overview of smart structures and smart materials with a particular focus on piezoelectric materials in Section 2.2. Subsequently, Sections 2.3 and 2.4 explore specific types of smart structure, namely energy harvesters and, more specifically, piezoelectric energy harvesters. Section 2.5 focuses on the description of the starting piezoelectric harvester used in this study. The chapter follows with Sections 2.6, 2.7 and 2.8, respectively, introduce machine learning and the optimization problem, with a particular emphasis on the genetic algorithm. Finally, Section 2.9 presents and analyzes the scientific researches on which the alternative optimization algorithm design is based, that combine numerical simulations, machine learning techniques, and genetic algorithms in an integrated manner.

2.1 Smart Structures and Smart Materials

A smart structure (or intelligent structure) is an engineering system based on sensors, actuators, and smart materials capable of performing sensing, actuation, and signal processing in order to adapt its properties and states to environmental stimuli and changes in operational conditions [16].

Smart structures can be categorized using a set-based diagram, as shown in Figure 2.1 [31] where:

- Sensory structures have sensors distributed throughout them
- Adaptive structures have distributed actuators
- Controlled structures have both actuators and sensors and a closed-loop system linking them, so that properties or states can be modified
- Active structures are characterized by highly distributed actuators that provide structural functionality and support to the system, as they are integrated into the load-bearing system

• Smart structures are an advanced subset of active structures that not only have highly distributed actuator and sensor systems with structural functionality, but also integrate distributed control functions and computing architecture to process data, analyze environmental conditions, and autonomously adapt to changing operational demands [31].

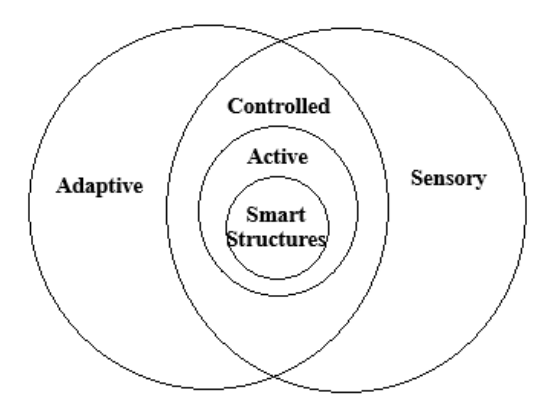


Figure 2.1: Smart Structures in a set-based diagram [31].

Since smart structures highly rely on smart materials, it is essential to provide a brief overview of these materials. Smart materials can change their composition, structure, or electrical or mechanical properties in response to various environmental conditions like temperature, magnetic fields, vibrations and so on. These materials can be used as actuators or sensors generating a certain response. Examples of such materials and the related inputs and output are provided in Table 2.1.

Smart materials offer several advantages, making them a field of increasing interest and attraction in the last few years. The advantages are the following: high energy density, fast response times, compact size and fewer moving parts. However, some limitations must be mentioned such as limited strain outputs and limited blocking forces, making them prone to damage. In addition, these materials are characterized by high cost, sensitivity to harsh environments and finally, nonlinear behavior. The latter drawback complicates the design and the control of systems, making it harder to manage and predict their responses.

Furthermore, smart materials can be categorized based on the type of coupling between mechanical and non-mechanical fields (such as electric or magnetic fields). In fact, it is possible to distinguish materials which exhibit direct or indirect coupling. Materials like piezoelectric materials, shape memory alloys, magnetostrictive ceramics, and magnetic shape memory alloys are examples of materials that demonstrate direct coupling. In these materials, either the mechanical or non-mechanical field is the input, while the other is the output. While materials such as electro-rheological fluids (ERF) and magneto-rheological fluids (MRF) demonstrate indirect coupling because there is an

intermediate link between the mechanical and non-mechanical field. In the case of ERF and MRF the variation of the electric or magnetic field leads to a changing viscosity, altering the mechanical behavior of the material.

In this overview of smart materials, piezoelectric materials play a central role due to their ability to convert mechanical strain into electrical polarization and vice versa. This property has made them particularly suitable for energy harvesting applications.

	Material Class	Excitation	Response
	Pyroelectrics	Temperature change	Electric polarization
	Piezoelectrics	Mechanical strain	Electric polarization
S	Electrostrictors	Mechanical strain	Electric polarization
SO	Magnetostrictors	Mechanical strain	Change in magnetic field
Sensors	Electroactive polymers	Mechanical strain	Electric polarization
3 2	Electroluminescent	Electric field	Light emission
	Photoluminescent	Incident light	Light emission
	Electrochromic	Electric field	Color change
	Piezoelectrics	Electric current	Mechanical strain
S	Electrostrictors	Electric current	Mechanical strain
Actuators	Magnetostrictors	Magnetic field	Mechanicl strain
na	Shape memory alloys	Temperature change	Mechanical strain
\ct	Electroactive polymers	Electric field	Mechanical strain
7	Electrorheological fluids	Electric field	Viscosity change
	Magnetorheological fluids	Magnetic field	Viscosity change

Table 2.1: Smart materials [22]

2.2 Piezoelectric Materials

The term piezoelectricity originates from the Greek word for "pressure". This is based on the fact that, in 1880, Jacques and Pierre Curie discovered that certain materials such as quartz and tourmaline generate electrical charge if subjected to pressure. This is the so-called piezoelectric effect. Shortly after, it was also discovered that applying an electric field to these materials induces mechanical deformation, a phenomenon now known as inverse piezoelectric effect.

Nowadays, the piezoelectric effect is widely used in various technological applications. The direct piezoelectric effect, also known as the generator or sensor effect, converts mechanical energy into electrical energy and is exploited in sensors and energy harvesting systems. Conversely, the inverse piezoelectric effect causes a change in length when an electric field is applied, allowing actuators to convert electrical energy into mechanical motion.

Piezoelectric materials can be classified based on their crystal structure, origin or characteristic. Firstly, piezoelectric materials can be classified based on their crystal structure into two main categories: (i) mono-crystalline materials, which are characterized by an asymmetric structure formed by a single, continuous crystal lattice. In these materials, a polar axis forms, leading to the piezoelectric effect, which occurs below the Curie temperature (TC). And (ii) polycrystalline materials made of many small crystals (the "grains") [28]. The piezoelectric effect in these materials is more pronounced compared to mono-crystalline materials. The crystals, once poled, display a strong piezoelectric response [37]. In addition, piezoelectric materials can be distinguished into natural and artificial types as highlighted by Table 2.2 [11]. Natural materials, such as quartz, ammonium, bone, and even wood, exhibit the piezoelectric effect without the need for any external treatment. On the other hand, synthetic materials are artificially fabricated through complex processes to enhance their piezoelectric properties [7].

Piezoelectric Materials						
Natural	Manmade - Inorganic (ceramics)		Manmade			
Lead based		Lead free	Organic (polymers)	Polymer composites		
Quartz Crystals	Lead titanate (PT)	Barium titanate (BT)	PVDF	PVDF/PZT		
Rochelle Salt	PZT	$KNbO_3$	P(VDF-TrFE)	PVDF/ZnO		
Topaz	PLZT	LiNbO ₃	P(VDF-TeFE)	PVDF/KNN		
Tourmaline	PMN-PT	LiTaO ₃	Nylon 11	PVDF/AgNWs		
Wood		KNN	Urea	PVDF/MWCNTs		
Silk		MoS_2	PLA	PVDF/BT NPs		
Rubber		$ZnSnO_3$	PP	PVDF-TrFE/PZT		
Dentin		Fe ₃ O ₂	Cellulose acetate	$PVDF/MoS_2$		
Bone		$ZnFe_2O_4$	Cellulose	PVDF/ZnSnO ₃		
Hair		ZnO	PAN	PVDF/Fe ₂ O ₃		
Enamel						

Table 2.2: Different piezoelectric materials [11].

Naturally, piezoelectric materials are generally isotropic and do not exhibit the dipole effect necessary for generating piezoelectricity as it is shown in Figure 2.2.(a). To make these materials macroscopically piezoelectric, a process called poling is used. This process consists of applying a strong electric field, typically several kV/mm, which causes the crystals to align their polarization direction with the external field Figure 2.2.(b). As a result, domains with a favorable orientation to the polarity field grow, while those with an unfavorable orientation shrink. After the poling process, most of the re-orientations remain even without the application of an electric field (Figure 2.2.(c)). However, a small number of domain walls may return to their original position, often due to internal mechanical stresses [37].

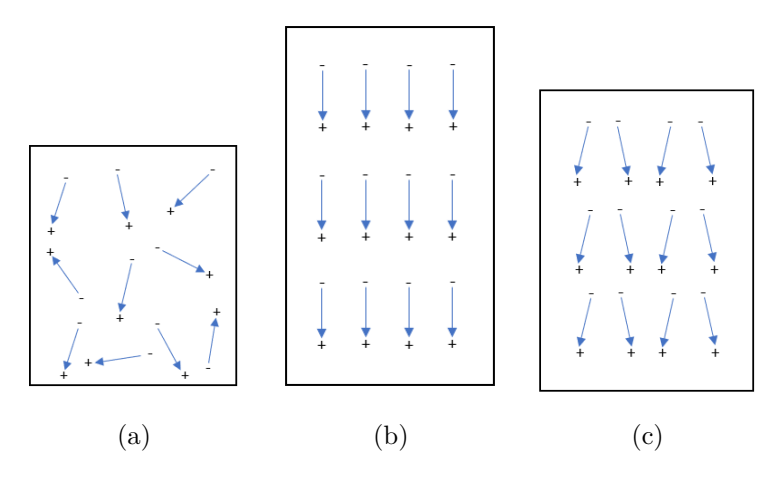


Figure 2.2: Poling process: (a) randomly oriented dipoles, (b) alignment under an external electric field, (c) stable orientation of dipoles after poling. [37]

This phenomenon results from the ferroelectric nature of piezoelectric materials. These materials are characterized by non-uniform stressed and presence of impurities that lead to limited domain wall movement, causing an hysteretic behavior when they are subjected to an electric field (shown in Figure 2.3). Indeed, if a weak field is applied, bending properties of domain walls allow a reversible movement. On the other hand, applying a stronger electric field the domain walls exhibit an irreversible translation and a permanent polarization is obtained [44]. So, once the external field is removed and an electric field, weaker than the original polarization field, is applied, the material expands and this expansion is partly caused by the piezoelectric displacement of ions within the crystal lattice, known as the intrinsic effect. The extrinsic effect, on the other hand, results from the reversible ferroelectric reorientation of the unit cells. As the strength of the applied field increases, this effect becomes more pronounced and is primarily responsible for the non-linear hysteresis [37].

Analyzing Figure 2.3, point O represent the initial isotropic condition of the material, corresponding also to the configuration of 2.2.(a). Point B, coinciding with the configuration of 2.2.(b), is the state of full polarization. Subsequently, starting diminishing the external electric field, the polarization decreases in a non-linear manner ending up with a remaining polarization at zero applied field P_s , also called saturation (or spontaneous)

polarization. Only inverting field direction is possible to remove the remaining polarization (point corresponding to the intersection between curve C-D and the horizontal axis). If negative electric field continues to increase its absolute value, symmetric behavior is shown, reaching point D (symmetric to point B in 1^{st} quadrant).

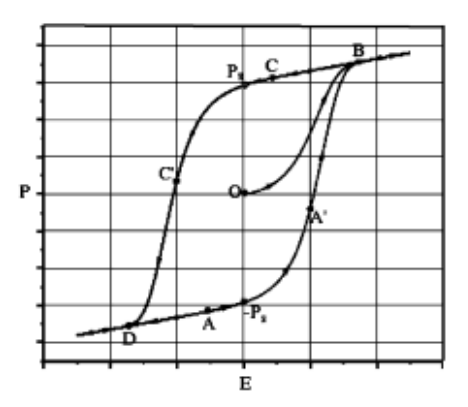


Figure 2.3: Resulting polarization versus electric field: typical hysteretic cycle of a piezo-electric material [46].

Piezoelectric materials are also characterized by a butterfly shaped diagram showing the relationship between the longitudinal strain and the electric field (shown in Figure 2.4). In that figure, the piezoelectric material linear behavior from point B to C is described. This portion describes the pure piezoelectric behavior, easily predictable and defined by a specific coefficient named the piezoelectric coefficient. The intersection between vertical axis and the curve identifies point L_s , which stands for the residual deformation at zero applied external field, also referred as remnant state. Subsequently, point C' represents the coercive field where the material shows the minimum linear deformation. After that point, as the polarization becomes negative, the strain starts growing until point D is reached. Finally, inverting the field direction again, a symmetric curve with its center of symmetry coinciding with L_s is obtained [46].

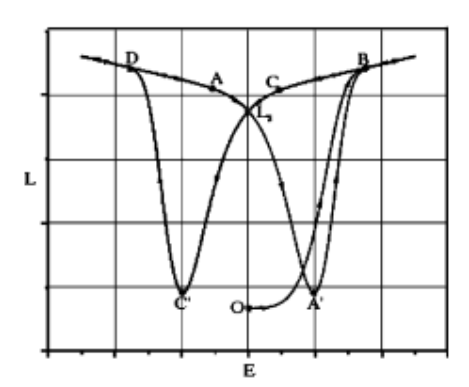


Figure 2.4: Longitudinal strain versus electric field diagram of piezoelectric materials [46].

Both direct and indirect piezoelectric effects, caused by polarized piezoelectric materials, are described by a set of constitutive equations [6]. The piezoelectric relations described by the constitutive equations and the associated symbols follow the 176-1978 - IEEE Standard on Piezoelectricity [1]. Equations 2.1 and 2.2 describe the electromechanical coupling of the indirect piezoelectric effect, specifically in the case of actuators.

$$\{\varepsilon\} = [s]^E \{\sigma\} - [d]^T \{E\}$$
(2.1)

$$\{D\} = [d] \{\sigma\} + [\epsilon]^{\sigma} \{E\}$$

$$(2.2)$$

Where ε stands for the strain field, σ for the stress field, D for the electric displacement field, and E for the electric field. The matrix s represents the compliance matrix under constant electric field conditions, while d and d^T are the electromechanical coupling coefficient matrices, accounting respectively for the direct and inverse piezoelectric effects. Finally, ϵ is the dielectric permittivity matrix under constant stress conditions.

In the case of sensing mechanism and so direct piezoelectric effect, constitutional equation changes (see Equation 2.3 and Equation 2.4).

$$\{\sigma\} = [c]\{\varepsilon\} - [e]^T\{E\}$$
(2.3)

$$\{D\} = [e] \{\varepsilon\} + [\Theta] \{E\}$$

$$(2.4)$$

Where:

$$[c] = [s]^{-1} (2.5)$$

$$[e] = [s]^{-1}[d] (2.6)$$

$$[\theta] = [s]^{-1}[d] \tag{2.7}$$

In which, matrices [c], [e] and $[\theta]$ represents respectively the stiffness, piezoelectricity and permittivity of the material.

The most produced piezoelectric materials are listed below.

Lead Zirconate Titanate (PZT) is one of the most commonly used piezoceramic materials. It is a synthetic perovskite ceramic material primarily made of lead (Pb), Zirconium (Zr) and Titanium (Ti). The addition of various dopants to the material, such as niobium (Nb), lanthanum (La), and bismuth (Bi), allows for further optimization [37]. The most common types are PZT-4, PZT-8, PZT-5A and PZT-5H and the properties are shown in Table 2.3. PZT materials offer several advantages that make them highly suitable for engineering applications. They are widely used in different range of applications such as in actuators, sensors, and energy harvesting systems [7]. Another key benefit is their customizable property, which means that they can be optimized by adjusting the zirconate-titanate ratio for specific applications. This is due to the presence of a morphotropic phase boundary (MPB) at a composition of 52% lead zirconate (as it is shown in Figure 2.5) which allows for a broad range of domain states to exist across a wide temperature spectrum [27]. In addition, PZT materials are characterized by hard and dense materials so that they can withstand high mechanical stress and environmental conditions [31], enhancing their durability. Finally, chemical inertness and relatively low manufacturing cost give to PZT materials high applicability.

However, PZT materials also exhibit certain limitations. One main drawback is their brittleness, which makes them prone to fracture under tensile strain. This limits its use in applications that involve large deformations or cyclical loads [6].

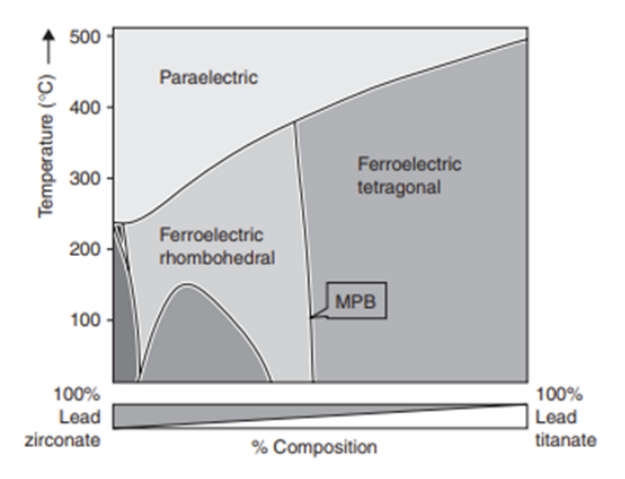


Figure 2.5: Phase diagram of lead zirconate - lead titanate compounds [27].

In addition, environmental impact due to the toxicity of lead [30] is another weak point, raising problems related to safety and disposal. Finally, above the Curie temperature, PZT loses its piezoelectric properties, which restricts its use in high-temperature applications. For many PZT-based materials, it is crucial to operate them below the Curie temperature to maintain their functionality.

Constitutive equations for PZT materials can be simplified and in particular, if they are characterized by a polarization along the z-axis, the following form is obtained [7]:

$$\begin{bmatrix} \sigma_{xy} \\ \sigma_{yy} \\ \sigma_{zz} \\ \sigma_{yz} \\ \sigma_{xz} \\ \sigma_{xy} \end{bmatrix} = \begin{bmatrix} c_{11} & c_{12} & c_{13} & 0 & 0 & 0 \\ c_{12} & c_{11} & c_{13} & 0 & 0 & 0 \\ c_{13} & c_{13} & c_{33} & 0 & 0 & 0 \\ 0 & 0 & 0 & c_{55} & 0 & 0 \\ 0 & 0 & 0 & 0 & c_{55} & 0 \\ 0 & 0 & 0 & 0 & 0 & c_{66} \end{bmatrix} \begin{bmatrix} \varepsilon_{xy} \\ \varepsilon_{yy} \\ \varepsilon_{zz} \\ \gamma_{yz} \\ \gamma_{xz} \\ \gamma_{xy} \end{bmatrix} - \begin{bmatrix} 0 & 0 & e_{33} \\ 0 & 0 & e_{31} \\ 0 & 0 & e_{31} \\ 0 & e_{15} & 0 \\ e_{15} & 0 & 0 \end{bmatrix} \begin{bmatrix} E_x \\ E_y \\ E_z \end{bmatrix}$$
(2.8)

$$\begin{bmatrix}
D_x \\
D_y \\
D_z
\end{bmatrix} = \begin{bmatrix}
0 & 0 & 0 & 0 & e_{15} & 0 \\
0 & 0 & 0 & e_{15} & 0 & 0 \\
e_{31} & e_{31} & e_{33} & 0 & 0 & 0
\end{bmatrix} \begin{bmatrix}
\varepsilon_{xy} \\
\varepsilon_{yy} \\
\varepsilon_{zz} \\
\gamma_{yz} \\
\gamma_{xz} \\
\gamma_{xy}
\end{bmatrix} + \begin{bmatrix}
\Theta_{11} & 0 & 0 \\
0 & \Theta_{11} & 0 \\
0 & 0 & \Theta_{33}
\end{bmatrix} \begin{bmatrix}
E_x \\
E_y \\
E_z
\end{bmatrix}$$
(2.9)

When polarization is oriented along the x-direction (Equations 2.10 and 2.11) or y-direction (Equations 2.12 and 2.13), the constitutive equations are modified accordingly. These can be obtained by applying appropriate transformations, such as a 90° rotation around the y-axis, followed by a 180° rotation about the z-axis for the x-polarized case [7].

$$\begin{bmatrix} \sigma_{xy} \\ \sigma_{yy} \\ \sigma_{zz} \\ \sigma_{yz} \\ \sigma_{xz} \\ \sigma_{xy} \end{bmatrix} = \begin{bmatrix} c_{33} & c_{13} & c_{13} & 0 & 0 & 0 & 0 \\ c_{13} & c_{11} & c_{12} & 0 & 0 & 0 & 0 \\ c_{13} & c_{12} & c_{11} & 0 & 0 & 0 & 0 \\ 0 & 0 & 0 & c_{66} & 0 & 0 & 0 \\ 0 & 0 & 0 & 0 & c_{55} & 0 \\ 0 & 0 & 0 & 0 & 0 & c_{55} \end{bmatrix} \begin{bmatrix} \varepsilon_{xy} \\ \varepsilon_{yy} \\ \varepsilon_{zz} \\ \gamma_{yz} \\ \gamma_{xy} \end{bmatrix} - \begin{bmatrix} e_{33} & 0 & 0 \\ e_{31} & 0 & 0 \\ 0 & 0 & e_{15} \\ 0 & e_{15} & 0 \end{bmatrix} \begin{bmatrix} E_x \\ E_y \\ E_z \end{bmatrix}$$
(2.10)

$$\begin{bmatrix} D_x \\ D_y \\ D_z \end{bmatrix} = \begin{bmatrix} e_{33} & e_{31} & e_{31} & 0 & 0 & 0 \\ 0 & 0 & 0 & 0 & 0 & e_{15} \\ 0 & 0 & 0 & 0 & e_{15} & 0 \end{bmatrix} \begin{bmatrix} \varepsilon_{xy} \\ \varepsilon_{yy} \\ \varepsilon_{zz} \\ \gamma_{yz} \\ \gamma_{xz} \\ \gamma_{xy} \end{bmatrix} + \begin{bmatrix} \Theta_{33} & 0 & 0 \\ 0 & \Theta_{11} & 0 \\ 0 & 0 & \Theta_{11} \end{bmatrix} \begin{bmatrix} E_x \\ E_y \\ E_z \end{bmatrix}$$
(2.11)

$$\begin{bmatrix} \sigma_{xy} \\ \sigma_{yy} \\ \sigma_{zz} \\ \sigma_{yz} \\ \sigma_{xz} \\ \sigma_{xz} \end{bmatrix} = \begin{bmatrix} c_{11} & c_{13} & c_{12} & 0 & 0 & 0 \\ c_{13} & c_{33} & c_{13} & 0 & 0 & 0 \\ c_{12} & c_{13} & c_{11} & 0 & 0 & 0 \\ 0 & 0 & 0 & c_{55} & 0 & 0 \\ 0 & 0 & 0 & 0 & c_{66} & 0 \\ 0 & 0 & 0 & 0 & 0 & c_{55} \end{bmatrix} \begin{bmatrix} \varepsilon_{xy} \\ \varepsilon_{yy} \\ \varepsilon_{zz} \\ \gamma_{yz} \\ \gamma_{xy} \end{bmatrix} - \begin{bmatrix} 0 & e_{31} & 0 \\ 0 & e_{33} & 0 \\ 0 & e_{31} & 0 \\ 0 & 0 & 0 & 0 \\ 0 & 0 & e_{15} \end{bmatrix} \begin{bmatrix} E_x \\ E_y \\ E_z \end{bmatrix}$$
(2.12)

$$\begin{bmatrix}
D_x \\
D_y \\
D_z
\end{bmatrix} = \begin{bmatrix}
0 & e_{31} & e_{31} & 0 & 0 & 0 \\
e_{31} & 0 & 0 & 0 & 0 & 0 \\
0 & 0 & 0 & e_{15} & 0 & 0
\end{bmatrix} \begin{bmatrix}
\varepsilon_{xy} \\
\varepsilon_{yy} \\
\varepsilon_{zz} \\
\gamma_{yz} \\
\gamma_{xz} \\
\gamma_{xy}
\end{bmatrix} + \begin{bmatrix}
\Theta_{11} & 0 & 0 \\
0 & \Theta_{33} & 0 \\
0 & 0 & \Theta_{11}
\end{bmatrix} \begin{bmatrix}
E_x \\
E_y \\
E_z
\end{bmatrix}$$
(2.13)

Barium Titanate ($BaTiO_3$) is another common piezoceramic material characterized by spontaneous polarization and high piezoelectric sensitivity. Like PZT, it is a ceramic material used in various actuator and sensor applications and its piezoelectric properties are enhanced when it is poled [7].

Polyvinylidene Fluoride (PVDF), differently from the other materials described, is a polymeric material and is one of the most well-known piezo polymers. These materials are characterized by high piezoelectric coefficient ($d_{33}=49.6\ pm/V$), low modulus, lightweight properties, excellent stability, and desirable flexibility [26], making them particularly suitable for applications where flexibility is required and piezo ceramic materials are not so desirable.

Macro Fiber Composites (MFC) are a class of piezoelectric composite materials developed by NASA in 1999. They are composed of rectangular piezoceramic rods embedded between adhesive layers, electrodes, and a polyimide film in a way to enhance durability (Figure 2.6). MFCs are categorized into different types based on their piezoelectric

coupling mechanism: (i) P1-type, which uses the electromechanical coupling effect in the same direction obtaining high effective strain sensing, (ii) P2 and P3-type, based on the coupling effect between two orthogonal directions, suitable for energy harvesting and strain sensing [6].

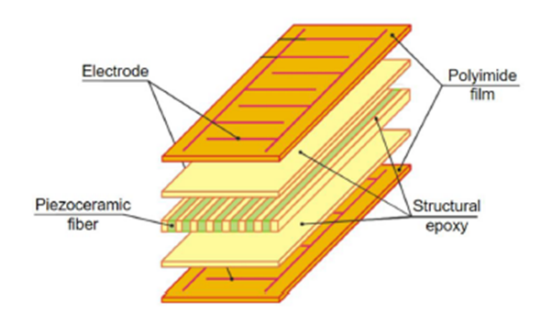


Figure 2.6: MFC composition [6].

	\mathbf{BaTiO}_3	PZT-4	PZT-5A	PZT-5H	PZT-8	PVDF
$d_{31}(10^{-12}C/N)$	-78	-123	-171	-275	-97	-23
d_{33}	149	289	374	593	225	33
d_{15}		496	584	741	330	
$g_{31}(10^{-3}Vm/N)$	5	-11.1	-11.4	-9.1	-11	216
g_{33}	14.1	26.1	24.8	19.7	25.4	330
g_{15}		39.4	38.2	26.8	28.9	
k_{33}	0.48	0.7	0.71	0.75	0.64	0.15
Mechanical Q_M	300	500	75	65	1,000	3-10
Dielectric loss		0.4%		2%	0.4%	
Curie temperature (°C)	115	328	365	193	300	100

Table 2.3: Piezoelectric materials and their properties [55]

In conclusion, piezoelectric materials stand out for their particularly promising properties, making them a topic of interest for the scientific community. Indeed, they represent the key components for piezoelectric energy harvesters, which have increasingly become the focus of attention for their potential applications. However, before discussing the specific case of piezoelectric harvesters, it is essential to outline the general principles of energy harvesting systems.

2.3 Energy Harvesters

Energy harvesting is the process of capturing and converting energy from the environment and transforming it into electrical energy through a device called energy harvester, which can be used to operate various electronic devices (particularly small and low-power applications). These devices, exploiting energy which would otherwise be lost as heat or dissipated, provide a sustainable and cost-effective alternative to traditional energy sources, reducing dependence on batteries and wired power supplies. Unlike conventional renewable energy sources, energy harvesting focuses on collecting locally available energy for immediate use in localized systems. The power levels typically range from nanowatts to hundreds of milliwatts [29] [27].

The emergence of advanced wireless networks, such as 6G, and the rapid expansion of the Internet of Things (IoT) have increased the need for sustainable and efficient power solutions. Traditional battery-powered devices suffer from limited lifespan, frequent recharging needs, and environmental disposal concerns. Energy harvesting provides an alternative by extending the operational life of electronic devices, reducing reliance on batteries, and minimizing electronic waste. It is particularly beneficial for remote, hard-to-reach, or inaccessible locations where battery replacement is impractical. Additionally, energy harvesting plays a crucial role in environmental sustainability by exploiting ambient energy sources, addressing the growing concern over ecological impact. The increasing reliance on batteries to power IoT devices has raised serious issues regarding their disposal, as millions end up in landfills, where heavy metals pose a risk of groundwater contamination. By reducing dependence on conventional batteries, energy harvesters offer a sustainable and eco-friendly solution to these challenges [29] [7].

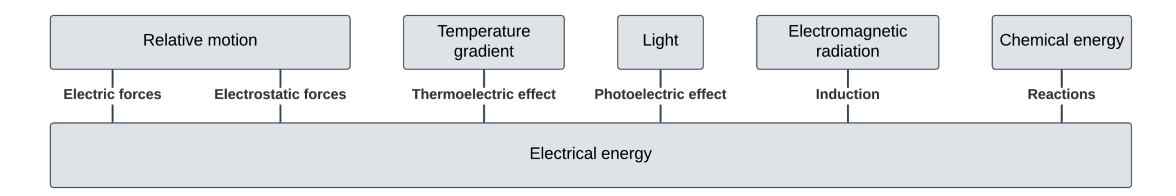


Figure 2.7: Classification of energy harvesting [27].

The classification of energy harvesters is based on the type of energy harvesting source they use. The main sources of energy for harvesting include relative motion (wind, waves, mechanical vibrations), heat (temperature gradient), electromagnetic radiation (radio frequency), light (Photovoltaic) and chemical reactions [29] [27].

Energy harvesters based on heat sources are devices with thermocouples or thermopiles which grasp waste heat from industrial processes or body heat for self-powered electronics. [14] Power density for thermal harvesting from body heat ranges from $10 \ \mu W/cm^3$ to $60 \ \mu W/cm^3$, depending on temperature differences, while from industrial applications ranges from 1 to $10 \ mW/cm^2$. The efficiency of these systems covers a range from 0.1 to 3% [29] [12].

Light-based energy harvesters are constituted by photovoltaic (PV) cells, that convert light energy into electrical energy. This method is commonly used in solar panels and

small scales applications like powering sensors in IoT devices. These devices are characterized by a power density which ranges from 0.006 to $15 \ mW/cm^2$ with an efficiency of 10 - 24% [29] [12].

An example of electromagnetic-based energy harvesters are devices based on RF (radio frequency) sources. RF energy harvesting converts electromagnetic waves from Wi-Fi, cellular networks, and broadcasts into electricity. It enables wireless power for remote or hard-to-reach devices, for its low energy output limits are mainly used for small sensors and IoT applications. In fact, power density goes from $1.2 \cdot 10^{-5}$ to $12 \ mW/cm^2$ and an efficiency of $\sim 50\%$ [29] [12].

Regarding mechanical motion, there are different ways to exploit it and a broad number of mechanisms including ocean wave energy harvesting (1a, 1b, 1c in Figure 2.7), tidal energy harvesting (2a, 2b, 2c in Figure 2.7), wind energy harvesting (3a, 3b, 3c in Figure 2.7), and vibration energy harvesting.

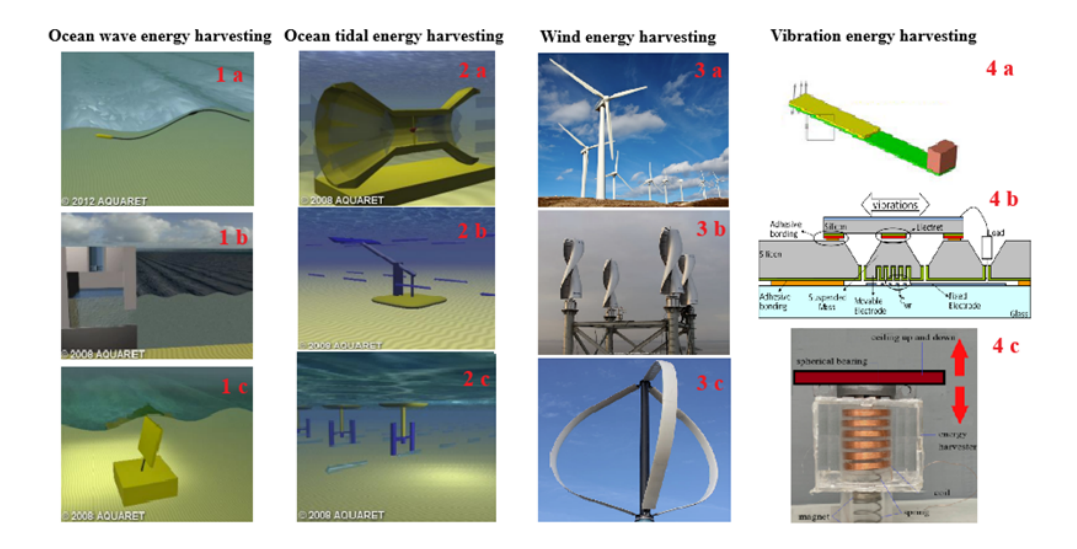


Figure 2.8: Energy harvesters based on mechanical motion. Reproduced from [5, 7, 12, 14, 15, 19, 20].

Among these, the vibration-based energy harvesting are the most promising one, using different transduction mechanisms such as piezoelectric (4a in Figure 2.7), electrostatic (4b in Figure 2.7) and electromagnetic conversion (4c in Figure 2.7).

Electrostatic vibration energy harvesting utilizes the relative motion of an oscillating mass to induce variations in overlapping comb structures, leading to a change in capacitance, which generates voltage at a constant charge. The governing equation is:

$$C = \epsilon_0 A/d, \ Q = C \cdot V \tag{2.14}$$

Where capacitance (C) depends on permittivity (ϵ_0), area (A), and distance (d) [12].

Electromagnetic vibration energy harvesting operates through the movement of a magnetic field relative to a static coil, inducing a current according to Faraday law of electromagnetic induction [12].

Piezoelectric vibration energy harvesting relies on the bending of a beam under mechanical strain, where a piezoelectric material converts mechanical deformation into electrical energy [12].

Piezoelectric transduction has become one of the most popular methods for low-power energy harvesting, particularly for small, autonomous electronics used in healthcare, automotive, and environmental monitoring thanks to its high-power density, simplicity, and scalability. Additionally, piezoelectric harvesters can be produced at both macro and micro scales. This versatility makes them ideal for powering low-energy devices, especially in applications where conventional power sources are impractical or infeasible.

2.4 Piezoelectric-Based Energy Harvesters

Piezoelectric energy harvesters (PEH), as previously introduced, convert mechanical strain into electrical energy through the piezoelectric effect. The process typically involves piezoelectric materials placed on cantilever beams, where bending due to vibrations induces strain in the material, generating voltage that can be harvested [18] [6].

These devices require a consistent vibration source and, thanks to well-established fabrication techniques such as thick-film and thin-film methods, can be produced in both macro and micro scales. This versatility makes them suitable for a wide range of applications, particularly in situations where frequent battery replacement is either impractical or impossible, such as in hard-to-reach areas. Applications include, but are not limited to, wireless sensor networks, implantable medical devices (such as pacemakers), tire pressure monitoring systems, and bridge and building monitoring (see Figure 2.9) [7] [6] [38].

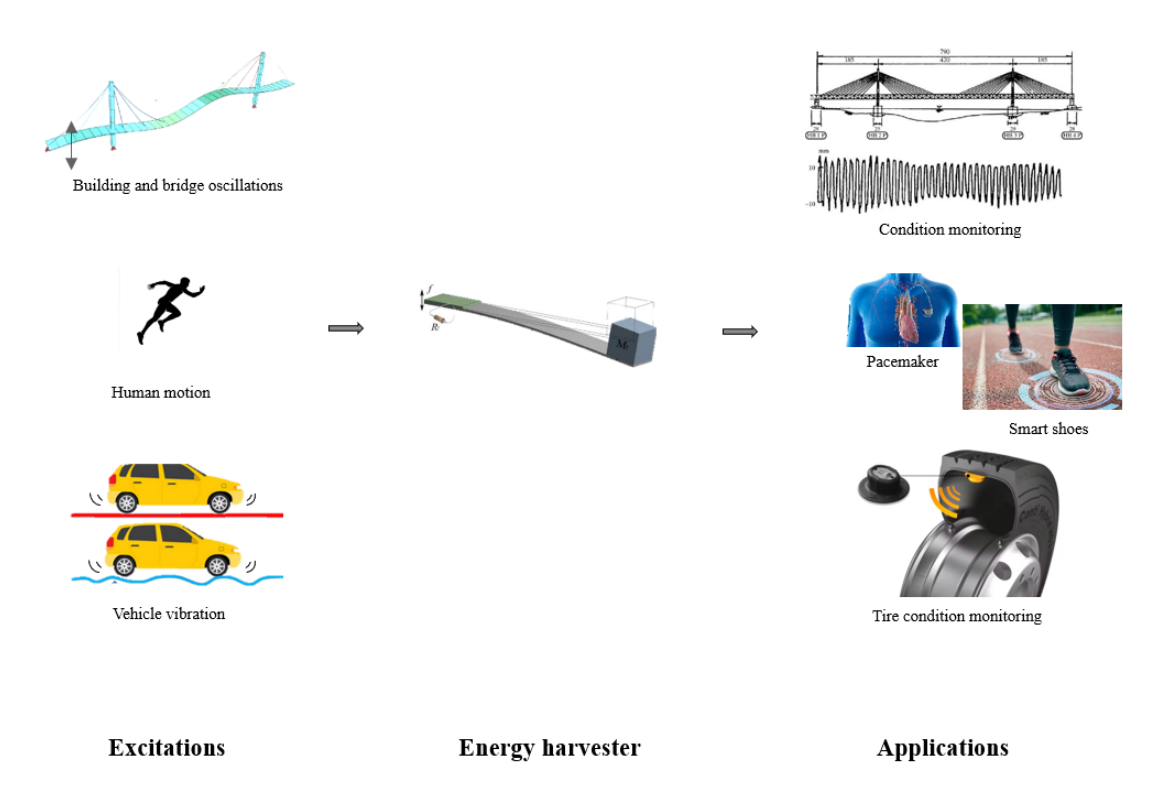


Figure 2.9: PEH applications. Reproduced from [7].

As mentioned earlier, PEH depends on the properties of piezoelectric materials that generate electrical charge when subjected to mechanical stress. The materials commonly used in PEH systems include PZT (Lead Zirconate Titanate), PVDF (Polyvinylidene fluoride), and Macro Fiber Composites (MFCs). These materials are selected for their high electromechanical coupling coefficients, which enable efficient energy conversion. Among these, PZT is the most widely used due to its strong electromechanical response, while PVDF is valued for its flexibility and is typically employed in low-power applications

[7] [6]. Also, devices with porous piezoelectric materials are a field of interest for their suitability in lightweight applications [7].

Since piezoelectric energy harvesting has become a central field of interest in recent years, many configurations have been explored with the aim of maximizing power output and expanding the range of excitation frequencies that lead to significant power extraction, in order to achieve devices that are practically useful in real applications.

Different classifications are defined to distinguish various types of piezoelectric energy harvesting systems. One of these classifications is based on the predominant value of the electromechanical coupling coefficients d_{15} , d_{33} and d_{13} , resulting in three main operation modes.

The d_{13} mode, also known as the transverse mode, is characterized by a polarization direction (which corresponds to the electric field direction) that is perpendicular to the direction of the applied mechanical stress, as illustrated in Figure 2.10.(a).

In contrast, the d_{33} mode or the axial mode, occurs when the polarization direction is aligned with the applied mechanical stress, as shown in Figure 2.10.(b).

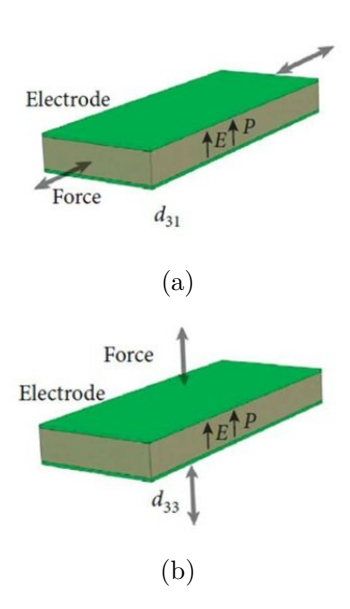


Figure 2.10: Comparison between d_{31} and d_{33} modes [7].

Finally, d_{15} mode, commonly referred to as the shear mode, features a polarization direction perpendicular to the applied electric field. Unlike the d_{13} and d_{33} modes, where the electrodes are positioned perpendicularly to the poling direction, in the d_{15} mode, they are arranged parallel to it.

Another classification is based on the number of piezoelectric layers used to design a single generator. A simple but effective design is the unimorph beam, which consists of a metallic substrate with a piezoelectric layer attached to it. Electrodes, with negligible thickness, are fixed to the piezoelectric layer to allow the electrical charge generated by the strain induced during the beam's vibration to create an electric field between them. In Figure 2.11 a scheme of a unimorph scheme is reported where it is assumed that the

upper and lower electrodes connected to the piezoelectric layer are linked to a resistive electrical load (RL) to develop a simple model for predicting the electrical outputs [8].

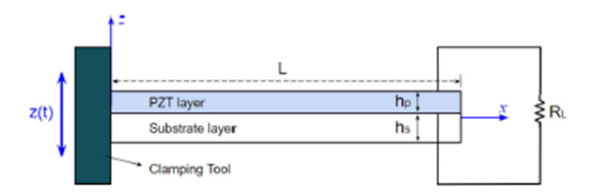


Figure 2.11: Unimorph cantilever energy harvester [8].

An equivalent electrical circuit model can be used to describe that energy harvester (Figure 2.12). The model is represented by two parts coupled. In the left part, the inductor L_m , the capacitor C_k and the resistor R_b are depicted that corresponds respectively to the mass, the stiffness of the piezoelectric beam and the parasitic damping. The AC voltage generator V_m stands for the vibration of the base that acts as an alternating input force. In the right part there is a capacitor C_0 in parallel to the resistive load which represents the capacitance of the piezoelectric layer. V(t) denotes the voltage across the resistive load, while I(t) indicates the current flowing through the piezoelectric layer [7].

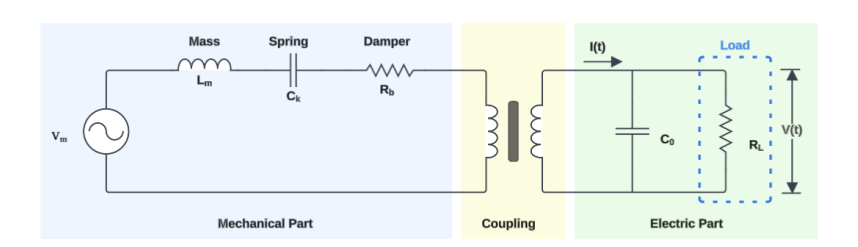


Figure 2.12: Unimorph energy harvester electrical circuit model [7].

For thin beams where the thickness is much smaller with respect to its length, that is the case of piezoelectric unimorph energy harvesters, Euler-Bernoulli beam theory is sufficient to describe the analytical model. In addition, as soon as the electrodes have a negligible thickness perfectly covering the top and bottom piezoelectric surfaces, the electric potential function ϕ is assumed to vary linearly on z direction and has no dependency on x and y coordinates. This assumption implies that the electric field can be represented as in Equation 2.15 [7].

$$E_x = E_y = 0, \quad E_z = -\frac{V(t)}{h_p}$$
 (2.15)

According to Euler-Bernoulli beam theory, the displacement field within the beam can be expressed as in Equation 2.16 [7].

$$U_x = -z\frac{\partial w}{\partial x}, \quad U_y = 0, \quad U_z = w(x, t)$$
 (2.16)

Where U_x , U_y and U_z are the total displacement, and w(x,t) is the relative deflection of the beam with respect to the base.

From the linear strain-displacement relationship, the strain field is obtained thanks to Equation 2.17 [7].

$$\varepsilon_{xx} = -z \frac{\partial^2}{\partial x^2}, \quad \varepsilon_{yy} = \varepsilon_{zz} = \gamma_{xy} = \gamma xz = \gamma yz = 0$$
 (2.17)

Furthermore, there are more complex models of energy harvesters known as multimorph energy harvesters. These devices are characterized by multiple layers of piezoelectric materials with the aim of increasing the power generated per unit scavenger volume [7].

In particular, one of the widely used examples of these devices is the bimorph harvester composed of two layers of piezoelectric. Figure 2.13 is a schematic representation of a bimorph PZT cantilever beam [4].

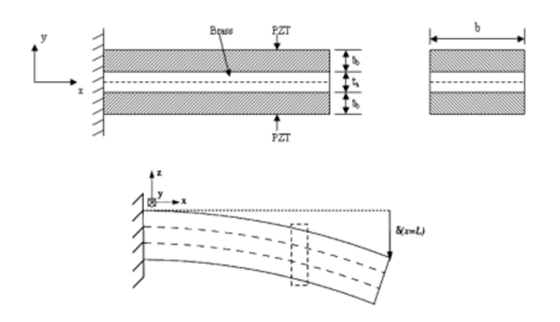


Figure 2.13: Bimorph PZT cantilever beam.

For these types of energy harvesters, the Euler-Bernoulli beam theory alone is no longer sufficient for analytical modeling. The aforementioned classic theory indeed assumes that the beam behavior is governed only by the bending moment, hypothesizing that the cross sections stay orthogonal to the neutral axis and without accounting for the influence of shear. This is valid only in the case of long and slender beams. On the other hand, in piezoelectric bimorphs, the slenderness ratio (beam length to its height) is reduced, and the shear stresses can no longer be neglected. For this reason, Timoshenko beam theory is introduced, which takes into account an angular variable that describes the rotation of the cross-section due to shear deformation [21]. Therefore, a combination of Timoshenko beam equations and Euler-Bernoulli theory has been developed to more accurately describe their real behavior. Piezoelectric bimorphs can be classified based on their manufacturing methods and electrode configurations and the main types are introduced in Figure 2.14.

Series bimorphs, type (a) and (b), have no intermediate electrodes and so the electric field is generated between the top and bottom electrodes. The polarization of the piezo-electric layers is antiparallel, leading to the alternative name antiparallel bimorph. The field strength is determined by the applied voltage V divided by the total thickness 2t. The difference between type (a) and type (b) is a minus sign in the piezoelectric coefficient, while all other parameters remain unchanged. Parallel bimorph, type (c), includes

an intermediate electrode connected to one of the poles of the voltage source leading to a stronger electric field as it is equal to V/t which is twice of that of the previous types. Heterogeneous bimorph, type (d), consists of a single piezoelectric element bonded to a non-piezoelectric material (e.g., metal or dielectric materials like glass). The structural behavior is more complex so that requires different analytical models [4].

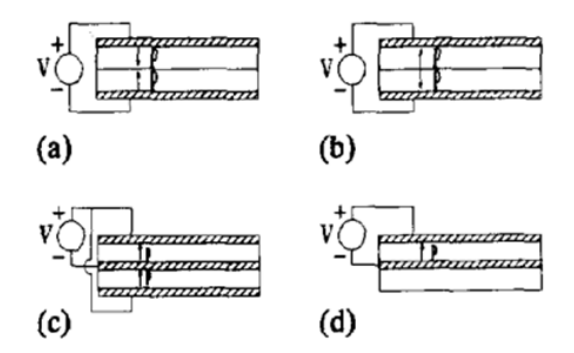


Figure 2.14: Piezoelectric bimorphs configurations: (a) Inward series bimorph, (b) outward series bimorph, (c) parallel bimorph, (d) heterogeneous bimorph [45]

Several models have been developed to enhance the power output of both unimorph and multimorph structures. One common approach is the addition of proof masses at the free end of the cantilever, which increases deformation and improves energy conversion. Another strategy involves modifying the geometry of both the beam or the proof masses to optimize mechanical response and achieve higher performance.

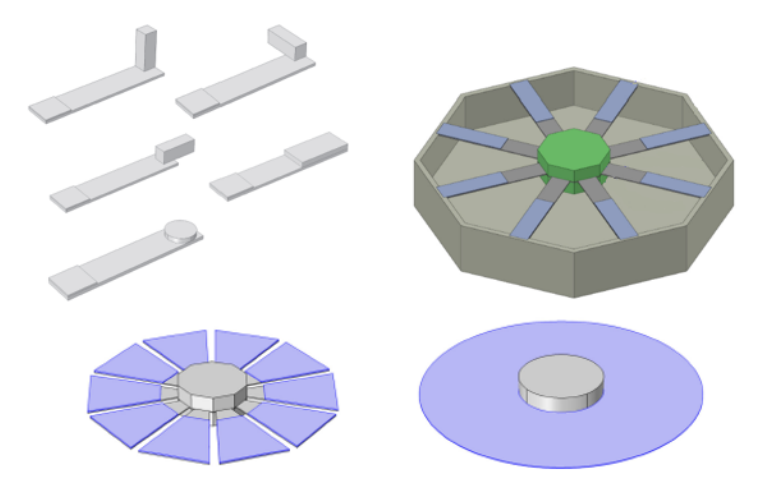


Figure 2.15: Geometrical improvements [38] [8].

An important aspect that must be taken into consideration when designing a piezoelectric energy harvester is the goal of making the first resonance frequencies as close as possible between each other and of falling within the excitation frequency range, typical of the given application. The reason why having the resonance frequencies within the excitation frequency range is that when the excitation frequency coincides with one of the harvester's resonance frequencies, the structure is in resonance condition and the highest possible mechanical strain for that structure at that excitation is achieved. This strain leads to the highest possible electrical charge and so voltage output, improving the overall energy conversion efficiency [6]. In addition, especially in the case of multimodal energy harvesters, it is important to have the resonance peaks close to each other in order to obtain an output voltage, and thus output power, as flat and constant as possible at reasonable values. This enhances also the feasibility and usefulness of the harvester in practical applications, where stable electrical power is required.

2.4.1 Energy Condition Circuits

Piezoelectric energy harvesters generate an AC voltage when subjected to mechanical vibrations. The aim of these structures is to exploit this electrical energy in different applications, that's why a circuit is implemented. The simplest approach is to connect directly the piezoelectric electrodes directly to a simple resistive load to simulate any electronic components that consume electrical energy generating electrical power, as it is shown in Figure 2.16 [8].

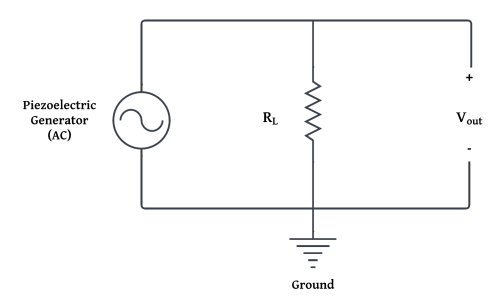


Figure 2.16: Piezoelectric energy harvester with a simple resistor [6].

Nevertheless, as soon as the harvester produces AC voltage, it is necessary to store this energy in practical applications, for example, using a chemical battery that needs a DC voltage. That is why, to improve applicability and optimize energy management, more advanced read-out circuits are implemented, which include different devices (see Figure 2.17).

Rectifier aims to convert the alternate current into direct current to store both positive and negative charges. The simplest one is a diode bridge $(D_1 \text{ and } D_4)$ and is shown in Figure 2.17. Capacitance (C) acts like an intermediate storage capacity preventing excessive charge accumulation. DC/DC converter regulates the output voltage preventing overcharging or discharging of the battery. Battery stores energy and power the connected devices [6].

In the case of having more than one generator, an important factor for the final performance is how the different generators are connected to each other. There are two possible basic ways to connect the generators, series and parallel configurations.

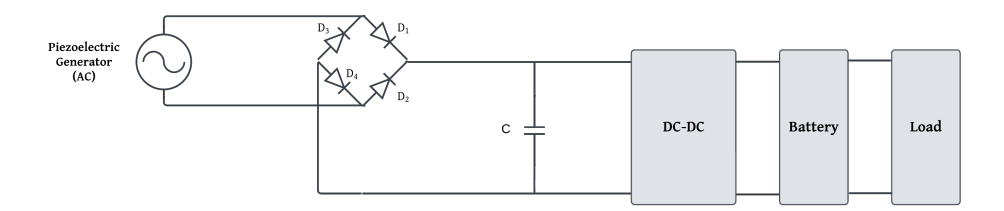


Figure 2.17: Read-out circuit for a single generator [6].

The series configuration is implemented by assigning the ground node to the bottom electrode of the first generator. Then, the top electrode of that generator is connected to the bottom electrode of the second generator, forming the first terminal. Subsequently, the second terminal is assigned to the top electrode of the second generator and the bottom electrode of the third one, and so on until all the generators are connected [8]. Finally, the ground node and the last terminal of the last generator will generate the overall voltage of the entire system so that the total output voltage is the sum of the voltages generated by each piezoelectric element [6]. However, this arrangement is sensitive to failures, in fact if one generator malfunctions, the entire system's voltage output may be compromised. In addition, the problem of voltage cancellation can occur, a phenomenon in which output voltage is nullified due to phase differences between each generator. A way to solve this problem is implementing a rectification stage for each piezoelectric element [6]. On the other hand, the parallel connection consists of having a shared ground node which is connected to the bottom electrode of each generator, and a shared terminal connected to the top electrode of each generator. In this case, the output current is the sum of the currents generated by each piezoelectric element, enhancing the charging process of the storage system. Moreover, this configuration does not suffer from overall failure if only one generator fails, increasing the system's reliability. However, unlike the previous case, the voltage output will be lower [6] [8].

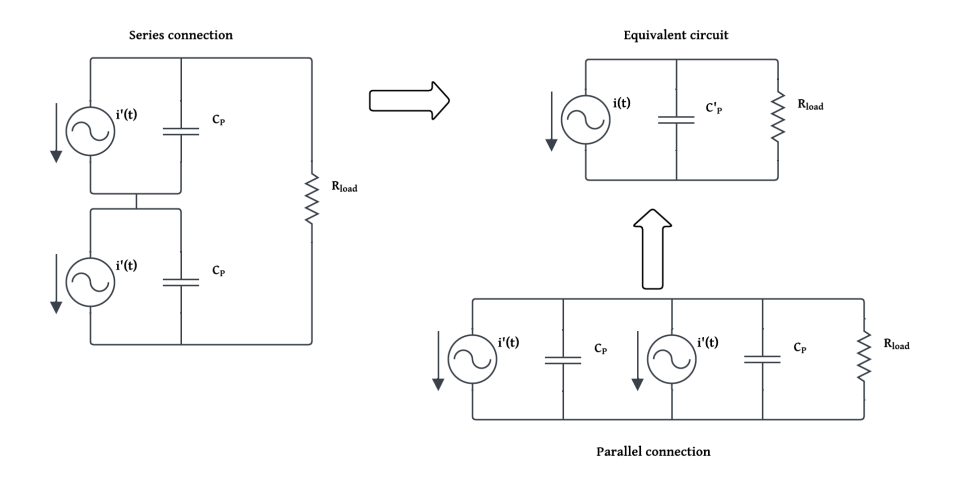


Figure 2.18: Series and Parallel connections [36].

Also mixed parallel-series connection are possible types of configurations to merge the main advantages of both the configurations explained before.

2.4.2 Experimental Setup

To experimentally evaluate the electrical output of the energy harvester subjected to base excitation, and also to validate the results obtained from the FEM analysis performed in specific software such as COMSOL, an experimental setup is required.

Firstly, as is shown in Figure 2.19, a function generator produces a signal, which can be sinusoidal, square, random or many other types. The signal generated must be amplified by a power amplifier, which is then connected to the shaker, providing the base excitation to the piezoelectric device. The electrodes of piezoelectric harvester can be wired in different configurations, and the wires are then connected to a resistance box, where the resistance value of the resistive load can be adjusted according to the desired extraction. Additionally, accelerometers can be placed in the harvester to measure the base excitation and record the acceleration response. These accelerometers are connected to a sensor signal conditioner. Finally, all the outputs coming from the resistance box and the sensor signal conditioner can be displayed on the workstation using a DAQ System [6].

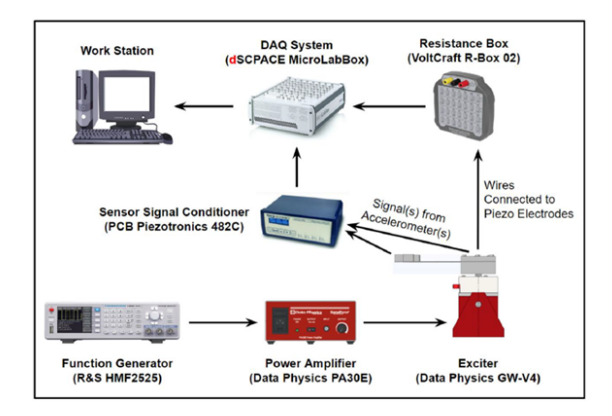


Figure 2.19: Schematic diagram of the experimental setup [6].

2.5 Starting Piezoelectric Harvesting Structure

The aim of this study is to geometrically optimize an existing structure in order to maximize the extracted electrical power. For this reason, it is crucial to introduce and describe the initial structure used to start the optimization process.

The starting configuration is a validated MFC-based Quad-Finger multi-modal energy harvester. From a geometrical point of view, the structure consists of a central plate with $a \times b \times t$ as main dimensions, which are respectively the length, the width and the thickness. One of the four edges of the structure is characterized by four cantilevered beams, each equipped with a proof mass at its free end, with a length L_m , width w and height h_m . Each of the four cantilevered beams has the same width w, coinciding with the one of the proof masses, and is equally spaced by a distance d. Furthermore, the lengths of the beams L_1 , L_2 , L_3 and L_4 are inspired by the proportions of a human hand. Additionally, parameters d_1 , d_2 and d_3 . Finally, the distance between the first beam and the nearest edge of the central plate is equal to the distance between the last beam and the opposite edge, both denoted by s.

From Figure 2.21.(b), it is clear that the width b can be expressed as the function given in Equation 2.18 as follows:

$$b = 2s + 4w + d_1 + d_2 + d_3 (2.18)$$

The overall substructure (also called substrate layer), composed of the central plate and the cantilever beams, is made of aluminum, while the proof masses are made of stainless steel. Mechanical properties of these materials are reported in Table 2.5.

This configuration is referred to as "multi-modal" because the presence of four beams enables multiple resonance modes at relatively low frequencies [50]. This characteristic allows the device to operate efficiently over a wider frequency range, which is advantageous in real-world applications where vibrations often occur over a spectrum of frequencies rather than at a single specific value. This avoids the need for precise tuning to one frequency and reduces performance losses due to frequency shifts, typical of real vibrations.

Each beam includes a piezoelectric patch made of Macro Fiber Composite (MFC), which is responsible for converting mechanical vibrations into electrical energy. These MFC patches are composed of two layers: an inactive layer, with $L_i \times W_i \times t_i$ dimensions, made of polyimide film bonded to the beam, and an active layer, with $L_a \times W_a \times t_a$ dimensions, made of piezoceramic rods (PZT-5A) embedded between electrodes, adhesive layers and polyimide film (see Figure 2.20).

All geometrical values previously named are listed in Table 2.4.

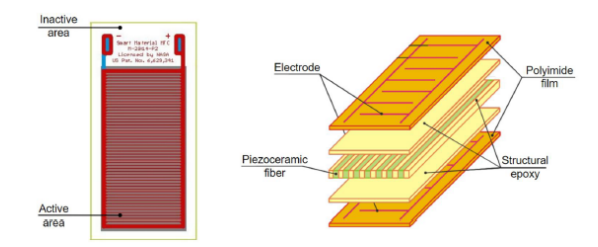


Figure 2.20: MFC microstructure [6].

As for boundary conditions, the device is clamped along three edges corresponding to those of the substructure, while the side with the cantilever beams is left free to vibrate under the effect of a base excitation along z-direction (see Figure 2.21.(a)).

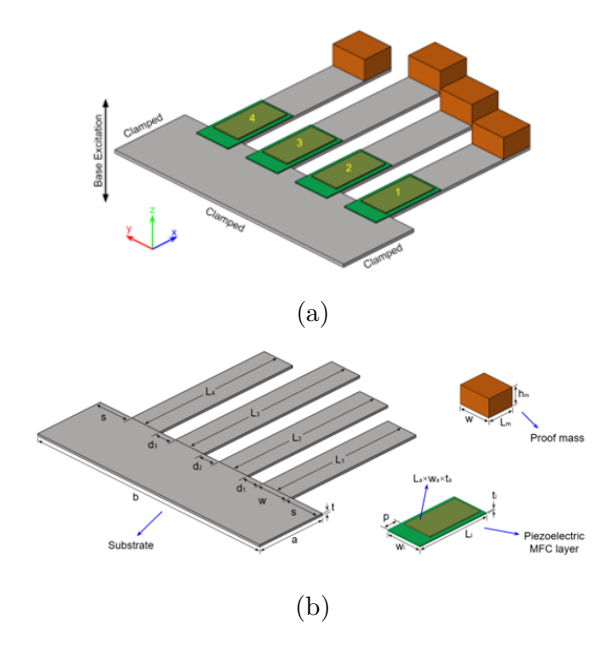


Figure 2.21: MFC-based Quad-Finger multi-modal energy harvester [6].

Focusing on the Macro Fiber Composite (MFC) materials, in order to fully describe the piezoelectric effects, all the components of the constitutive equation (Equations 2.1 and 2.2) has to be defined [6]. Materials data are provided by the manufacturer (listed in Table 2.5 [17]), however, not all the components of the previously mentioned equations are directly available from the data sheet. In particular, the matrix $[S]^E$ is not known apriori, but is retrieved by using standard stress-strain relations for orthotropic materials (Equations 2.19 and 2.20), that rely on the linear elastic engineering constant provided and listed in Table 2.5.

$$S_{11}^{E} = \frac{1}{E_{1}}, \quad S_{22}^{E} = \frac{1}{E_{2}}, \quad S_{33}^{E} = \frac{1}{E_{2}}, \quad S_{44}^{E} = \frac{2(1+\nu_{21})}{E_{2}}, \quad S_{55}^{E} = \frac{1}{G_{12}},$$
 (2.19)

$$S_{66}^{E} = \frac{1}{G_{12}}, \quad S_{12}^{E} = S_{21}^{E} = \frac{-\nu_{12}}{E1}, \quad S_{13}^{E} = S_{31}^{E} = \frac{-\nu_{12}}{E1}, \quad S_{23}^{E} = S_{32}^{E} = \frac{-\nu_{21}}{E2}$$
 (2.20)

Component	Geometrical parameter	Value (mm)
	a	40
	b	130
	t	1
	w	18
Substrate	d	10
Substrate	s	14
	L_1	80
	L_2	90
	L_3	100
	L_4	85
	d_1	10
	d_2	10
	d_3	10
	L_i	37
	W_i	18
	$t_{\pmb{i}}$	0.15
MFC	L_a	28
	W_a	14
	t_a	0.3
	p	7.5
	L_m	15
Proof masses	h_m	10

Table 2.4: Geometrical parameters of the starting structure [6]

Therefore, the final simplified compliance matrix for the MFC piezoelectric material can be expressed in the following way [6].

$$[S]^{E} = \begin{bmatrix} 3.30 & -1.02 & -1.02 & 0 & 0 & 0\\ -1.02 & 6.31 & -1.01 & 0 & 0 & 0\\ -1.02 & -1.01 & 6.31 & 0 & 0 & 0\\ 0 & 0 & 0 & 14.63 & 0 & 0\\ 0 & 0 & 0 & 0 & 18.13 & 0\\ 0 & 0 & 0 & 0 & 0 & 18.13 \end{bmatrix} \times 10^{-11} \quad m^{2}N^{-1}$$
 (2.21)

Concerning the electromechanical coefficients matrix, the simplified matrix shown in Equation 2.22 is retrieved for two principal reasons. Firstly, the piezoelectric materials are polarized in z-direction and so the only non-null components are d_{31} , d_{32} , d_{33} , d_{24} and d_{15} . In addition, another simplification can be performed which consist on considering d_{24} and d_{15} , known as shear coefficients, negligible in composite materials such as MFC [6].

Finally, the dielectric permittivity matrix is simplified to a diagonal matrix (Equation 2.23) [6].

$$\begin{bmatrix} \epsilon^{\sigma} \end{bmatrix} = \begin{bmatrix} \epsilon_{11}^{\sigma} & 0 & 0 \\ 0 & \epsilon_{22}^{\sigma} & 0 \\ 0 & 0 & \epsilon_{33}^{\sigma} \end{bmatrix}$$
 (2.23)

Component	Material property		Value
	Tensile modulus in rod direction, E_1	GPa	30.336
	Tensile modulus in electrode direction, E_2	GPa	15.857
	Shear modulus, G_{12}	GPa	5.515
	Poisson's ratio, ν_{12}	1	0.31
	Poisson's ratio, ν_{12}	1	0.16
Active part	Volume density, ρ	kg/m^3	5440
	$d_{31} = d_{32}$	pC/N	-170
	d_{33}	pC/N	400
	ϵ_{11}^{σ}	1	712
	ϵ_{22}^{σ}	1	1.7
	ϵ_{33}^{σ}	1	737
	Young modulus, E	GPa	1.85
Inactive part (Polyimide film)	Volume density, ρ	kg/m^3	1440
	Poisson's ratio, ν	1	0.34
	Young modulus, E	GPa	70
Substructure (Aluminum)	Mass density, ρ	kg/m^3	2700
	Poisson's ratio, ν	1	0.3
	Young modulus, E	GPa	193
Proof masses (Stainless steel)	Mass density, ρ	kg/m^3	8000
	Poisson's ratio, ν	1	0.3

Table 2.5: Mechanical and electrical properties of components' materials [6] [17]

Once the geometry and materials of the harvester are defined, it is crucial to describe the power management circuit implemented in this study.

As previously discussed, the structure is placed into a shaker, clamped along three edges, and subjected to harmonic base excitation. This vibration induces mechanical strain in the MFC patches, resulting in an alternating voltage output. To collect this voltage and evaluate the electrical power generated, the four piezoelectric patches must be electrically connected between each other and with an external load. For simplicity, a single resistor is selected as external load. Regarding the electrical connection between the MFC layers, a parallel configuration is adopted 2.22. This choice is based on prior study of the substructure [6], which reports that a parallel connection leads to higher output voltage due to the previously described advantages, discussed in Subsection 2.4.1.

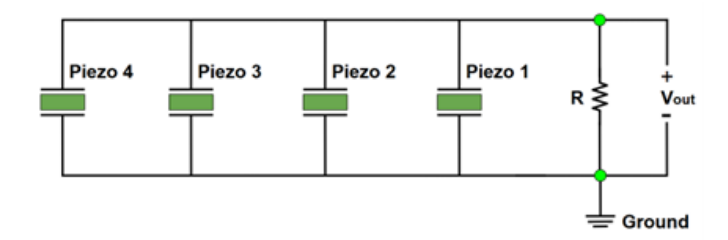


Figure 2.22: Power management circuit of the structure under study.

This initial design of the Quad-Finger energy harvester was simulated in COMSOL Multiphysics and validated through experimental testing by Askari et al. [6], thanks to a fabricated prototype of the starting structure of the harvester shown in Figure 2.23.

In the FE simulations, Aluminum (Young's modulus: 70 GPa, density: 2700 kg/m³, Poisson's ratio: 0.3) was assigned to the substrate, MFC material to the piezoelectric layers, and Stainless Steel (Young's modulus: 193 GPa, density: 8000 kg/m³, Poisson's ratio: 0.3) to the proof masses. The FE model was discretized using fine tetrahedral elements, and eigenfrequency and frequency-domain studies were then conducted.

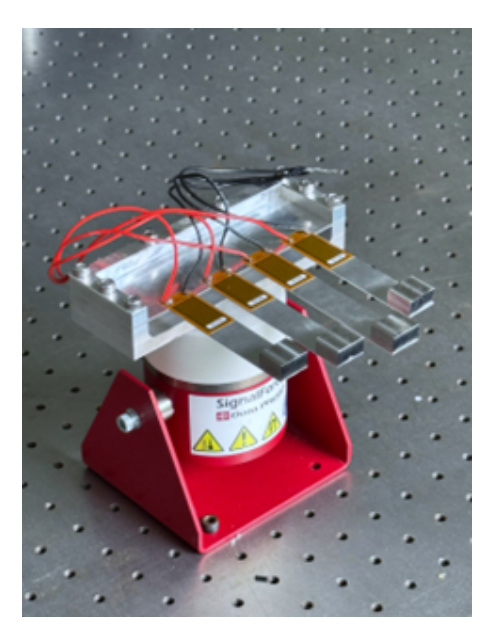


Figure 2.23: Fabricated prototype of the starting structure.

In conclusion, the harvesting structure just described, whose FE model has been experimentally validated, represents the starting point for the hybrid optimization process proposed in this thesis, which is based on the combination of Machine Learning and Genetic Algorithms. It is therefore fundamental to introduce the theoretical background related to Machine Learning models and general optimization principles.

2.6 Machine Learning

Nowadays, Machine learning is increasingly discussed and widely applied in a lot of fields, becoming an essential tool that opens the door to new ways to see things and solve problems. Current applications of machine learning range from personalized search and recommender systems (such as Netflix) to transportation, medical diagnosis, and, particularly relevant to this project, the optimization of energy harvesters. By enhancing their output, machine learning can contribute to making these devices more viable for practical applications.

Nowadays, Machine learning is increasingly discussed and widely applied in a lot of fields, becoming an essential tool that opens the door to new ways to see things and solve problems. Current applications of machine learning range from personalized search and recommender systems (such as Netflix) to transportation, medical diagnosis, and, particularly relevant to this project, the optimization of energy harvesters. By enhancing their output, machine learning can contribute to making these devices more viable for practical applications. Machine learning is a subset of artificial intelligence which is defined by Nils J. Nilsson in "The quest for Artificial intelligence" as "[..] artificial intelligence is that activity devoted to making machines intelligent, and intelligence is that which enables an entity to function appropriately and with foresight in its environment." [33].

It is important to introduce the concept of "deductive" and "inductive" reasoning.

Deductive reasoning (commonly associated with Good old-fashioned AI) consists of explicitly defining rules to make decisions. For example, in a chess game, it defines what a good chess position is by means of if-then clauses.

Inductive reasoning, on the other hand, is the key feature of machine learning and it gathers a large, labeled data set and the system learns. For instance, in a chess game, the system might learn to associate certain positions with the label "win".

«Most machine learning methods construct hypotheses from data. [..] Such an inference is rather "inductive" than "deductive"» [33]

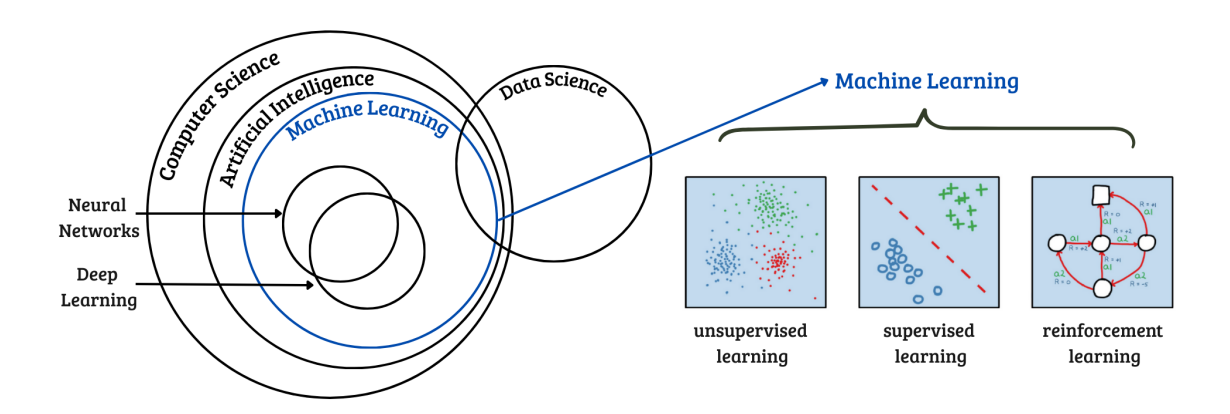


Figure 2.24: AI classification [52].

Machine learning can be classified into three categories, as it is shown in Figure 2.24, which are unsupervised learning, supervised learning and reinforcement learning, each characterized by different subcategories listed in Figure 2.25.

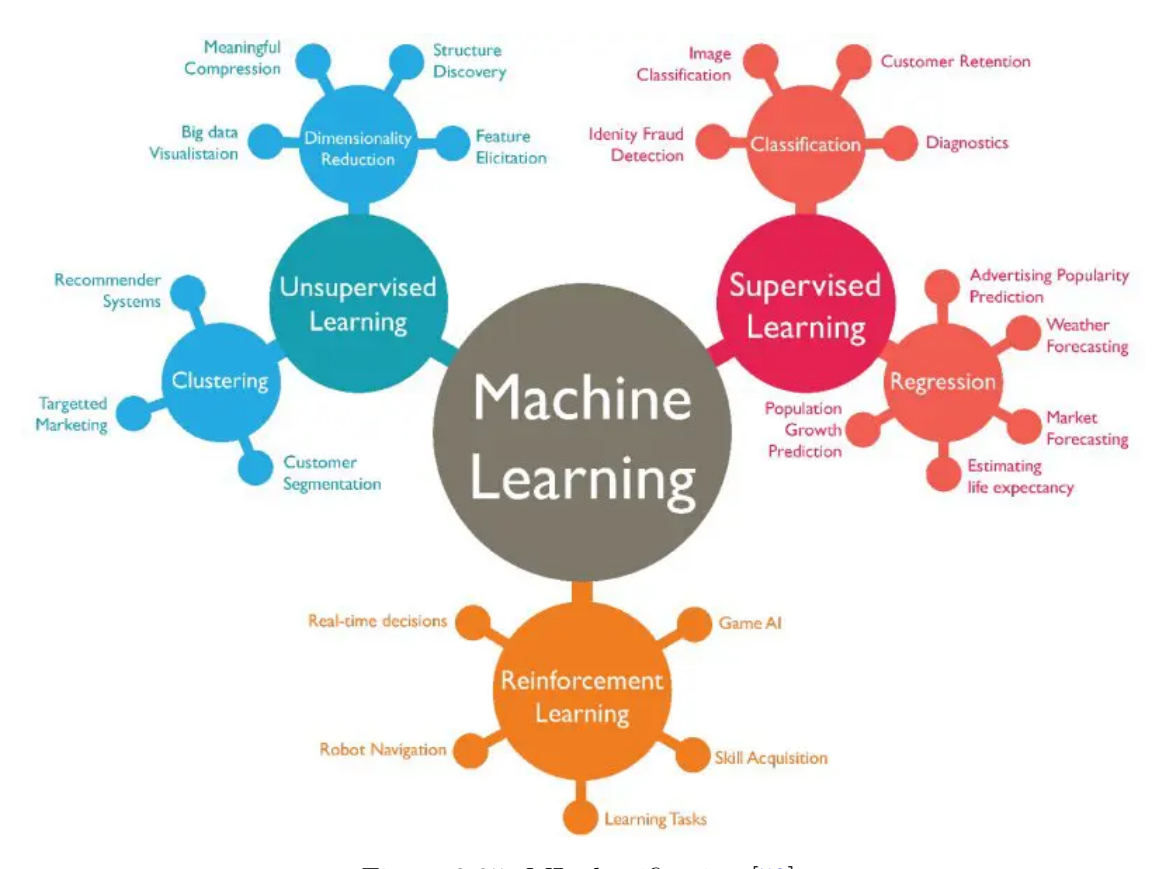


Figure 2.25: ML classification [52].

Unsupervised learning is used to draw interferences from input datasets without any output (targets) to be followed. It can be distinguished in two categories: (i) Clustering, the most common unsupervised learning technique, where different clusters are created based on similar features, and (ii) Dimensionality reduction, technique used to reduce the dimension of a problem, representing the dataset with less variables so that a simpler and faster technique is achieved at the cost of sacrificing some information.

Supervised learning, on the other hand, uses a known set of input data and known outputs to train a model to make reliable predictions. The goal of the model is to make accurate predictions for the output when presented with new, unseen data. This type of model can be additionally divided into: (i) Classification technique which predicts discrete responses (e.g. image recognition, tumor recognition, spam detection etc.) and (ii) Regression technique which predicts continuous responses (e.g. algorithmic trading, power outputs of energy harvesting systems etc.).

Reinforcement learning (RL) «is learning what to do, how to map situations to actions, so as to maximize a numerical reward signal. The learner is not told which actions to take, but instead must discover which actions yield the most reward by trying them» [49].

The RL, differently from the unsupervised and supervised learning that are characterized by a static dataset, has dynamic dataset and has the aim of finding the best sequence of outputs that will generate the optimal outcome. The basics of RL can be summarized in Figure 2.26.

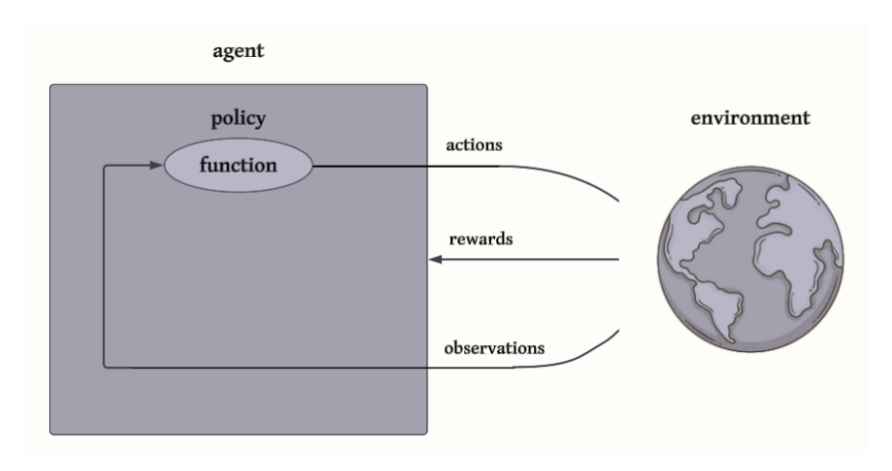


Figure 2.26: RL scheme [52].

Within the agent, there is a function that takes all state observations as inputs and maps them to actions as outputs. In reinforcement learning terminology, this function is referred to as the policy. Based on the set of observations, the policy determines which action to take. Once the action is taken, the environment generates a reward, which is a function that returns a scalar value indicating the desirability of the action taken. The main limitation of RL is the challenging and time-consuming process that requires careful tuning of the so-called hyperparameters and of the reward function [52].

2.6.1 Data Preparation for Machine Learning Models

Before focusing on specific machine learning models to analyze in detail how they work, it is crucial to pay attention to the dataset used to build these ML models.

The first step to create the dataset is data collection based on the expected output of the machine learning model [32]. In the case of supervised learning with regression techniques, this consist of gathering output values corresponding to a a given set of inputs. These data can be collected from various sources, such as physical sensors, numerical simulations performed with dedicated software tools, or many other suitable methods.

The second step consists of identifying the presence of outliers, that are unexpected or abnormal data points within the dataset. They are defined by Hawkins in the following way: "An outlier is an observation which deviates so much from the other observations as to arouse suspicions that it was generated by a different mechanism" [3]. This is a crucial aspect of data preparation, as outliers can significantly affect the reliability of machine learning models. In particular, the presence of outliers can mislead the training process, causing the formation of patterns that do not reflect the general trend of the data and so generating inaccuracies [3]. To identify the presence of outliers Exploratory Data Analysis (EDA) is performed. This analysis has the aim of understanding and identifying

the main features of the collected dataset. EDA consists of analyzing the distribution of variables of the gathered data. In particular, graphical are the most used and intuitive ones to identify the presence of outliers [32] [53]. Histograms, box-plots and scatter-plots are only few examples of graphical way to perform EDA.

Once the anomalous points are identified, the next steps involve data cleaning and data preparing. First, the detected outliers are removed from the dataset to avoid the aforementioned issues. Then, the data are further analyzed to identify common patterns. Based on this analysis, new features are created from the input variables in the raw dataset to later help ML models capturing the significant relationship and improve them. This process, known as Feature engineering, is not mandatory but can be really helpful to improve prediction ability of machine learning models [58].

Finally, in order to train and test machine learning models, it is necessary to split the obtained dataset in two parts: the training dataset and the test dataset. The training dataset is a part of the dataset, usually the 60-70 % of it, used to train and fit the model. The remaining part of the dataset is the test dataset and it is used to provide an evaluation of a model.

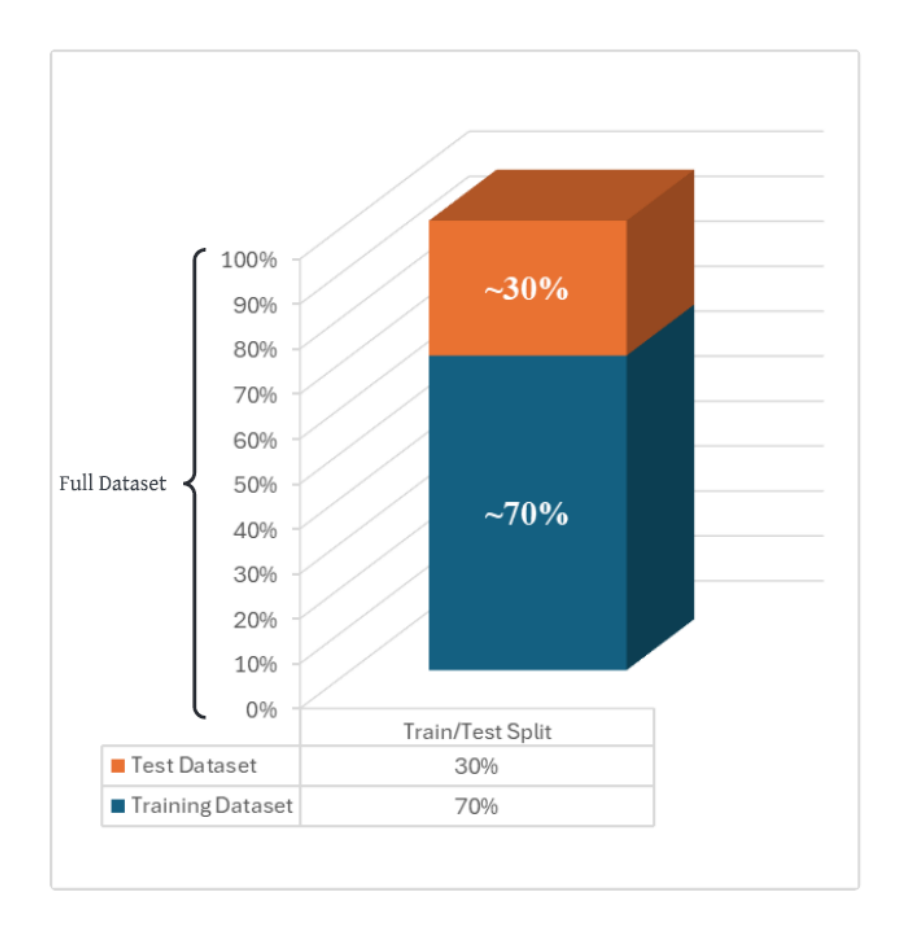


Figure 2.27: Train/Test split [52].

2.7 Ensemble Supervised Algorithms

Ensemble algorithms are a particular type of supervised learning. Differently from simpler algorithms that use only one model to predict the output, such as one decision tree, multiple models are used in ensemble algorithms. The combination of these models has the main objective of obtaining more reliable and accurate predictions and this combination is only effective if there is disagreement between the models. Combining different models leads to effectively reducing the variance-error and in some cases also bias-errors [40].

Since the output to be analyzed in this study is continuous, particular attention is given to the three main regression ensemble models, chosen for their reliability and widespread use: Random Forest Regression (RFR), Gradient Boosting Regression Tree (GBRT), and Extreme Gradient Boosting Regression (XGBR) [18].

Before introducing these algorithms, is important to define what a decision tree is. A decision tree is composed of: (i) root nodes that contain the dataset, (ii) internal nodes where each of them corresponds to an attribute, and (iii) leaf nodes that correspond to the results.

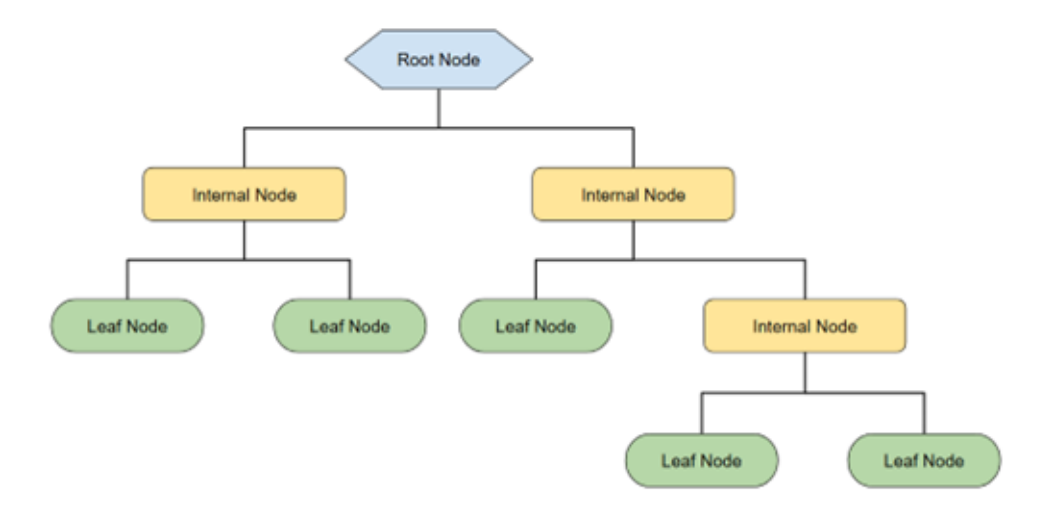


Figure 2.28: Decision tree scheme.

The decision tree splits the dataset recursively using decision nodes until only pure leaf nodes remain, selecting the optimal splits by maximizing the entropy gain. If a data sample meets the condition at a decision node, it moves to the left; otherwise, it moves to the right. Eventually, it reaches a leaf node where a class label is assigned [57].

2.7.1 Random Forest Regression RFR

RFR model, since it is an ensemble algorithm, uses more than one decision tree because the drawback of using a single decision tree is that, slightly changing the dataset, the decision tree changes completely showing a high sensitivity to the training data. In particular, this model is characterized by 5 main steps.

First, multiple training subsets are generated from the original training data. This is

achieved by using the "bagging idea" (also referred as bootstrap aggregating), where random rows from the original dataset are selected to generate new subsets, each containing the same number of rows as the original. Some data may be selected multiple times due to the random sampling process.

In the second step, rather than utilizing all available inputs, only a part of them ,for each subset, is used to train each tree, reducing overfitting and improving model robustness. The procedure of selecting random features for the splitting procedure is called CART algorithm [13].

Once the subsets and the random inputs to consider within each of them are chosen, decision trees are built accordingly.

After the creation of the decision trees, the RFR model is trained and the following phase consist of feeding the algorithm with the test dataset to predict the output. The result would be the average between all the decision trees build.

Finally, the predicted results are compared with the real outputs to have an assessment of the accuracy of the model.

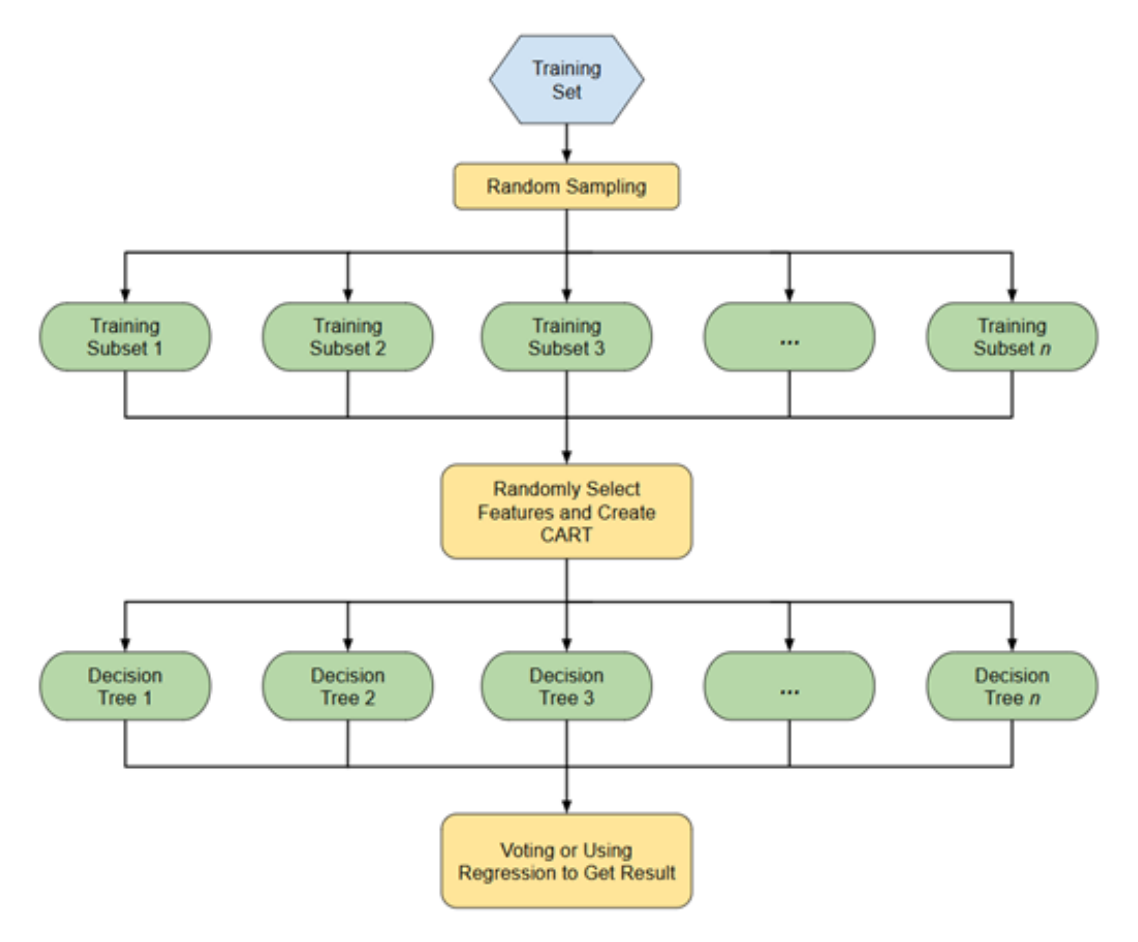


Figure 2.29: RFR flowchart [47].

2.7.2 Gradient Boosting Regression Tree GBRT

Gradient Boosting Regression Tree (GBRT) is composed of two primary components: the Regression Tree (RT) and Gradient Boosting (GB). In GBRT, multiple regression trees are used, where each tree learns the residual error from the cumulative predictions of all previous trees. These residuals represent the difference between the predicted values and the actual values. The final output of GBRT is the sum of the predictions made by each individual tree. The key concept behind GBRT is to identify the right decision tree function that minimizes the loss function during each iteration [18]. The steps followed by the GBRT are listed below.

First, a weak initial model is created but the outcomes from that model have nonoptimal accuracy.

Then, A boosting method is used to train the model so that the previous predictions are continuously improved. To do so, the differences between the predicted values from the weak model (y) and the actual values $(f_m(x))$ are retrieved, as it is shown in Equation 2.24, and named residuals.

$$R(y, f_m(x)) = y - f_m \tag{2.24}$$

The negative gradient approximation is applied in the loss function, following the Equation 2.25, to find the correct direction in order to minimize it.

$$g_m = -\frac{\delta R(y, f_m(x))}{\delta f_m(x)} \tag{2.25}$$

The next step consist of obtaining the subsequent prediction model by adding the residuals to the weak model. In Equation 2.26 the "m + 1" prediction model is derived, where a weight α is considered to prevent overfitting. The latter is a common issue in supervised machine learning, where the model memorizes the entire training dataset, including noise, without capturing the main patterns, leading to a poor generalization [56].

$$f_{m+1}(x) = f_m(x) + \alpha R(y, f_m(x))$$
 (2.26)

This procedure is repeated iteratively, obtaining at the end the results that will be the sum of the conclusions of all the previous trees.

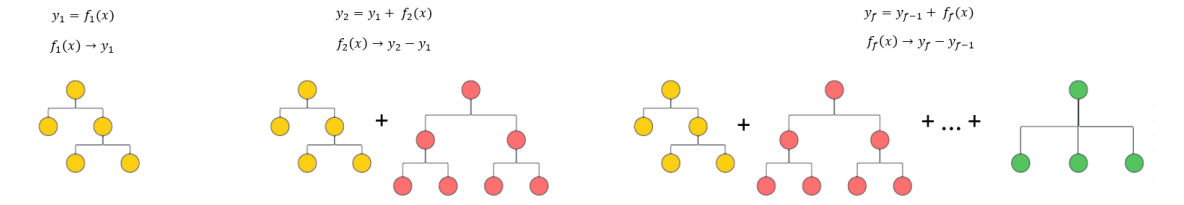


Figure 2.30: GBRT scheme [18].

2.7.3 Extreme Gradient Boosting Regression XGBR

Extreme gradient boosting regression is an evolution of the GBRT model, indeed iteratively improves itself through boosting methods following a similar process of the previously described model. However, XGBR differs in that it continuously adjusts the parameters of the next decision tree by minimizing structural risk. To achieve this, XGBR incorporates a regularization term into the loss function, which helps smooth the final learning weight and prevents overfitting. The regularization function is expressed in Equation 2.27, where T represents the leaf nodes, w_n is the output value of each leaf node and values α and β are coefficients of control of specific gravity.

$$\Omega(h_m(x)) = \alpha T + \frac{\beta \sum_{n=1}^{T} w_n^2}{2}$$
 (2.27)

This model is fast and efficient, making it well-suited for handling large datasets. However, due to its numerous parameters, it is difficult to tune and may not be ideal for high-dimensional data. In the XGBR model, the sum of the predicted values at each step constitutes the final predicted value [18].

2.8 Optimization Problem

The main goal for the design of an energy harvester is maximizing power extraction in order to be competitive in real world applications. Consequently, an important issue to be addressed is a constrained optimization problem. The objective function f(x) lies at the core of that problem, and the process consists in the minimization or maximization of that function. The decision variables x can be more than one and their values are constrained.

The objective function can represent several types of functions coming from different fields of interest such as thermodynamic, economic, environmental field, and so on. For the energy harvesting field one typical objective function could be power extraction or output voltage. In addition, multi-objective optimization could be performed to find an optimal trade-off between the outputs considered. In the field of energy systems there are three levels of optimization.

The first one is the optimal synthesis that aims of searching the optimal system configuration such as the components to be installed.

The second one is the optimal design, where the system configuration is defined and the focus is on the optimization of the design parameters.

Finally, optimal operation consist of optimizing off-design conditions while the configuration and the design are fixed [54].

In this specific case, the level explored is the optimal design since the main configuration of the piezo-harvester has already been defined. The objective is to change the design parameters, such as the length of the beams, in order to maximize the energy extraction. However, finding the maximum power extraction traditionally solving analytical equation is not possible because of non-linear governing equations that require the use of Finite Element Method (FEM) [10]. As a matter of fact, the need of the objective function evaluation through system simulation using COMSOL leads to what is called "Simulation-based optimization" [10].

2.8.1 Optimal Design

Considering the methods used to find the optimal design, the first distinction is between the deterministic and the heuristic methods. Deterministic methods can be further divided into graphical methods, where the objective function is evaluated at several values of the decision variables so that the maximum or the minimum can be graphically detected; direct methods, which consist of iteratively evaluating the objective function; and indirect methods that take advantage of the derivative [54].

These ways of evaluating the best design could not be the best solution high complexity and predominantly stochastic nature problems, much like most real-world phenomena [10]. For this reason, heuristic methods are the most suitable option to tackle this type of problems. Indeed, heuristic methods are particularly well-suited in case of complex, non-convex objective functions, as they avoid being stuck in local maxima or minima. These methods are capable of evaluating the global optimum and, also in this case, it is possible to further divide this category into other sub-categories like Evolutionary Algorithms (EAs) or Simulated Annealing and others [54]. Evolutionary algorithms

are so called because they find the optimal solution by simulating the natural process of evolution. One of the most used is the Genetic Algorithm (GA) [10].

2.8.2 Genetic Algorithm

Genetic Algorithm simulates the selection mechanism of natural genetics to optimize a given problem and is characterized by four main steps.

The first step is called *initialization*. In this phase, an initial population of N individuals is generated. Each individual can be characterized by λ decision variables and each decision variable is described by n number of genes. Therefore, each individual consist of a set of λ binary strings of n bits. For each individual, the objective function is evaluated. Next, a certain percentage of individuals is selected from the initial population according to the value of the objective function. This process is known as *selection*. The third step is *cross-over* (or combination). In this phase, from the selected population two individuals are chosen, calling them parents, which are combined to generate two children. Finally, the *mutation* step is performed, in which, with a certain probability, a single gene can be modified from 0 to 1 or vice-versa. After these steps, the objective function is evaluated and then all the steps are repeated iteratively until the cycle is stopped. Several types of criteria to stop the algorithm can be performed depending on the application [54].

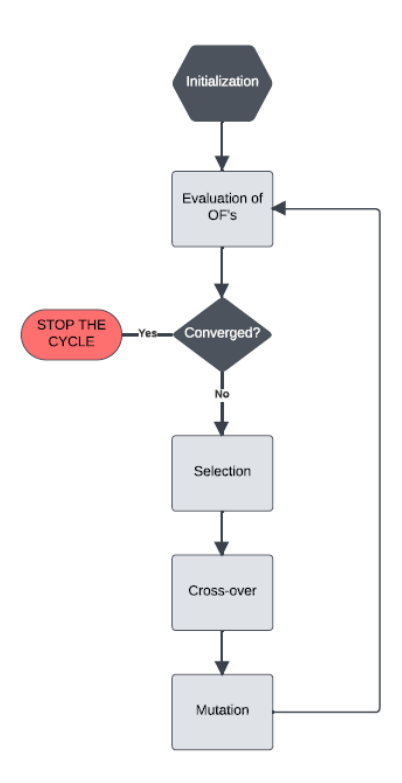


Figure 2.31: Genetic Algorithm flow-chart [54].

Focusing on the *selection* step, several methods are used to retrieve the selected population in order to generate a new population.

Among these methods, the *steady state selection* is a possible choice to perform the genetic algorithm. This method consists of taking only a part Ω of the population but at the end, only one individual or only a small part of the population are replaced in a time step [2].

Another technique consists of ranking the population on their fitness value, giving the name of rank selection. If an individual has the best fitness, it is placed in the first place. Then, depending on the specific variant of the method is used, parents can either be randomly selected from the top ranked individuals or selected based on a probability function (Equation 2.28). The latter is a function of the individual's rank position N [34].

$$P_{i} = \frac{1}{N}(n^{-} + (n^{+} - n^{-})\frac{i-1}{N-1}); \quad i \in \{1, ..., N\}$$
(2.28)

Where P_i is the selection probability, n^+ is the best individual and n^- the worst one.

Moreover, a simpler selection mechanism is the *random selection*, where the parents are randomly selected from the population [25].

One of the most used methods is the *Tournament Selection* and it consists of taking several individuals from the population defined by the tournament size. The individual with the best fitness is subsequently chosen [34].

Furthermore, *Roulette wheel* selection is another well-known technique. Each individual of the population has its own slice of the roulette wheel, but the angle of the sector depends on the fitness value in order to establish the probability of selection that can be calculated with Equation 2.29.

$$PS(I_i) = \frac{f(I_i)}{\sum_{i=1}^n f(I_j)}; \quad j = 1, 2, ..., n.$$
 (2.29)

Where n is the population size and f is the fitness value of the specific individual [34]. Focus is subsequently placed on the *crossover* step. Likewise, in this case, there is more than one method to combine the selected parents generating the new population and some of them are listed below [25].

One of the most commonly used is the *single point crossover*, where a point is randomly chosen and at that point, crossover takes place between two parents.

Another method is the *two points crossover*, which is similar to the first method but crossover is performed between the two points.

Alternatively, the *uniform crossover* selects genes randomly from each parent with the same probability for each gene of the single child.

Finally, also for the *mutation* step multiple methods are available [25].

The most common is the *swap mutation*, in which the values of two randomly selected genes are mutated.

Another approach is to select and mutate only a part of genes, named as *inversion* mutation.

Adaptive mutation is a particular method where the percentage of genes to mutate depends on the fitness value of the solution.

2.9 Related Work

The aim of this study is to optimize the structure of the previously described piezoelectric energy harvester using machine learning and genetic algorithms, with the goal of increasing electrical power output. The methodological approach is based on insights from three research papers, which are discussed in Subsections 2.9.1, 2.9.2 and 2.9.3. For each work, similarities and differences with respect to the present work are highlighted.

2.9.1 Structural Validation of the Energy Harvester

One of the main references is the research paper titled "Design, fabrication and evaluation of a Quad-Finger multimodal vibration energy harvester utilizing MFC generators" [6]. This study proposes and validates a novel energy harvester structure based on four fingers, designed to exploit multimodal excitation, maximizing the harvested energy thanks to higher tunability with real world vibrations. This structure serves as the starting point for the optimization performed in the present work.

While the original project focused on the mechanical and electrical characterization of a precise configuration of the scavenger, through finite element simulations and experimental measurements, this thesis continues the investigation of the quad finger energy harvester with the specific goal of optimizing the design. The aim of the thesis differs from the original study in which the geometric structure of the scavenger was not optimized. Instead, the current goal is to optimize the multimodal design configuration in order to maximize the extractable electrical power.

2.9.2 Machine Learning for Energy Harvester Optimization

The research paper "Optimize output of a piezoelectric cantilever by machine learning ensemble models" [18] investigates the application of supervised ensemble machine learning models in the field of energy harvesting, specifically focusing on a piezoelectric cantilever beam. The machine learning models analyzed in the study are Random Forest Regression (RFR), Gradient Boosting Regression Tree (GBRT), and Extreme Gradient Boosting (XGBR). These models are used to capture the nonlinear relationships between the electrical output (voltage and power) and various geometrical, electrical and dynamic parameters of the system. The lengths of the piezoelectric layer, the weight of the loading mass, the vibration frequency of the shaker and the load resistance are the considered parameters. Ultimately, the three mentioned models are compared to determine which one provides the best fit.

The study demonstrates that ensemble machine learning models can achieve high reliability in capturing the relationships between different parameters and electric outputs, highlighting their potential in energy harvesting field.

Due to the promising results obtained, this paper inspired the approach adopted in the present work, which uses supervised ensemble machine learning models to make reliable prediction for different structure configurations, significantly reducing computational costs. In fact, once the machine learning model is properly trained, it can provide instant predictions without the need of further finite elements simulations. However, while the mentioned study is based on a simple cantilever structure, this thesis applies the models to the more complex quad-finger harvester discussed in Section 2.5. Additionally, the parameters adopted as inputs for the machine learning models enables a deeper and more realistic analysis of the structure with the final aim of optimizing the structure.

Moreover, unlike the reference paper, which focuses solely on understanding the relationships between inputs and outputs, the present work goes a step further by employing machine learning models not only for prediction, but also as the objective function in the optimization problem.

2.9.3 Genetic Algorithms Combined with Machine Learning Techniques

Finally, the third relevant work is "Application of artificial intelligence and evolutionary algorithms in simulation-based optimal design of a piezoelectric energy harvester" [10] which studies the use of machine learning and genetic algorithms to optimize harvester designs.

This approach of mixing machine learning models and evolutionary algorithms has inspired the present work but distinguishes itself for some key features.

First of all, the starting structure is a fully validated complex harvester model which presents different parameters to consider for an optimization. In addition, the goal is not only to simulate or predict but to guide the optimization process toward maximizing generated power of a real harvester structure.

Chapter 3

Main Contribution of the Thesis

The present thesis, as previously discussed, further develops the structure proposed in the research paper "Design, fabrication and evaluation of a Quad-Finger multimodal vibration energy harvester utilizing MFC generators" [6]. The reference study proposes and validates a novel multimodal energy vibration energy harvester, whose design is discussed in detail in Section 2.5.

The aim of this thesis is to take the energy harvester developed in the original research paper, featuring a parallel connection between the four electrodes of the MFC layers electrically connected to a resistive load, as a starting point, and to optimize its design in order to maximize the electrical output. The optimization focuses on several design and operational parameters: the load resistance R, the excitation frequency f, the individual lengths of the four beams L_1 , L_2 , L_3 , L_4 , and the distances between the distance between them d_1 , d_2 , d_3 .

To avoid the time-consuming process of running COMSOL simulations for all possible combinations of the aforementioned parameters in search of the optimal one, a hybrid methodology is adopted. The idea is to combine supervised ensemble machine learning models with a genetic algorithm to guide the design optimization process.

More specifically, the strategy consists on training supervised ensemble machine learning models using only a limited set of combinations. In that way, the requirement of computing COMSOL simulations is extremely reduced, and it is possible to obtain predictions of any given parameter configuration. Once the most suitable machine learning model is trained obtaining an acceptable reliability, genetic algorithm optimization can be implemented to find the combination which maximizes the electrical output. A scheme of the full methodology is reported in the flowchart shown in Figure 3.1. The proposed optimization strategy has been progressively refined through three main approaches. Each step introduces modifications and improvements over the previous one in terms of dataset structure, model prediction capabilities, and optimization efficiency. This step-wise methodology leads to the identification of an optimal configuration the proposed hybrid approach against traditional optimization in COMSOL.

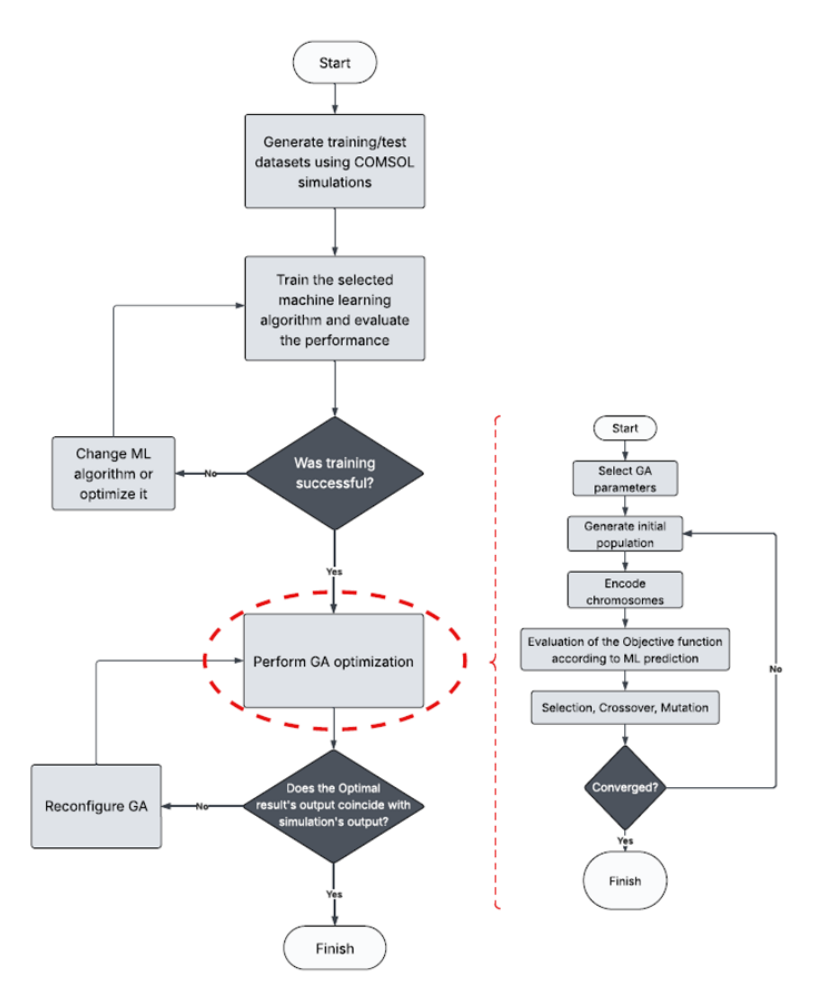


Figure 3.1: Optimization procedure flowchart adapted from [10].

3.1 First Approach: Optimization of beam lengths only with excitation frequencies sweep

The first phase of the study focuses on the optimization of a limited set of parameters. In particular, only the lengths of the four beams and the excitation frequency are considered.

To carry out this preliminary optimization, a dataset is generated through finite element simulations using COMSOL Multiphysics. Each simulation provides electrical outputs (voltage and power) corresponding to several combinations of beam lengths under a frequency sweep. The excitation frequency varies within a defined range for each configuration. All other aforementioned parameters are kept constant, such as the resistive load that is set to $10^9\Omega$ to simulate open-circuit conditions.

Once the dataset is defined, it is exploited to train the ensemble machine learning models with the goal of predicting the electrical outputs for any given configuration. These trained models are then adopted as the objective function of the genetic algorithm,

which aims to identify the combination that maximizes the electrical output.

However, this initial strategy turns out to have a critical limitation. The power and voltage outputs exhibit sharp resonance peaks when the excitation frequency coincides with the structure's eigenfrequencies. These huge variations are challenging for the machine learning models to accurately predict. Therefore, the optimization process that looks for these peaks, struggles to reliably identify the optimal configuration.

This issue motivates a shift to a different approach. The frequency sweep is abandoned in favor of a new approach based on discrete and precomputed excitation frequencies.

3.2 Second Approach: Optimization with discrete excitation frequencies and load resistance sweep

In light of the main limitation emerged in the first approach, a new strategy is developed in which the frequency sweep for each configuration of the dataset is no longer performed. In the present approach, the frequency domain study is performed with the excitation frequency that matches the first eigenfrequency of the corresponding analyzed structure. In this way, it is possible to obtain the electric output peak, ensuring a more efficient analysis.

The strategy of this method consists of calculating, through the eigenfrequency study on COMSOL, the first four eigenfrequencies for each given combination of beam lengths. Then, the first of the obtained eigenfrequencies is adopted as the excitation frequency in the subsequent frequency domain study.

A further addition of this approach is the adoption of a new parameter to be optimized: the load resistance. In the first approach, indeed, a high value of load resistance is considered to approximate an open circuit condition, only focusing on the output voltage. Nevertheless, in real world applications, evaluating the extracted power from the structure is more meaningful. For this purpose, in this stage, a sweep of load resistance values is performed for any given configuration, so that it is possible to maximize the output power, which represents the most relevant parameter for practical application of energy harvesting.

This approach effectively solves the first method's issue related to the huge difference between the voltage peaks and the average value of the output. Thanks to the use of the first eigenfrequency as the excitation frequency, the optimization algorithm result turns out to be more reliable and consistent.

However, a limitation cannot go unnoticed: the analysis is incomplete since the objective function employed in the genetic algorithm is the electrical output associated with the first eigenfrequency. In this way, one loses sight of the structure's multimodal nature. In a multimodal energy harvester, the other vibration modes are significant as they can extend the device's field of application. It is precisely for this reason that in the following strategy, the electrical output is considered for all the first four principal eigenfrequencies. Moreover, in the third approach, additional project parameters are included in the optimization study: the distances between each beam.

Nonetheless, the results of this second approach are not useless. In fact, they can

be useful to appropriately delimit the range of lengths to be considered in the subsequent step, thus avoiding the generation of an overly heavy dataset due to the additional optimization parameters.

3.3 Third Approach: Multimodal optimization with the introduction of beam distances and all modes

The third approach represents the innovative core of this thesis work and the main original contribution made. Differently from the previously introduced strategies, which focus on a single resonance condition, this method is designed to fully exploit the multimodal nature of the studied energy harvesting structure.

The key idea is to consider, for each geometric configuration, the behavior of the system not only at the first eigenfrequency, but also at the second, third and fourth. For each of these excitation frequencies the extracted power is calculated, and the goal of the genetic algorithm becomes to maximize the overall sum of the four powers, thus ensuring high performance not only in a specific condition, but over an entire range of resonant frequencies.

In addition, once explored the role of beam lengths only as geometrical input variables, the distances between beams (d_1, d_2, d_3) are also missing to be added to assess how the combination of lengths and distances can affect performance in order to identify the optimal configuration to maximize power extracted.

The introduction of these new features significantly increases the number of input variables required for the dataset, therefore, it is decided to narrow the range of lengths and reduce the number of resistance values to be considered decreasing the computational effort.

With the evaluation of the four distinct power outputs to be summed, it also introduced the possibility of using multi-output machine learning models, which can not only predict the sum directly, but also estimate each individual power output and subsequently combine them. This type of evaluation is presented as an alternative to the ensemble machine learning models, characterized by only one output, described earlier. The model that will be characterized by higher reliability will then be selected within the genetic algorithm.

In parallel, an analysis is conducted to see whether comparable results could be obtained by reducing the number of samples in the dataset in order to decrease the computational burden required for its generation.

In summary, this approach enables not only more realistic and robust power output optimization, but also the identification of efficient, versatile, and exploitable geometric configurations in real-world scenarios where environmental excitations are not limited to a single frequency.

3.4 Validation of the Hybrid Optimization Model

As a last step, after obtaining the results of the hybrid approach based on ensemble machine learning models and genetic algorithm, it is considered worthwhile to conduct a

validation study using traditional optimization method.

This approach is based on the combined use of COMSOL Multiphysics and MATLAB, via the LiveLink for MATLAB module, with the aim of verifying the robustness of the obtained solutions and their actual reliability.

Again, to avoid convergence to local maxima, a genetic algorithm is used to guide the global optimization. The objective function coincides with that adopted in the machine learning and genetic algorithm hybrid approach, which is the maximization of the electrical power that can be extracted from the piezoelectric energy harvesting system.

However, unlike the hybrid approach in which the power value is estimated by predictive models, here the objective function is evaluated by full FEM simulations performed in the COMSOL environment, one for each individual generated by the genetic algorithm.

Since the first approach has a crucial reliability limit, it is decided to start directly from the second approach as the basis for this validation study.

In a first exploratory step, to test the effectiveness of the optimization, three of the four beam lengths are fixed at the values previously found from the second approach optimization process, leaving the algorithm free to optimize the fourth length and the resistive load value. This step allows to verify the accuracy of the method by analyzing its computational time and evolutionary behavior.

Next, a full optimization is performed on all four beam lengths and resistive load in order to directly compare the obtained configuration with the one identified through the hybrid approach. With this comparison it is possible to assess the applicability of the presented hybrid approach in real-world applications.

Chapter 4

Experimental versus Numerical Validation

This chapter provides the experimental and numerical results of the optimization strategy presented in Chapter 3. For each introduced progressive approach, the adopted methodology is described in details, followed by the discussion and the interpretation on the results. Finally, a comparison is made between the final outcome of the optimization process with the hybrid strategy (Machine learning combined with genetic algorithm) and the traditional optimization performed in COMSOL Multiphysics.

4.1 First Approach: Optimization of beam lengths only with excitation frequencies sweep

4.1.1 Methodology

The first step to optimize the piezoelectric structure is to identify the optimal combination of beam lengths which outputs the maximum electrical power. Considering the strain limitations that the structure can withstand, a range from 45mm to 100mm is selected for all beams. The parameters to set the COMSOL simulations are the following: the frequency of the external excitation [Hz], the base excitation of the shaker [g] and the resistance value [k Ω].

This first approach consist on considering a constant base acceleration equal to 0.5g, a constant resistance of $10^6k\Omega$ and variable frequency.

Varying the base acceleration is not meaningful for the optimization objective of this project. It is well established and logical that increasing the base acceleration leads to higher electrical output. In addition, in practical applications, base acceleration is not something that can be controlled and depends on the specific environment or system in which the harvester is used. Therefore, the goal is to find the geometry that, under a given uncontrollable base acceleration, leads to the highest electrical output compared to the other feasible geometric configurations.

Regarding the excitation frequency, to establish the appropriate range to consider

for each geometrical configuration, two eigenfrequencies studies through COMSOL Multiphysics are performed considering the boundary values of the length range. The first simulation involves a structure with all beam lengths equal to 45mm. The output of that simulation is the identification of the first four eigenfrequencies. The same is carried out for a structure with all beam lengths set to 100mm. The highest electrical output is achieved when the excitation frequency matches the eigenfrequency of the structure. Therefore, since the objective of the project is to find the design that maximizes that output, it is necessary to ensure that, for every configuration in the dataset, the excitation frequency leading to the peak power output is included. Following this line of reasoning, the frequency range under study needs to include the lowest and the highest eigenfrequencies that appears from the previously explained eigenfrequency studies. Once the range of excitation frequencies is defined, it is possible to create the dataset to train and test the machine learning model.

The most important part to have a well-designed machine learning model is the definition of the dataset. This dataset is composed of 20 randomly chosen combinations of lengths within the defined range 45 - 100mm. COMSOL simulations are performed for all these combinations, where the output Voltage (mV) and Power (mW) are evaluated considering a sweep of frequency within the defined range. Consequently, following to the dataset definition, the training and the evaluation of the supervised ensemble machine learning models, as well as the implementation of the genetic algorithm are developed through a Python code, whose structure is described in detail below.

Firstly, the dataset is uploaded and subsequently split into input features and output targets. The input features include the four beam lengths $(L_1 - L_4)$ and the excitation frequency (f), while the output target is the voltage.

In this first approach, electrical power is not considered as the target output for the optimization. This decision is due to the fact that the resistive load is set to a constant and very high value, effectively simulating open-circuit conditions. Under such conditions, the power output becomes negligible due to its inverse proportionality to resistance expressed by Equation 4.1.

$$P = \frac{|V|^2}{R} \tag{4.1}$$

As a result, voltage is chosen as the output target to optimize the structure in this phase, since it remains a meaningful and representative measure of the harvester's performance in open-circuit conditions. In subsequent stages, when other resistance values are introduced, the power output becomes a more meaningful quantity to optimize, as it is the significant quantity in practical applications. The goal of the project is to identify the optimal configuration that delivers the highest electrical power output to exploit the energy harvester in real-world applications.

Once the dataset is uploaded and the input and output features are defined, the train-test split is imposed at 70/30. This means that 70% of the dataset is used to train Machine learning models, while the remaining 30% to test if the predictions made by the models are able to well-approximate the real outputs given by COMSOL simulations.

The next step, after the preparation of the dataset and the division into training and testing subset, involves training and evaluating the three selected ensemble machine learning models: Random Forest Regressor (RFR), Gradient Boosting Regression Tree (GBRT) and eXtreme Gradient Boosting Regressor (XGBR).

To achieve more reliability, these three models need hyperparameter tuning. In order to perform it, a k-fold randomized cross-validation strategy is adopted.

The procedure to perform this strategy, explained below, is the same for all the models but the list of hyperparameters to tune is different depending on the model chosen.

Firstly, a list of detectable values for the hyperparameters is created. Later, a predefined number of random combinations (e.g. 50) are considered. 3) For each random combination K-fold cross-validation method is applied to train the model. This method involves splitting the dataset into k equal-sized, non-overlapping subsets. Then, for each iteration, k-1 subsets are used for training the model, while the remaining subset is used for testing. This process is repeated k times, and the final result of the cross-validation is the average of the k tests [51]. In particular, a 5-fold cross validation is adopted for this study. Finally, Randomized Search CV ends up with the combination that has achieved the best performance.

The way to assess the best performance and so to select the optimal hyperparameters is the evaluation metric known as R-squared value (or R^2 score), defined in Equation 4.2.

$$R^{2} = 1 - \frac{\sum_{i=1}^{n} (y_{i} - y_{p})^{2}}{\sum_{i=1}^{n} (y_{i} - \overline{y})^{2}}$$

$$(4.2)$$

Where n is the number of samples; y_i is the actual value of the sample; y_p is the predicted value; and \overline{y} is the average of all y_i .

The R-squared value is a number that ranges from 0 to 1, and the more this value approaches 1, the more accurately the model's predicted values approximate the real output values.

For each model, a dedicated set of hyperparameters is investigated with the 5-fold cross-validation in order to identify the best combination with the highest \mathbb{R}^2 score.

The list of hyperparameters explored for each model with their corresponding description, is summarized in Table 4.1.

Hyperparameter	Description	RFR	GBRT	XGBR
${\tt n_estimators}$	Number of trees in the ensemble. Increas-	✓	1	1
	ing the number of trees, more stable error			
	estimates and more robustness of variable			
	importance measures are achieved. How-			
	ever, higher computational time is needed.			
criterion	Metric to measure the quality of a	1		
	split. Options include "squared_error",			
	"absolute_error", etc.			
max_depth	Maximum depth of the tree determines	✓	1	1
	how deep the tree can grow. If set to None,			
	the nodes will continue to expand until all			
	leaves are pure or contain fewer samples			
	than the specified min samples split but			
	can lead to overfitting.			
min_samples_split	Minimum number of samples required to	1	1	
	split an internal node, so if the number of			
	samples is minor than the set value the in-			
	ternal node ends up as a leaf node. Having			
	a lower value leads to higher flexibility but			
	increases the risk of overfitting.			
min_samples_leaf	Minimum number of samples required to	1	1	
-	be at a leaf node.			
max_features	maximum number of features to consider	1	1	
	during the splitting procedure to build the			
	decision trees in order to reduce overfit-			
	ting.			
learning_rate	Weight α multiplied to the residuals to re-		1	1
G	duce overfitting. It's a value which ranges			
	from 0 to 1 and the less is the more reduce			
	overfitting at the expense of computational			
	time.			
subsample	Fraction of samples to train each tree. If		1	1
-	it is equal to 1, all the samples are used.			
	If it is lower than 1 the model is called			
	stochastic gradient boosting, where only			
	a stochastic subset of samples is used.			
	Choosing the latter approach, a reduc-			
	tion of variance and an increase in bias is			
	achieved.			
colsample_bytree	Subsample ratio of features used when con-			/
- v	structing each tree.			
gamma	Minimum loss reduction required to make			1
5	a further partition on a leaf node of the			
	tree.			
reg_alpha	α regularization term on weights			/
reg_lambda	β regularization term on weights			1

Table 4.1: Summary of hyperparameters used for each model [39, 42].

Once the 5-fold cross-validation is completed and the optimal set of hyperparameters is selected for each of the supervised ensemble machine learning models, the three algorithms are trained and tested.

To compare their performance and determine which one fits most the problem, and therefore the most suitable to use within the genetic algorithm, two main evaluation strategies are applied.

The first is based on the R^2 score, previously introduced in Equation 4.2. This metric

gives quantitative indication of how well the predicted values match the real ones, and so a fair comparison of the models. In the formula, n is the number of test samples, y_i is the real voltage output obtained from the COMSOL simulations, and y_p is the predicted output from the machine learning model.

Together with the numerical comparison, a more intuitive and visual check is performed by plotting the predicted voltage values against the real ones for each model. This helps to quickly see how closely each model follows the actual simulation results.

The model that shows the highest R^2 value and the best alignment in the visual plot is finally selected as the most reliable model, and is used to evaluate the objective function inside the genetic algorithm.

After having identified the optimal most accurate machine learning model, the genetic algorithm can be implemented using the PyGAD Python library. Each individual in the genetic algorithm population is defined by five genes, where four of these represents the lengths of the beams $(L_1 \text{ to } L_4)$, and the remaining encodes the excitation frequency.

Following the same constraints used during the training of the machine learning models, the values of the beam lengths are bounded within a range between 45 mm and 100 mm. This range, as previously discussed, guarantees structural integrity. Similarly, the excitation frequency is limited within the range preliminary established during the eigenfrequency analysis. Moreover, the beam lengths are limited to either integer or half-integer values. This constraint is due to the fact that arbitrary decimal values are not practical from the fabrication point of view.

Once the constraints are defined, the fitness function is modeled. This function, as previously introduced, corresponds to the output voltage of the harvester system predicted by the machine learning model with the highest reliability. This strategy allows a fast evaluation of the population individuals without using expensive finite element simulations on COMSOL.

To achieve a robust and efficient search process, the main features of the genetic algorithm are carefully selected.

First of all, the population size is set to 500 individuals. For the selection method, the steady state selection approach, described in Subsection 2.8.2, is adopted. Since this method selects only a small portion of the population for the next generation, it helps avoid being trapped in local optima. On the other hand, the algorithm is slower, requiring more iterations to reach the convergence. Regarding the crossover, a single point crossover type is selected. This strategy is computationally efficient and compensates for the choice of the steady state selection method, which leads to higher evaluation effort. Additionally, a random mutation with a probability of 5% is employed in order to introduce stochastic variability in the population. This is crucial for avoiding the convergence toward local maxima, while enhancing the convergence toward global optimum. The genetic algorithm stops after reaching 300 iterations.

To evaluate the performance of the present algorithm, the fitness history is represented across all generations. With that representation is possible to assess the convergence behavior and so the robustness of the optima research process. The final result of the optimization is the configuration that achieves the highest predicted voltage output, representing the optimal design within the defined constraints.

4.1.2 Numerical Results

After having outlined the methodology adopted for the optimization process to find the configuration that maximizes the voltage output, this Section presents and discusses the results obtained from the previously described procedures.

The first part focuses on the preliminary eigenfrequency analysis through COMSOL Multiphysics in order to define a suitable frequency range for the following evaluations.

As detailed in the methodology, the first four eigenfrequencies are computed for the two extreme configurations: one with all beam lengths set to 45 mm, and the other with all beam lengths corresponding to 100 mm. This approach allows to retrieve the boundaries beyond which the eigenfrequencies of any possible beam configuration cannot fall. The results of this analysis are summarized in Table 4.2.

Beam lengths (mm)	$\lambda_1 ext{ (Hz)}$	$\lambda_2 \; (\mathrm{Hz})$	$\lambda_3 \text{ (Hz)}$	$\lambda_4 ext{ (Hz)}$
45	43.809 + 1.0518i	57.533 + 1.3438i	65.709 + 1.5021i	69.151 + 1.5664i
100	16.984 + 0.4002i	19.193 + 0.4465i	20.230 + 0.4666i	20.612 + 0.4743i

Table 4.2: First four eigenfrequencies for two extreme configurations of beam lengths.

From the results reported in the table, the range under study is decided to be from 15 Hz to 70 Hz, in order to include all the voltage peaks for any configuration. Summarizing, the dataset used to train the machine learning models consists of 2,200 samples, each composed of five input features and one output. The output is the voltage of the system, obtained through a frequency domain study in COMSOL, using the following five inputs:

- 1. 20 randomly chosen values for the first beam length L_1 within the 45-100 mm range.
- 2. 20 randomly chosen values for the second beam length L_2 within the 45-100 mm range.
- 3. 20 randomly chosen values for the third beam length L_3 within the 45-100 mm range.
- 4. 20 randomly chosen values for the fourth beam length L_4 within the 45-100 mm range.
- 5. Excitation frequency ranging from 15 Hz to 70 Hz, with a step size of 0.5 Hz between each evaluation

With the dataset now fully defined, the performance of the selected machine learning models, RFR, GBRT and XGBR, is assessed. As outlined in the methodology, the evaluation of the performance is based on the prediction accuracy, measured through the R^2 score, and visually analyzed by comparing the predicted and actual voltage values of the dataset portion used for testing. The following table reports the R^2 scores obtained for each model, while the accompanying figure illustrates how closely the predicted values match those obtained from COMSOL.

Model	RFR	GBRT	XGBR
R^2 Score	0.88	0.91	0.86

Table 4.3: R^2 scores for each ML models.

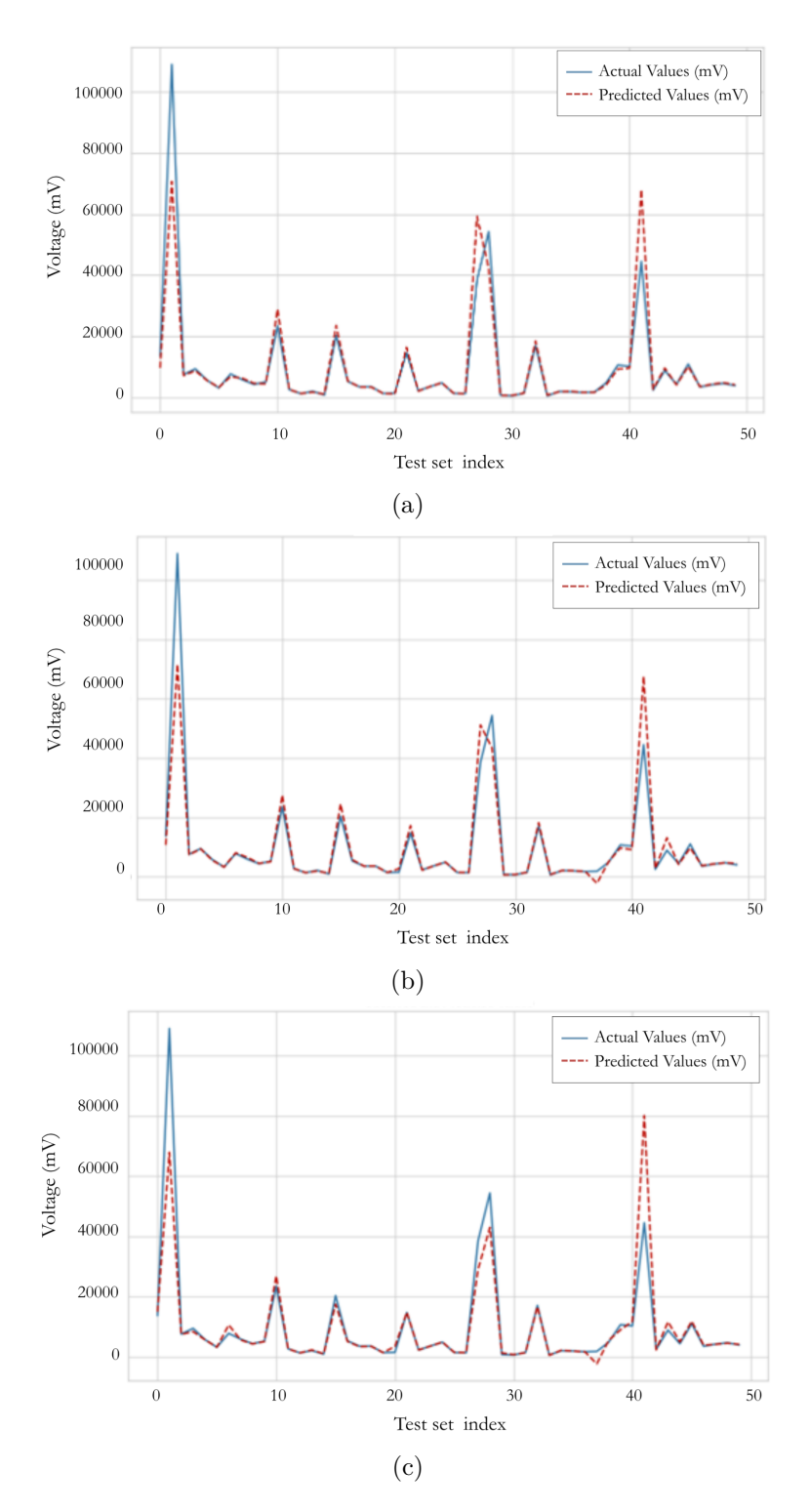


Figure 4.1: Actual versus Predicted values comparison of a part of test set: (a) RFR model, (b) GBRT model, (c) XGBR model.

Table 4.3 highlights that the Gradient Boosting Regression Tree model shows the highest reliability thanks to its previously explained self-improving method used to create the decisional trees. However, even if the value of R^2 seems really promising, a crucial problem is hidden. For each configuration, the majority of the collected data are characterized by really low voltage values, while only where the excitation frequency matches the eigenfrequency, there is a peak of voltage. For this reason, the models can approximate in a really accurate manner the lowest voltage values but for the peaks the reliability drops, as soon as the quantity of peak values is too low to train properly. This crucial problem is evident in Figure 4.1, where the well-suited predictions of the lowest values and the unreliable predictions of the peaks can be easily observed.

This is a crucial problem for the goal of the project, because the aim is to look at the peaks and to maximize them by changing the structure of the piezoelectric energy harvester. However, if the model fails on predicting those peaks a good geometrical optimization cannot be performed.

Consequently, a genetic algorithm, performed by a Python code, is applied to search for the best combination of lengths to maximize the electrical output. For each generation, the electrical output of the combination of lengths and excitation frequency is evaluated thanks to the trained GBRT model, since it is the one that shows the highest reliability. The optimal configuration found by the genetic algorithm is the one described by Table 4.4.

\mathbf{L}_1 (mm)	\mathbf{L}_2 (mm)	\mathbf{L}_3 (mm)	\mathbf{L}_4 (mm)	F (Hz)	Predicted Voltage (mV)	Simulated Voltage (mV)
98.1	75.7	48.9	95.8	19.3	123,074	104,400

Table 4.4: Comparison between predicted and simulated output voltage for the optimal configuration.

Table 4.4 reports the optimal energy harvester configuration obtained through the implemented genetic algorithm, with a predicted output voltage of 123,074 mV. This value, after 50 generations, converged to the aforementioned voltage output as the best fitness value, as shown in Figure 4.2.

A frequency domain study is performed on COMSOL using the obtained values for beam lengths and the dataset frequency sweep to investigate the maximum output Voltage of the obtained configuration. The extracted maximum output Voltage from the simulation corresponds to $\approx 104{,}400$ mV at a frequency value of 19.995 Hz.

The prediction error of the Machine Learning model is approximately 15%. This significant error does not allow the genetic algorithm to find the optimal configuration because peaks predictions of ML model are not sufficiently reliable. The solution to this problem could be to increase the number of combinations, but performing COMSOL simulations for a huge number of samples is really time-consuming and consequently the advantage of using machine learning models to save time for optimization is lost.

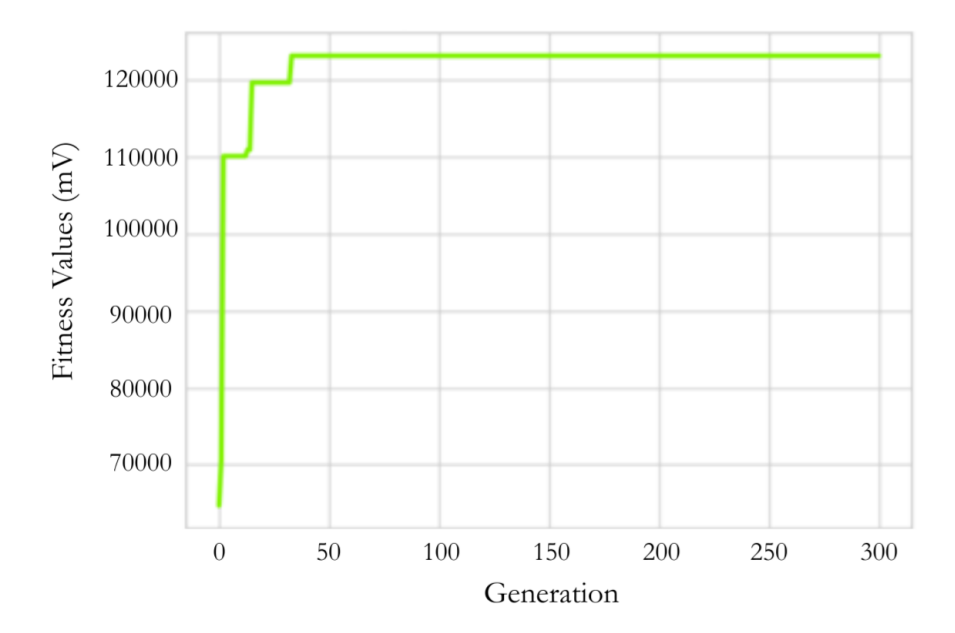


Figure 4.2: First approach: Evolution of the best fitness value across genetic algorithm iterations.

In addition, the machine learning models struggle to predict the peak voltage values, as lowest voltage outputs as the given dataset contains much higher samples with low output. This inaccuracy with peaks is due to the fact that, within the considered frequency range (15-70 Hz) only one sample for each configuration experiences a peak output. At the end, the dataset contains only 20 peak values in total, that are not sufficient to permit ML models to learn how to capture peaks behavior. On the other hand, it is clearly visible that the model can well-predict the frequency at which peaks occur for the specific configuration, which corresponds to the match between the excitation frequency and the first modal frequency of the structure. Other peaks certainly occur not only when the excitation frequency corresponds to the first eigenfrequency but also when it matches the second, the third and so on. In those other cases, peak values are lower than the first case, and for the purpose of the project, the first eigenfrequency is the most significant one

Therefore, to better align with the goal of the project, it is more meaningful a shift to the second approach, introduced in Chapter 3.2.

4.2 Second Approach: Optimization with discrete excitation frequencies and load resistance sweep

4.2.1 Methodology

As introduced in Chapter 3.2, this second approach modifies the method of dataset generation. In particular, a frequency sweep for each geometrical configuration is no longer considered. Instead, the first eigenfrequency is set as the excitation frequency for each simulation. The first eigenfrequency is determined through COMSOL for each geometry. Since these values depend solely on the geometry, the simulation time is significantly reduced. Therefore, developing an additional machine learning model to predict these frequencies would be unnecessary and could compromise the reliability of the process. This choice ensures that each configuration is tested under resonance condition, maximizing the output and avoiding the loss of accuracy of the machine learning models.

With this approach, it is possible to increase the number of simulated configurations while keeping the overall computational time approximately unchanged. Indeed, it is no longer necessary to perform a frequency sweep for each geometry, but a single simulation at the first proper frequency is sufficient.

Following this line of reasoning, the final dataset is constructed by setting the listed parameters on the frequency domain study in COMSOL: 1. Excitation frequency equal to the first eigenfrequency of the specific geometric configuration. 2. Base acceleration of the shaker equal to 0.5 g, according to the reason described in the first approach. 3. A sweep of electrical load resistance values.

After setting the optimal frequency by performing the eigenfrequency study on COM-SOL for each geometry, the next step is to define a meaningful range of resistance value to explore, including values other than the open circuit condition. The goal is to identify the resistance value that maximizes the electrical power generated. This value will then be used as an input variable in ML models, as well as a reference to select the optimal geometry by genetic algorithm.

To understand the range of resistance values over which the output power peak lies for different beam lengths, two COMSOL simulations are performed using a finely spaced resistance sweep. In the first simulation, all beam lengths are set to 45 mm and in the other, they are set to 100 mm. For these two simulations, the resistance sweep ranges from 0 to 10^6 k Ω which corresponds to an open circuit configuration. For the simulation of the configuration with all beam lengths equal to 45 mm an excitation frequency of 43.809 Hz is used, which corresponds to the first eigenfrequency of the structure obtained from the COMSOL results and showed in Table 4.2. Accordingly, for the second configuration an excitation frequency of 16.984 Hz.

Once the appropriate range for the electrical load resistance is defined, it is possible to create the dataset to train and test the machine learning model.

This dataset includes 12 randomly chosen combinations of lengths within the defined range 45-100 mm. COMSOL simulations are performed for all these combinations, where the output Voltage (mV) and Power (mW) are evaluated considering the sweep of resistance obtained in the previous analysis. For the same reason of the first trial of optimization where a frequency sweep is considered, in this improved case other than

these 12 combinations with the entire resistance sweep, 28 more geometries are inserted with a reduced selected set of resistance values. In this way the model can learn peaks behavior more easily, which is the goal of the project, without significantly increasing simulation time.

Before starting machine learning models training, a thorough analysis of the dataset is performed, the results of which are detailed in the Chapter 4.2.2. A number of common patterns emerged from this analysis that influence the electrical output, e.g. the effect of the sum of the beams lengths and the symmetry of the structure.

On the basis of these observations, some features are defined to help the machine learning models easily capturing the most relevant behavior of the structure. This step is part of feature engineering process.

The created features are listed in Table 4.5.

Name	Description
L_sum	The sum of all four beam lengths.
Index 1	This index outputs a 1 when the length of the first beam L_1 , starting
	from the left, is equal to the fourth beam L_4 , and contemporary the
	second beam L_2 coincides with L_3 . In all the other cases this index is
	0. This kind of index identifies the central symmetry of beam lengths,
	that is the symmetry with respect to an imaginary line that divides the
	plate of the structure into two identical parts.
Index 2	Similar to Index 1 but outputs a 1 only when contemporary L_1 coincides
	with L_3 and L_2 matches with L_4 .
Index 3	Index that outputs 1 only when all beam lengths are identical otherwise
	outputs 0.

Table 4.5: Description of the indexes introduced during the feature engineering process.

In conclusion, the final dataset is composed of the lengths of the four beams, the four features described in Table 4.5. The output is the electrical power (mW) is considered, since it is more meaningful with respect to the output voltage in the optimization context. In fact, the main objective is to maximize the extractable power from the energy harvester.

The dataset is divided into training set (70%) and test set (30%), as in the first approach. Again, cross-validation (K-fold) is performed to optimize model hyperparameters and improve reliability.

When the dataset is split into training and test set, some test samples have resistance values very close to those present in the training set for the same geometric configuration. As a consequence, the machine learning models find it relatively easy to predict the output for the test set. This mechanism leads to really high R^2 scores, also equal to the unit, even if models lack real generalization.

For this reason, in order to have a fair comparison between different ensemble machine learning models and determine which is the one that will be used in the genetic algorithm for optimal design selection, additional reliability evaluation metrics are used. Particularly, mean absolute error (MAE) and mean squared error (MSE) are evaluated using the Formulas $4.3 \ 4.4$, as well as R^2 scores.

$$MAE = \frac{1}{n} \sum_{i=1}^{n} |y_i - y_p|$$
 (4.3)

$$MSE = \frac{1}{n} \sum_{i=1}^{n} (y_i - y_p)^2$$
 (4.4)

Where y_i is the real value, y_p is the predicted value and n is the number of samples.

Once the training of the machine learning models is completed, a comparison procedure becomes necessary among the three ensemble-type models, in order to select the most suitable one for the selection criterion within the genetic algorithm.

The evaluation of the performance of the machine learning models is not limited to the numerical metrics alone, as introduced previously, but is extended to more in-depth analysis.

In particular, the residual plot is employed to compare the quality of the machine learning models. The residual graph is a diagram showing the prediction residuals as a function of the actual output power. The residuals are defined as the absolute value of the difference between the predicted power output and the real corresponding output. This instrument turns out to be particularly helpful in assessing the models' reliability for the highest power values, which are also the most relevant from the optimization perspective.

Further analysis is conducted on feature importance. Evaluating feature importance means calculating the percentage of contribution of input variables used to create the decision trees that determine the prediction process of the models. With this approach, it is possible to understand what are the input variables which have the most important impact. This allows testing whether the models are indeed focusing their attention on the most influential features in determining the power generated.

Overall, these evaluations are essential for selecting the most suitable model to be used as an objective function within the genetic algorithm.

After these analysis, and the most reliable machine learning model is selected, it is possible to move on to the implementation of the chosen model within the genetic algorithm. The procedure follows the same pattern as described in the first approach, with some improvements. The main steps of the genetic algorithm, already described in Chapter 4.1.1, are summarized below.

The algorithm starts with the generation of a population of 500 combinations of inputs. In particular, a matrix of 500 rows and 5 columns is created, where the columns are represented by five inputs: L_1 , L_2 , L_3 , L_4 and R.

Each individual of the generated population, so each row of the matrix, is encoded into chromosomes containing five strings of binary codes representing the corresponding input values.

Subsequently, for every individual of the population the fitness or objective function is evaluated. For the goal of the project, the objective function is the power prediction made by the previously selected ensemble machine learning model.

Once the fitness function is evaluated for all the population matrix the following steps are performed: 1. Steady state selection with a number of mating parents equal to 500 elements. 2. Mate selected parents. 3. Single point crossover. 4. Random mutation type with 5% of probability to avoid to be stuck in local minimum.

A new population is generated from the results of these operations, and the whole process is repeated iteratively.

The principal difference with respect to the genetic algorithm implemented in the first approach lies in the stopping criterion. In this case, the genetic algorithm stops after 300 iterations by default. However, early stopping is applied when saturation of the fitness function is detected for more than 20 consecutive iterations. This means that if an individual, with a specific predicted power output, remains the best among all generated individuals for 20 iterations, the algorithm is forced to convergence at the 21st iteration.

As in the first approach, the fitness history graph is analyzed and the results of the optimization in terms of the optimal configuration identified are examined.

4.2.2 Numerical Results

Having described in detail the methodology followed in the second approach (Chapter 4.2.1), it is now possible to present the numerical results obtained. The process' improvements allows to achieve greater reliability in this results, making the overall analysis more robust and effective.

Firstly, as it is described in the methodology part, to build the dataset it is necessary to define a proper load resistance range. The importance of defining it, is to ensure that the electric power peak falls within that range for any geometric combination considered. Speaking of which, two frequency domain studies are performed in COMSOL Multiphysics: the former with all beam lengths equal to 45 mm and the latter with lengths equal to 100 mm. The goal of these studies is to identify, with a very fine sampling step, the value of the resistance corresponding to the maximum power output. The obtained results show that n the first configuration, the peak power lies at a resistance value of approximately 130 k Ω , while in the second configuration, the maximum value is reached at around 340 k Ω . These results are also represented graphically in Figure 4.3, showing electrical power as a function of resistance.

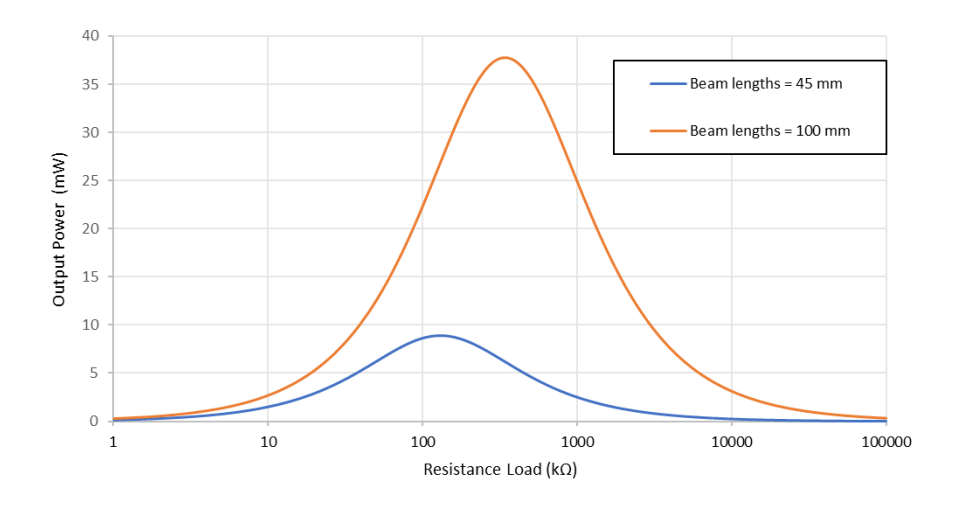


Figure 4.3: Power peak versus electrical load for the two limit configurations.

In light of these outcomes, it is decided to select a resistance range from 100 k Ω to 400 k Ω , which certainly includes peak power for all the feasible beam configurations.

Once this interval is established, it is possible to proceed with the generation of the dataset needed for training and testing the machine learning models.

As previously explained, an initial part of the dataset consists of twelve randomly generated geometric configurations with beams lengths between the minimum and maximum allowed values. An eigenfrequency study is conducted for each configuration in order to identify the first natural frequency of the system, which is then used as the excitation frequency in the frequency domain study. In the latter study, for each configuration, the load resistance value is varied from 100 k Ω to 400 k Ω with a step of 2 k Ω . This first stage yields 12 \cdot 151 = 1,812 samples, each characterized by five input features (four beam lengths and one resistance value) and the associated electrical power output value.

A second part is added to the first part of the dataset, consisting of twenty-eight additional geometric configurations. A frequency domain study is performed also for these new considered geometry but with a limited number of resistance values. Particularly, four values of resistive load are randomly selected within the interval 100 k Ω - 400 k Ω for each configuration. This choice allows the model to better learn the behavior near the power peak, which is the main object of the optimization, without overburdening the computational load. The total number of samples in the final dataset is thus 1,872.

Before proceeding with the three machine learning model trainings, a detailed analysis of the obtained dataset is conducted. This analysis revealed some crucial observations. As the beam lengths increase, the power output increases as well, however it is not the only factor influencing the results. As a consequence, higher total beam length is not the only requirement for achieving higher power output. This evidence is clearly visible from the following example: an energy harvester configuration with beam lengths L_1 , L_2 , L_3 , and L_4 respectively 100 mm, 100 mm, 100 mm, and 82 mm, summing to 382 mm, outputs a maximum power of 29.83 mW. On the other hand, a configuration with beam lengths 100 mm, 82 mm, 82 mm and 100 mm, so 364 mm overall, has 34.22 mW of maximum output power. From that observation, it is clear that kind of central symmetry also has a positive impact on the maximum power output. The presence of this symmetry affects the strain distribution on the structure, making it more uniform and so leading to a more efficient way to exploit all the piezo-harvesters mounted on the beams. Also, having high asymmetries would lead to non-constructive vibrations wasting significant amounts of energy.

Another important piece of evidence is observed by comparing the configuration with all lengths equal to 100 mm, which generates a maximum power of 37.77 mW, with an apparently less performing geometry (100 mm, 90 mm, 90 mm, 100 mm), which instead produces 44 mW. The explanation lies in the vibration mode of the first configuration, where the beams oscillate in phase opposition, causing voltage cancellation and thus reducing the total power. This behavior is confirmed by observation of the first system mode.

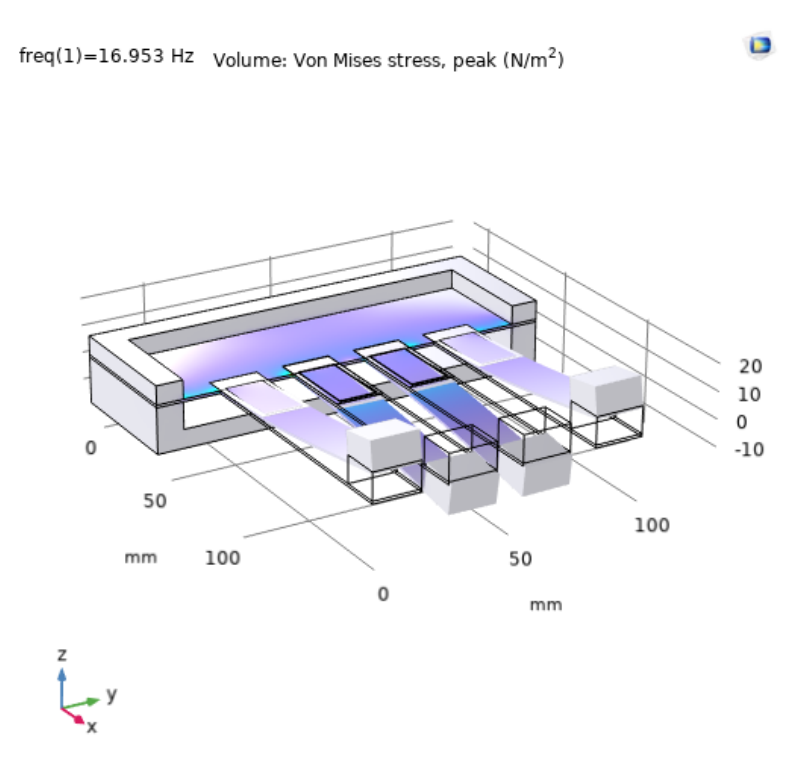


Figure 4.4: Stress distribution and vibration pattern at first eigenfrequency for configuration with all beam lengths equal to 100 mm.

In Figure 4.4, it is clearly visible that a system with all beam lengths equal to 100 mm and excited at its first eigenfrequency exhibits a vibration pattern in which pairs of beams oscillate in opposite directions. This antisymmetric behavior leads to voltage cancellation and consequently to a lower output power.

As a result of these discussed observations on the dataset, the introduction of four additional input features described in Table 4.5 in Chapter 4.2.1 is justified: the sum of the lengths, and the three indices capturing the symmetries within the structure. These additional features are fundamental for enabling the machine learning model to better capture relevant correlations between the geometrical structure and the power output.

The final final dataset thus consists of 1,872 samples, each characterized by nine input variables (the four, the three indices and the total length, as well as the resistance) and one output variable represented by the generated power.

At this point it is possible to proceed to train three ensemble models: Random Forest Regressor, Gradient Boosting Regression Tree, eXtreme Gradient Boosting Regressor.

The first criterion for comparing the models is represented by the evaluation metrics described in Chapter 4.2.1: R^2 , MAE and MSE. The comparison between the three models is reported in Table 4.6.

Reliability Metric	RFR	GBRT	XGBR
\mathbb{R}^2 Score	1.00	1.00	1.00
MAE (mW)	0.07	0.05	0.10
$MSE (mW^2)$	0.08	0.01	0.02

Table 4.6: Comparison of reliability metrics for the three ensemble models: Random Forest Regressor (RFR), Gradient Boosting Regression Tree (GBRT), and Extreme Gradient Boosting Regressor (XGBR).

As can be observed from Table 4.6, all three models have a R^2 score equal to unity. This result is attributable to the fact that, for each geometric configuration, there are multiple load resistance values leading to the generation of similar power output. Consequently, some of these values are included in the train split while the tremainder in the test set, thus facilitating extremely accurate prediction on the latter as well. Such behavior is a symptom of overfitting, as discussed in Chapter 4.2.1 within the methodology section.

To mitigate this effect and make the model robust, the adopted strategy is to include twenty-eight additional geometric configurations in the dataset, each with a reduced number of resistance values. This increased the diversity of the data and improved the generalization of the model.

For a more meaningful performance evaluation, it is therefore necessary to rely on the alternative metrics such as MAE and MSE, from which it appears that Gradient Boosting Regression Tree model shows the lowest mean and quadratic error compared to the others.

However, this result, although indicative, is not sufficient by itself to determine which model should be selected for the genetic algorithm. Therefore, additional qualitative analysis, such as residual plot and feature importance, are considered.

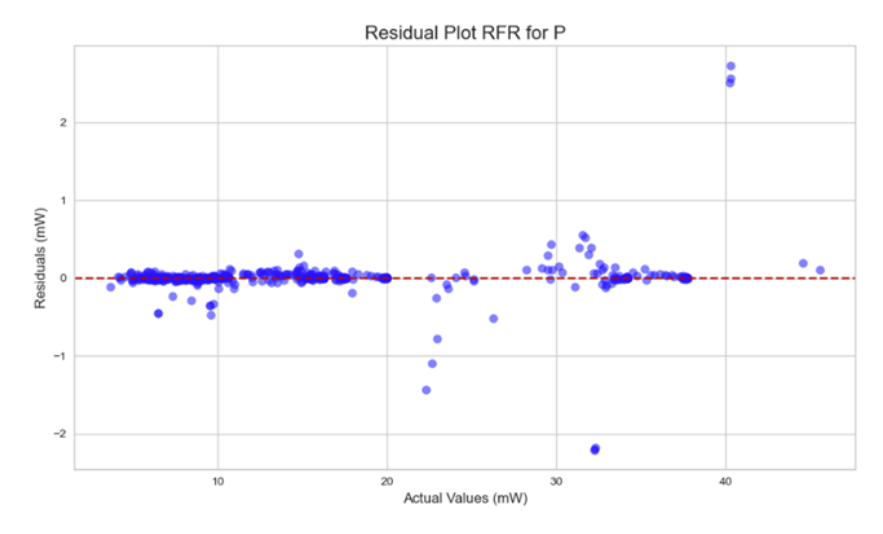


Figure 4.5: Residual plot with Random Forest Regression.

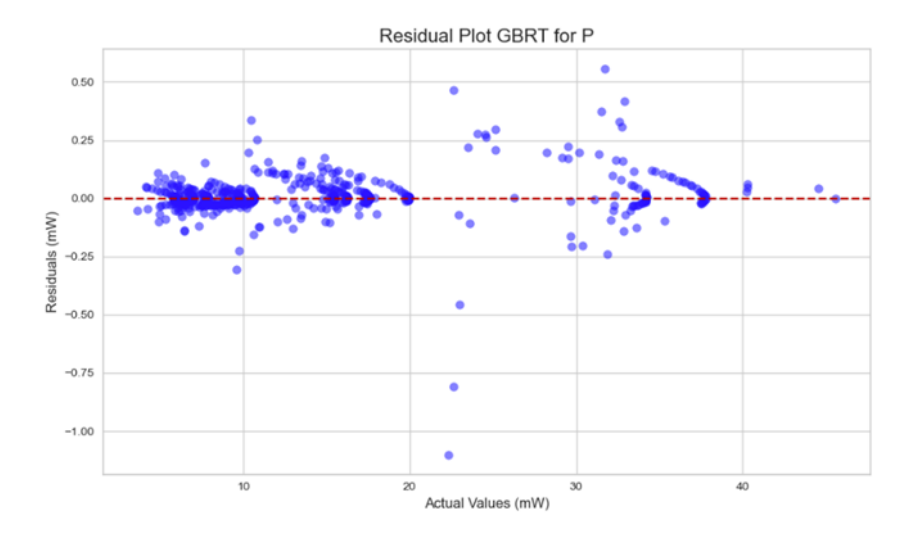


Figure 4.6: Residual plot with Gradient Boosting Regression Tree.

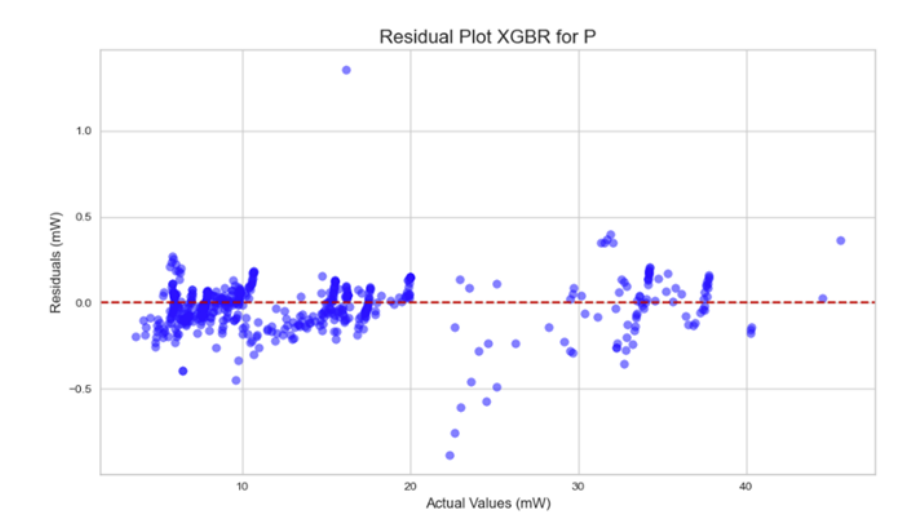


Figure 4.7: Residual plot with eXtreme Gradient Boosting Regressor.

Figures 4.5, 4.6 and 4.7 represent the residual plots of each ensemble machine learning model, where the central red dashed line expresses zero error. It is clearly visible that, especially for highest power output values (mW), the GBRT model shows the lowest prediction error. It is really relevant to focus on the highest power values, as the machine learning models will be used within the genetic algorithm and the goal of the genetic algorithm is to find the optimal geometry that maximizes the output power.

Further analysis was conducted on the significance of the input variables through the assessment of feature importance, the results of which are summarized in Figures 4.8, 4.9, 4.10, and Table 4.7.

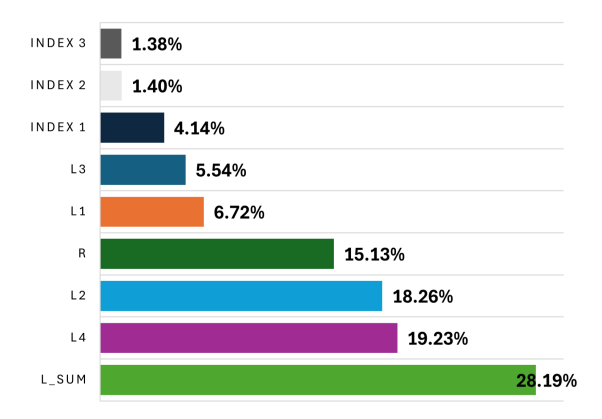


Figure 4.8: Histogram of feature importance of RFR model.

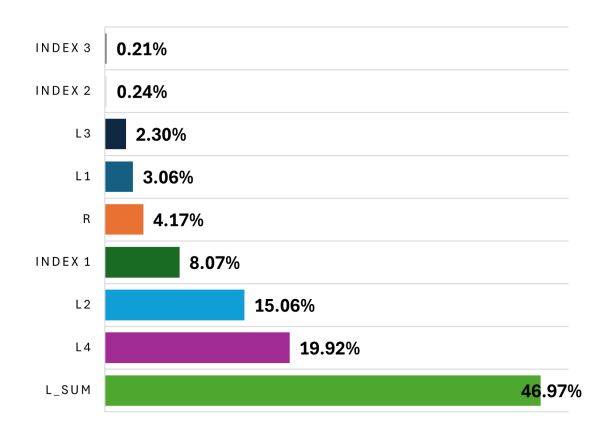


Figure 4.9: Histogram of feature importance of GBRT model.

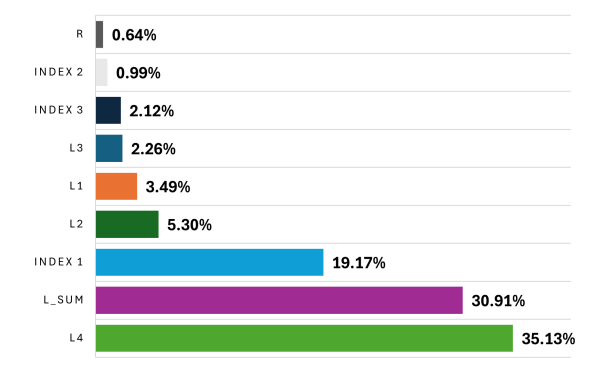


Figure 4.10: Histogram of feature importance of XGBR model.

Feature	RFR	GBRT	XGBR
L1	6.72%	3.06%	3.49%
L2	18.26%	15.06%	5.30%
L3	5.54%	2.30%	2.26%
L4	19.23%	19.92%	35.13%
R	15.13%	4.17%	0.64%
L_sum	28.19%	46.97%	30.91%
Index 1	4.14%	8.07%	19.17%
Index 2	1.40%	0.24%	0.99%
Index 3	1.38%	0.21%	2.12%

Table 4.7: Relative feature importance for the three ensemble models: Random Forest Regressor (RFR), Gradient Boosting Regression Trees (GBRT), and Extreme Gradient Boosting Regression (XGBR).

From Figures 4.8, 4.9, 4.10 and Table 4.7 it is visible that two features, the sum of beam lengths and L_4 , are relevant for all the machine learning models, while the other inputs are treated quite differently by the chosen models. Considering that the Gradient Boosting Regression Tree has the highest reliability and in addition gives quite high importance to index 1, which by an analysis of the dataset is a meaningful feature, it is chosen to be the machine learning model to use within the genetic algorithm.

At this point, it is finally possible to apply the genetic algorithm described in Chapter 4.2.1, in which the fitness function is evaluated using the predictions of the GBRT machine learning model, with the goal of maximizing just such a prediction. The outline of the genetic algorithm has already been explained above, however, it is important to point out a fundamental addition to what has already been described: at the time when the initial population, consisting of random combinations of the five input parameters (the four beam lengths and the resistance value), is generated, the four additional features introduced in the feature engineering phase are also automatically calculated. These features, as already explained, are essential to enable the GBRT model to make a reliable prediction of the generated power value. In other words, for each individual in the population, in addition to the main inputs, the fitness function generates the four derived features (sum of lengths and the three symmetry indices) needed to correctly complete the input vector of the GBRT model and thus obtain the estimated power output to be maximized.

The optimized geometry resulting from the genetic algorithm is shown in Table 4.8, while in Figure 4.11 the fitness history curve is illustrated, showing the evolution of the value of the objective function over iterations.

Configuration	$L_1 \text{ (mm)}$	$L_2 \text{ (mm)}$	$L_3 \text{ (mm)}$	$L_4~(\mathrm{mm})$	$R~(k\Omega)$	Predicted Power (mW)	Simulated Power (mW)
Starting structure Optimal configuration (GA)	80	90	100	85	318	17.600	17.603
	100	92	92	100	340	45.584	45.560

Table 4.8: Comparison between the initial structure and the optimal configuration found by the genetic algorithm, showing input parameters and both the predicted and simulated output power.

Once the result of optimization through genetic algorithm and machine learning is obtained, a validation of the behavior of the optimal configuration through simulations on COMSOL Multiphysics is performed. Specifically, an eigenfrequency study is initially carried out to determine the first eigenfrequency of the optimized structure. Then, this is used as the excitation frequency in the frequency domain study so that the extracted power value predicted by the machine learning model can be compared with that obtained by numerical simulation.

In Table 4.8 it is shown that the Gradient Boosting Regression Tree (GBRT), applied to the optimized structure, predicts a power value of 45.584 mW, while COMSOL simulation returns a value of 45.560 mW, with an extremely small relative percentage error of about 0.05%. This result confirms the high reliability of the supervised learning model employed.

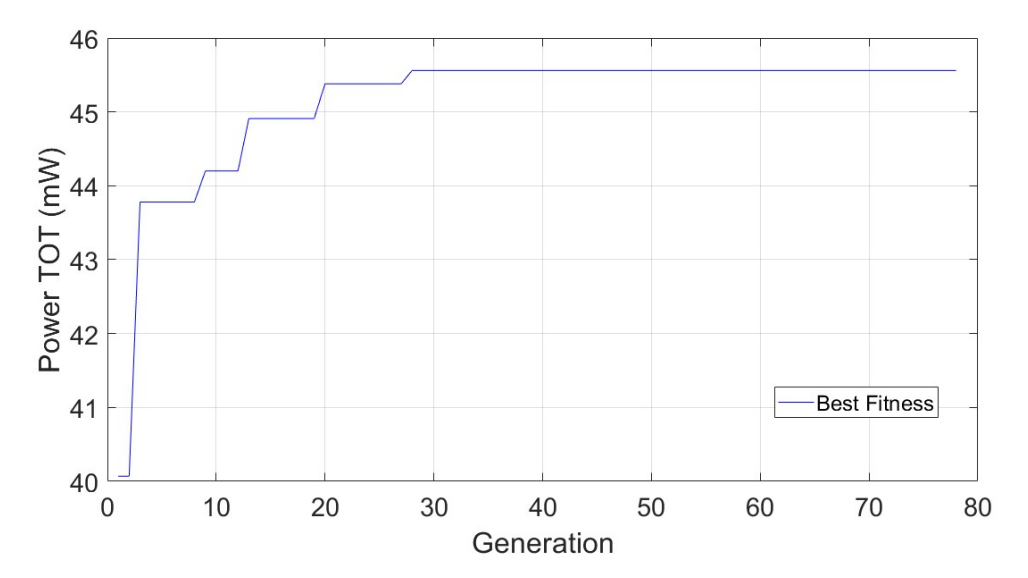


Figure 4.11: Second approach: Evolution of the best fitness value across genetic algorithm iterations.

In addition, comparison between the initial and optimized structure shows a significant increase in extracted power. The initial configuration provided a simulated power of 17.603 mW, while the new configuration yields 45.560 mW, corresponding to a percentage increase of about 158.8%.

Once the reliability of the power value obtained from the optimized structure is verified, the behavior of the optimized configuration can be analyzed in more detail.

In particular, Figures 4.12 and 4.13 represent respectively the geometrical configuration of the optimized structure and the visualization of the structure optimized with the Von Mises stress distribution, in the case where the excitation frequency coincides with the first eigenfrequency.

In Figure 4.13 the modal behavior of the structure is clearly visible: the four beams move in phase, which means they oscillate in the same direction, avoiding voltage cancellation phenomena. This condition leads to efficient energy extraction from all piezoelectric elements. This observation justifies the high extracted power from the resulting structure.

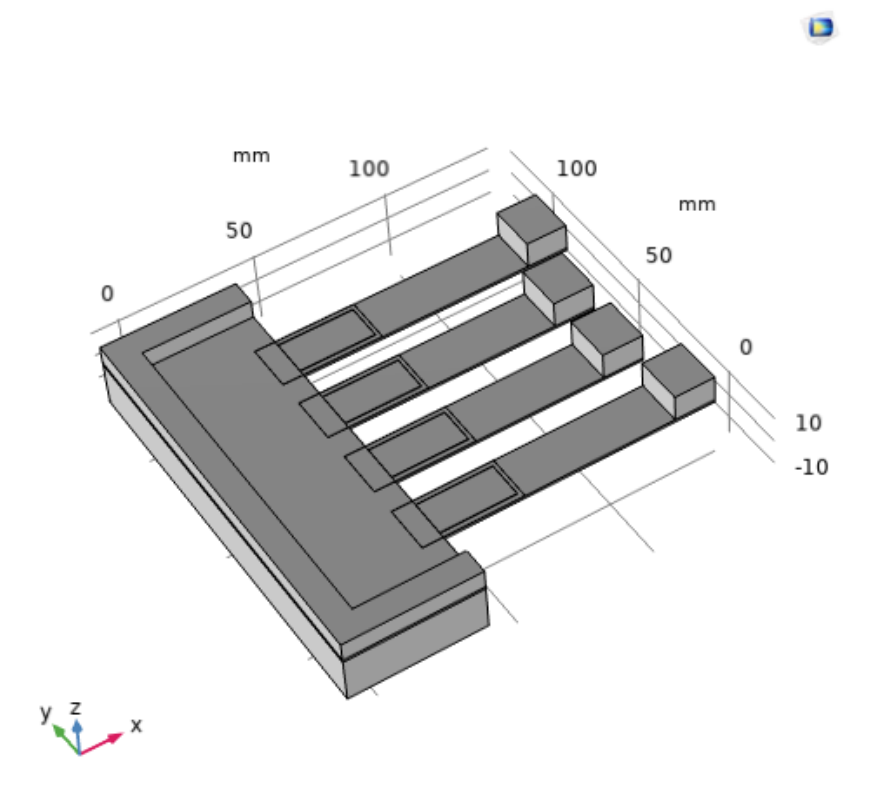


Figure 4.12: Optimized geometry obtained with the second approach, corresponding to the maximum predicted power output using the GBRT-based genetic algorithm.

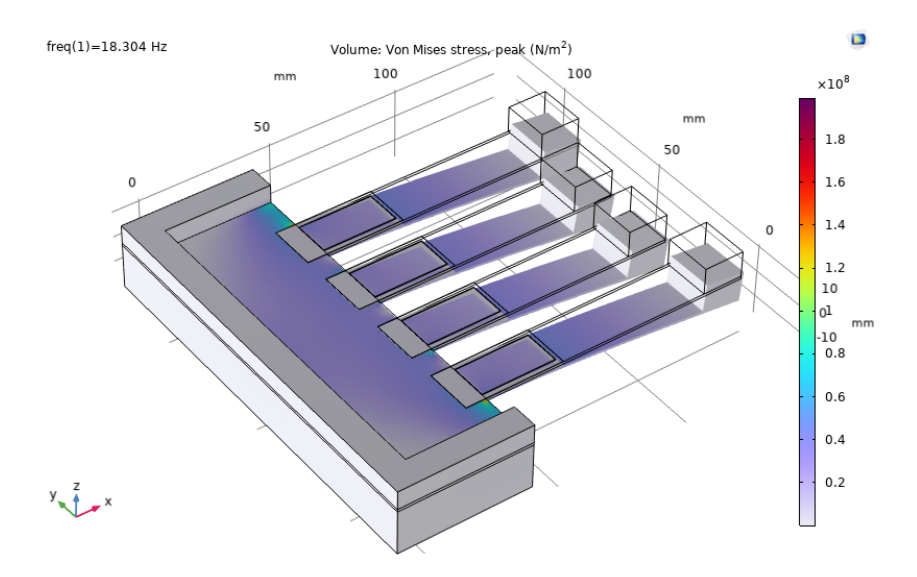


Figure 4.13: Von Mises stress distribution of the optimized configuration (Second approach) when excited at its first eigenfrequency.

Also from the stress distribution, it is observed that the maximum value of Von Mises stress reaches about $1.4 \cdot 10^8$ N/m² (140 MPa), located at the joints between the outer beams and the support plate.

It is well known that aluminum can be used in various forms, from almost pure versions to high-strength structural alloys. As reported by ASM international, aluminum can exhibit great variability in its mechanical properties depending on its composition and the treatments it has undergone. In particular, pure aluminum in the annealed state shows a very low yield strength of about 10 MPa, while heat-treated commercial alloys can reach values of about 550 MPa. Some high-performance alloys reach up to 690 MPa or more [9].

Based on the reported data, it can be concluded that the maximum stress value obtained for the optimized structure of 140 MPa falls within the yield strength limits of common structural aluminum alloys. Therefore, it can be reasonably stated that, except for the use of unalloyed or high-purity aluminum, the structure is able to withstand the expected harmonic excitation while remaining in the elastic range, thus ensuring the mechanical safety of the system.

Having now a more complete overview of the structural and functional effectiveness of the optimized configuration, it is worth reflecting on a fundamental limitation of the approach taken so far. The entire optimization process is conducted by assuming the structure's first eigenfrequency as the excitation frequency. This is a reductive way of approaching the problem, neglecting the multimodal nature of the structure. In fact, the structure with the presence of four beams was created to ensure complex and exploitable dynamic behavior over a wide range of frequencies. This type of structure of the energy harvester is indeed designed to extract power under multiple resonance conditions, corresponding to the first four eigenfrequencies, which are in the lowest part of the spectrum, given the geometry of the scavenger with four cantilevered beams.

Therefore, limiting the study to the first resonant frequency results in a partial view. In fact, setting an optimization with an objective function based solely on power extracted at the first eigenfrequency leads to neglect the starting nature of the structure, which is designed to operate efficiently on a wider frequency range. In this way, there is the risk of obtaining a configuration that can maximize performance at the first eigenfrequency, but at the same time performance suddenly drops at higher frequencies, resulting in a loss of the overall energy potential that the structure would theoretically be able to offer.

For this reason, it is necessary to introduce a third approach, already introduced in Chapter 3.3 and detailed in the following part, which takes into account the multimodal nature of the system. In this new step, for each geometric configuration, the extracted power is calculated when the excitation frequency coincides with the structure's first, second, third and fourth eigenfrequencies. The goal of optimization then becomes the maximization of the sum of these four powers, so as to select a geometry that guarantees good performance over multiple modes and, consequently, stable, high-performance behavior over a wider range of frequencies.

Despite the limitations highlighted, the present approach is nevertheless useful in refining the search range of beam lengths. Indeed, analysis of the dataset shows that low beam lengths lead to significantly lower extracted power since the structure has a higher stiffness and so lower beams' displacement. For this reason, it is decided to narrow the range of lengths to be explored in the following approach from the initial range of 45-100 mm to a narrower range of 80-100 mm. This choice makes it possible to lighten the number of configurations required for the construction of the new dataset, being particularly advantageous since new geometric variables, such as beam spacing, are also introduced in this new phase.

4.3 Third Approach: Multimodal optimization with the introduction of beam distances and all modes

4.3.1 Methodology

Downstream of the first analysis, it is decided to implement a significant change in the optimization methodology. This choice is made from the construction of the dataset and the definition of input and output variables, in order to increase optimization parameters of the harvester structure and take into account its multimodal nature.

The first change introduced in this third approach is to include, as the last step of the optimization, the relative distances between the beams, denoted by d_1 , d_2 and d_3 . These parameters, that were initially neglected, are now considered to allow a more complete exploration of the potential of the structure in terms of extracted power.

Moreover, in previous approaches, the excitation of the system was imposed on the first eigenfrequency, completely neglecting the multimodal nature of the structure. This assumption can lead to optimizing structures that generate peak power only at the first mode of vibration, but perform poorly for frequencies corresponding to the other modes. This represents a substantial limitation, since in the real world, ambient vibrations are neither constant nor perfectly stationary, but often exhibit frequency shifts or irregular behavior. For this reason, it is crucial that the structure maintains high performance even over multiple vibration modes, effectively widening the range of frequencies in which the energy harvester is efficient.

In light of these considerations, the dataset construction strategy is modified together with the characterization of the input and output variables.

As a first step, it is decided to reduce the range of lengths to be considered. Analysis of the dataset generated in the previous approach showed that shorter lengths result in higher stiffness, and consequently, lower vibration amplitude. As a consequence, lower vibration intensity leads to lower power extraction by the piezoelectric patches in the beams. Therefore, the range of beams lengths is limited from 80 mm to 100 mm. In parallel, also the range of load resistances can be reduced, from 100-400 k Ω (previously used) to 200-400 k Ω . This reduction in resistance range is based on previous results. In fact, in Chapter 4.2.2 it is retrieved that in the harvester structure with all beam lengths set to 45 mm the maximum power is reached at approximately at 130 k Ω . By eliminating the shorter lengths, it no longer makes sense to explore very low resistances, and it is therefore decided to completely exclude the range between 100 and 200 k Ω . In this way, the computational cost required to generate the dataset can be contained. Furthermore, it is also necessary to introduce the ranges for the new variables: the distances between

the beams d_1 , d_2 and d_3 . The distance between beams is constrained by the width of the host platform. Therefore, a variable s is introduced, defined as the distance between the extreme (first or last) beam and the nearest edge of the structure. This distance must be strictly greater than zero to avoid beams protruding outside the platform, a condition that would lead to irregular behavior and undesirable structural stresses. In addition, to avoid structural asymmetries, the distance of the first beam from the left edge is required to be the same as the distance of the last beam from the right edge. As a result, once the values of d_1 , d_2 and d_3 are set, the value of s can be uniquely determined as a function of beam distances and the width of the structure. Indeed, since the beams must not laterally protrude from the hosting structure, the upper boundary for the values of d_1 , d_2 and d_3 are automatically created. The lower boundary, on the other hand, is based on the fact that the distance between the beams must be greater or equal to 5 mm, which is considered as the minimum safety threshold to avoid lateral collisions between adjacent beams.

Once the bounds for the considered variables are set, it is possible to proceed with the construction of the dataset. Specifically, 8 random combinations of lengths between 80 mm and 100 mm are generated. For each of these configurations, 24 different combinations of the distances between the beams $(d_1, d_2 \text{ and } d_3)$ are considered. Then, a sweep of electrical resistances is associated to each length-distance configuration, with values that ranges from 200 to 400 k Ω with a step size of 8 k Ω .

This procedure resulted in a theoretical total of $8 \times 24 \times 26 = 4{,}992$ configurations. To these, additional samples are added obtained by taking advantage of the concept of symmetry: for example, a configuration with beam lengths set to [80, 90, 100, 85] and distances symmetrical with respect to the center such as [10, 15, 10] has the same behavior as the mirrored configuration [85, 100, 90, 80], keeping the distances unchanged. Therefore, these mirrored configurations are also included in the dataset, bringing the total number of samples to $5{,}460$.

Once the input variables characterizing each sample in the dataset is defined, the next step is to attribute to each configuration its corresponding set of outputs. These are derived through numerical simulations carried out in the COMSOL Multiphysics environment, with the goal of fully capturing the multimodal nature of the structure.

For each geometric configuration and for each resistance value considered, a dual analysis is performed. The first study is an eigenfrequency analysis, from which the first four eigenfrequencies of the structure are extracted. Unlike previous approaches, in which only the first mode was considered, at this stage it is crucial to consider the subsequent modes as well, since each of them can contribute significantly to power generation.

Subsequently, a Frequency Domain Study is conducted, in which the structure is excited separately at each of the just calculated four eigenfrequencies. For each excitation frequency, a sweep of load resistance values is simulated in the range of 200 to 400 k Ω , with a step size of 8 k Ω . This makes it possible to determine, for each geometric combination, the maximum electrical power that can be extracted at each of the four frequencies.

At the end of this process, each sample in the dataset is described by an input set, consisting of the four beam lengths (L_1, L_2, L_3, L_4) , by the three distances between beams (d_1, d_2, d_3) , by the resistance R, and by the auxiliary variable s which represents

the distance between the extreme beams and the edges of the platform and which, as mentioned above, is completely determined by the values of d_1 , d_2 and d_3 . The associated outputs, on the other hand, are denoted by P_1 , P_2 , P_3 and P_4 , corresponding to the power extracted from the structure when the excitation coincides respectively with the first, second, third, and fourth eigenfrequencies.

Although the sum of these four values, named as P_{tot} does not directly represent the power that can be extracted under real-world conditions, it is still calculated and taken as the objective function for the genetic algorithm. The idea behind this choice is that a structure that exhibits good performance over multiple vibrational modes is more likely to have good performance even under conditions of varying and not perfectly resonant excitation, as is frequently the case in real-world applications.

Once the dataset is constructed, following standard data preparation guidelines Exploratory Data Analysis (EDA) is performed. Specifically, for each input variable and for the total power extracted, all the values taken within the dataset are graphically represented and superimposed by three lines: the line representing the average value of the considered variable, and the limits corresponding to ± 3 times the standard deviation (σ). This type of analysis is commonly used to detect potential outliers, defined as samples that deviate anomalously from the rest of the distribution. However, in the present case, EDA is not used to remove such values. Indeed, the available data are not derived from experimental measurements, where the presence of noise or instrumental errors could justify the removal of outliers. On the contrary, each configuration in the dataset is obtained through numerical simulations and so all the values are physically plausible. For this reason, samples that lie outside the $\pm 3\sigma$ range are also kept.

Subsequently, before training the machine learning models, a feature engineering phase is carried out. To relate the beam lengths and the power output, the total sum and the symmetric indexes, already described in Table 4.5 and adopted in the second approach, are evaluated. For beam distances, on the other hand, it is observed that no obvious correlations emerge with the target variables. To enable the ML model to learn any complex relationships, the following new features are introduced in Table 4.9.

After the dataset construction and analysis, the next step consist on the training of the supervised machine learning models. In continuity with the approaches covered in the present project, the same regression models are employed: Random Forest Regressor (RFR), Gradient Boosting Regressor (GBRT) and XGBoost Regressor (XGBR). The goal is to exploit the predictive ability of these models to estimate the power extracted in configurations that have not yet been simulated.

Two different approaches are considered. The former consists of predicting a single output, namely the sum of the powers associated with the first four eigenfrequencies of the structure, denoted as P_{tot} . In this case, regression models are trained to directly predict this aggregate quantity, which is the quantity chosen to be maximized in the optimization. In the latter, on the other hand, the multi-output mode of the chosen machine learning models is exploited, training them to simultaneously predict the four values P_1 , P_2 , P_3 and P_4 . These values are then summed within the objective function of the genetic algorithm, still allowing for maximizing P_{tot} , , but with more detailed modeling of the structural response.

Feature Name	Formula	Description
Symmetry Pattern	$f = \begin{cases} 1 & \text{if } d_1 = d_3 \text{ and } d_2 > d_1 \\ 2 & \text{if } d_1 = d_3 \text{ and } d_2 < d_1 \\ 3 & \text{if } d_1 = d_2 = d_3 \\ 0 & \text{otherwise} \end{cases}$	Function to detect symmetries. Value 0 denotes asymmetry; 1 indicates symmetry with a larger central gap; 2 indicates symmetry with a smaller central gap; 3 denotes full symmetry.
Mean Distance	$\bar{d} = \frac{d_1 + d_2 + d_3}{3}$	Arithmetic mean of the three distances between adjacent beams. Useful to assess the overall compactness or spread of the structure.
$ d_1-d_2 $	$ d_1-d_2 $	Absolute difference between the first and second beam distances. Helps capture local asymmetry between the left and center sections.
$ d_2 - d_3 $	$ d_2-d_3 $	Absolute difference between the second and third beam distances. Highlights asymmetry between the center and right sections.
$ d_1 - d_3 $	$ d_1-d_3 $	Absolute difference between the first and third beam distances.

Table 4.9: Engineered features derived from the beam distances.

Similarly to the previous approaches, all the models are tuned through k-fold cross-validation with the same setting already explained.

Performance is measured using the metrics R_2 , Mean Absolute Error (MAE) and Mean Squared Error (MSE), accompanied by feature importance analysis and residual plots, which help the interpretation of accuracy and the selection of the model to be used within the genetic algorithm.

The predictions of the machine learning models is then employed as the fitness function within the genetic algorithm, with the goal of maximizing P_{tot} .

Again, two variants are developed.

The first is created to be used in the case where a single output machine learning model is employed. In this case, the objective function directly coincides with the direct prediction of P_{tot} . In the second variant, which takes advantage of multi-output prediction, the four predicted values are summed within the genetic algorithm itself, so that fitness is calculated with the same logic as in the single-output version.

In both approaches, physical constraints are imposed on the allowable configurations: beam lengths must remain between 80 and 100 mm, while the three beam distances must be such that their sum does not exceed the structure lateral width. The latter constraint is necessary to meet the overall dimensions of the device. To ensure that invalid configurations are automatically excluded during the search, a very severe penalty is applied within the fitness function. Specifically, if the sum of the distances exceeds the limit, a very low fitness value (-10^6 mW) is returned making that solution ineligible for evolutionary selection.

To evaluate the behavior of the optimization over time, the fitness history, or the trend of the maximum fitness value generation after generation, is plotted. This makes it possible to analyze the speed of convergence of the algorithm and its ability to explore the space of solutions.

Finally, given the high computational cost associated with generating more than 5,500

configurations through FEM simulations, a second analysis is also performed on a reduced dataset. In this case, 8 random combinations of lengths are selected, each of which is associated with 20 different combinations of distances. For each obtained configurations, only four resistance values are considered, randomly chosen within the previously defined range. This process leads to the creation of 640 configurations, which, when completed with the corresponding symmetric samples, bring the total to 700 samples. The entire pipeline is repeated on this subset as well, allowing the performance and robustness of the optimization to be compared with respect to the size of the dataset.

4.3.2 Numerical Results

Once the methodology of the third approach is outlined in Chapter 4.3.1, it is possible to report and discuss its results. As previously explained, the dataset is generated by combining different configurations of lengths and distances between beams, including symmetric configuration obtained by reflection. From these geometric variables, along with the value of electrical load resistance, numerical simulations are performed in COMSOL Multiphysics to calculate the power extracted from the structure at each of the first four resonant frequencies, named P_1 , P_2 , P_3 and P_4 . At the end a dataset of 5,460 samples is build, and in Table 4.10 are summarized all the considered input and output variables.

Type	Variable	Description
	L_1	First beam length
	L_2	Second beam length
	L_3	Third beam length
	L_4	Fourth beam length
	L_sum	Sum of all four beam lengths
	Index 1	Described in Table 4.5
	Index 2	Described in Table 4.5
Inputs	Index 3	Described in Table 4.5
Inputs	d_1	Spacing between the first and the second beam
	d_2	Spacing between the second and the third beam
	d_3	Spacing between the third and the fourth beam
	R	Resistive load
	symmetry_pattern	Described in Table 4.9
	\overline{d}	Average between the three beam distances
	$ d_1 - d_2 $	Absolute difference d_1 e d_2
	$ d_2 - d_3 $	Absolute difference d_2 e d_3
	$ d_1 - d_3 $	Absolute difference d_1 e d_3
	P_1	Extracted power with an excitation frequency equal to the first
		eigenfrequency
Output	P_2	Extracted power with an excitation frequency equal to the second
		eigenfrequency
	P_3	Extracted power with an excitation frequency equal to the third
		eigenfrequency
	P_4	Extracted power with an excitation frequency equal to the fourth
		eigenfrequency
	$P_{ m tot}$	Sum of the previous power values: $P_{\text{tot}} = P_1 + P_2 + P_3 + P_4$

Table 4.10: Input and output variables of the dataset used in the third approach

As previously described, an Exploratory data analysis (EDA) is conducted, which can be useful for understanding the distribution of the data and the possible presence of anomalous configurations. Specifically, all the independent input variables, that are L_1 , L_2 , L_3 , L_4 , d_1 , d_2 , d_3 and R, are analyzed along with the output quantity $P_{tot} = P_1 + P_2 + P_3 + P_4$ corresponding to the target variable used for optimization. For each of these variables, the mean value is reported, together with two bands corresponding to $\pm 3\sigma$, visually compared with the values of all the samples in the dataset.

This analysis shows that some samples fall outside the upper boundaries defined by $+3\sigma$. Particularly, this behavior is detected for some values of the variable d_2 , shown in Figure 4.15.(b). However, these values are still embedded within the physical constraints imposed during dataset generation, as described in the methodology. In fact, the sum of the three distances d_1 , d_2 and d_3 never exceeds the maximum allowable length of the structure, ensuring the physical validity of the configurations. Therefore, it is not considered appropriate to remove these samples, even if they were statistically far from the center of the distribution.

Similar considerations apply to the output $P_{\rm tot}$, where some samples show very high powers. Again, these are not outliers in the classical sense, since the data do not come from experimental measurements subject to noise or disturbances, but from controlled numerical simulations. Removing such samples would result in a significant loss of information, potentially going to eliminate precisely those optimal configurations that the optimization process aims to identify.

In light of these considerations, it is decided not to apply any kind of EDA based filtering. The entire dataset, including the original and engineered features, is used to train the machine learning models.

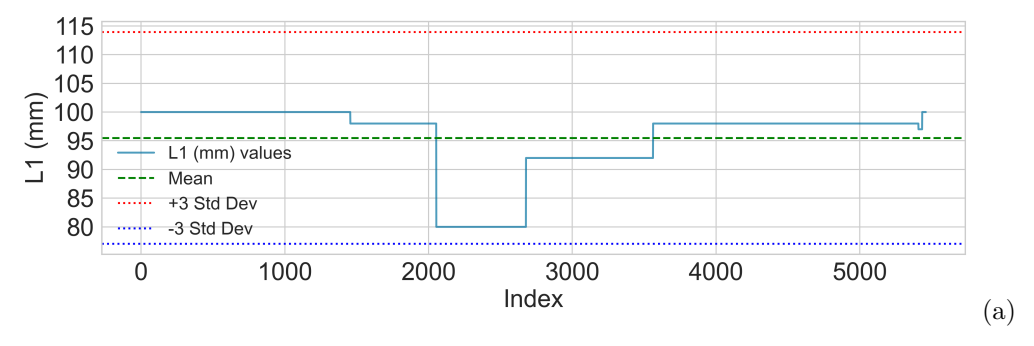
Once the data preparation step is completed, the dataset is subdivided into training and test set. Given the size of the complete dataset, consisting of 5,460 samples, a 50-50 split between train and test set is chosen, in order to reduce the possible risk of overfitting and allow for a more balanced comparison during validation.

Six different regression machine learning models are trained at this point. Three of these are the previously employed supervised ensemble models RFR, GBRT, and XGBR, each configured for direct prediction of the single output P_{tot} . The same models are then used in the multi-output configuration, in such a way that the four outputs P_1 , P_2 , P_3 , and P_4 are simultaneously predicted.

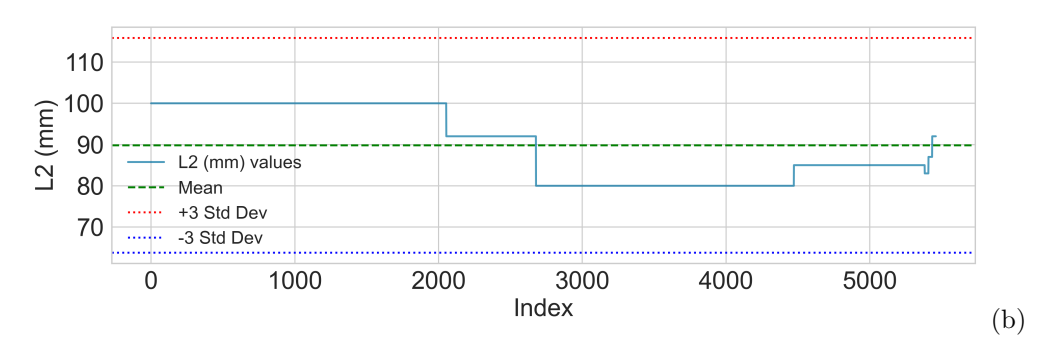
In each case, the hyperparameters tuning process is performed by the previously explained 5-fold cross-validation procedure, with the aim of ensuring robust estimation of model performance

Once the models are trained and tested is important to perform a comparison based on the performance, in terms of reliability of the machine learning model's predictions.

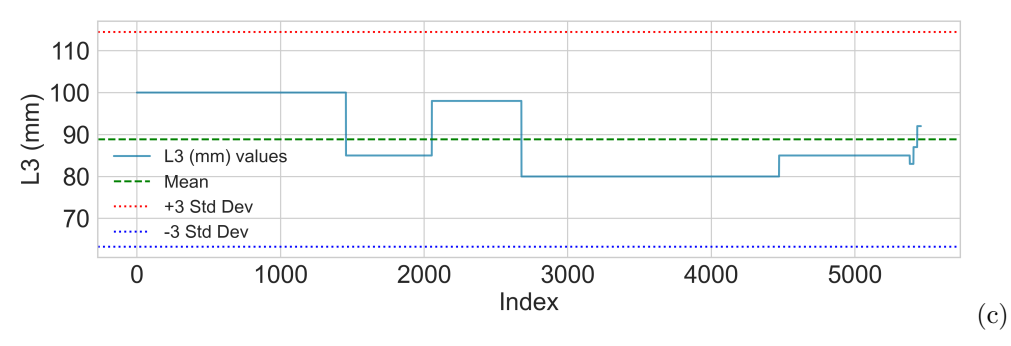
First of all, for each model the main performance metrics are analyzed and compared: the R-squared value R^2 , the mean absolute error MAE, and the mean square error MSE.



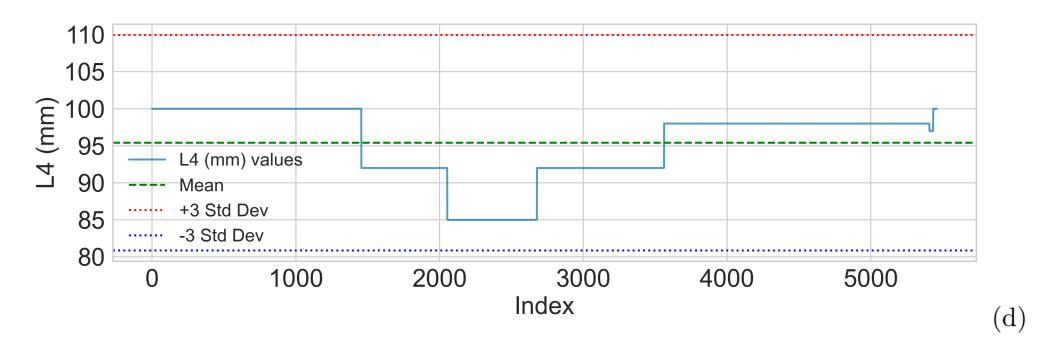
Distribution of variable L_1 with mean and thresholds $\pm 3\sigma$.



Distribution of variable L_2 with mean and thresholds $\pm 3\sigma$.

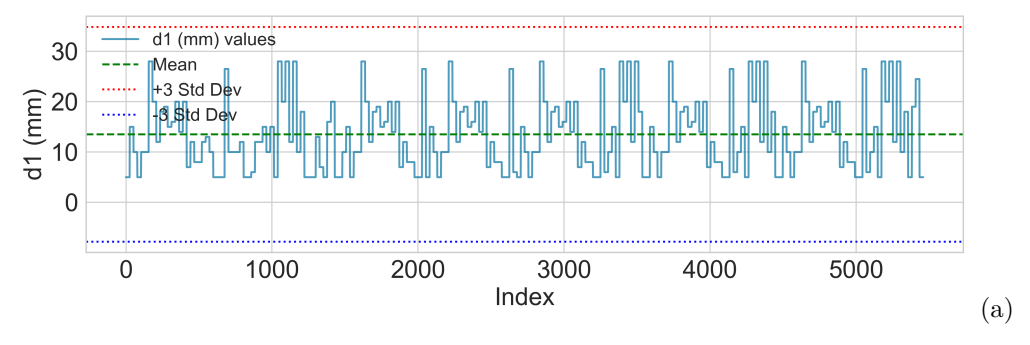


Distribution of variable L_3 with mean and thresholds $\pm 3\sigma$.

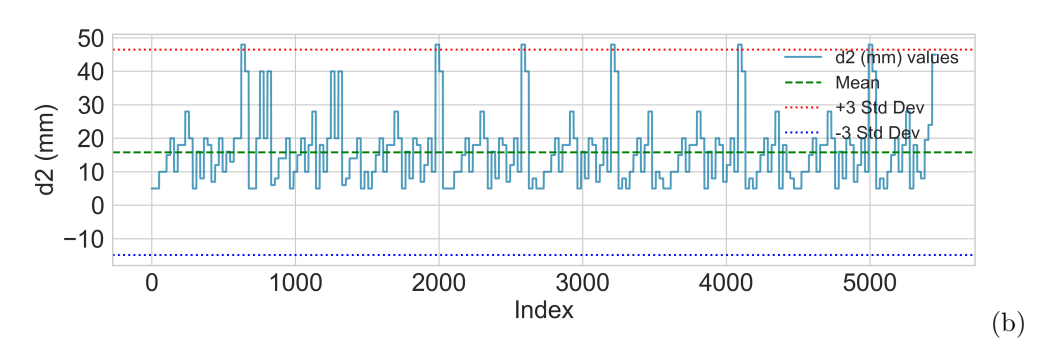


Distribution of variable L_4 with mean and thresholds $\pm 3\sigma$.

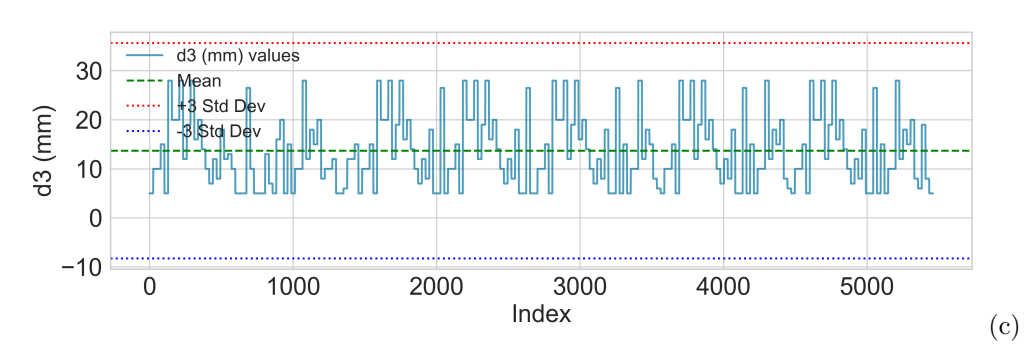
Figure 4.14: Exploratory data analysis of beam length variables $(L_1 \text{ to } L_4)$, showing the mean and thresholds at $\pm 3\sigma$.



Distribution of variable d_1 with mean and thresholds $\pm 3\sigma$.



Distribution of variable d_2 with mean and thresholds $\pm 3\sigma$.



Distribution of variable d_3 with mean and thresholds $\pm 3\sigma$.

Figure 4.15: Exploratory data analysis of inter-beam distance variables (d_1, d_2, d_3) , highlighting the distribution with mean and $\pm 3\sigma$ thresholds.

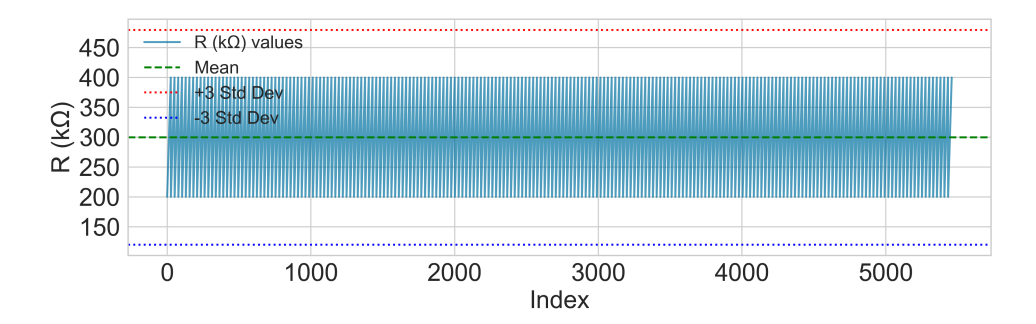


Figure 4.16: Exploratory data analysis of resistive load values, highlighting the distribution with mean and $\pm 3\sigma$ thresholds.

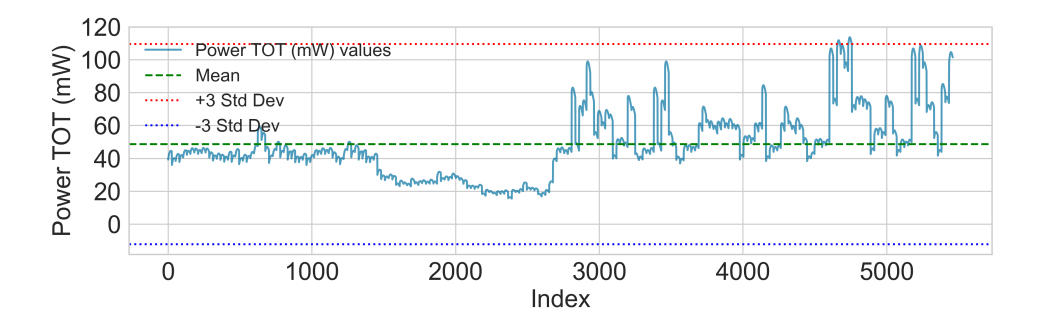


Figure 4.17: Exploratory data analysis of P_{tot} , highlighting the distribution with mean and $\pm 3\sigma$ thresholds.

Model	\mathbb{R}^2	MAE	MSE
RFR (Single Output)	0.98	0.33	1.03
GBRT (Single Output)	0.98	0.26	0.95
XGBR (Single Output)	0.98	0.22	0.41
RFR (Multi Output)	0.99	0.11	0.16
GBRT (Multi Output)	0.99	0.08	0.14
XGBR (Multi Output)	0.99	0.10	0.25

Table 4.11: Performance metrics for single-output and multi-output regression models: coefficient of determination (R^2) , Mean Absolute Error (MAE), and Mean Squared Error (MSE).

In Table 4.11 it is possible to clearly observe the performance obtained by the different models, both in single-output and multi-output configurations. In particular, it is noticed the multi-output models generally report better metrics, with a R^2 coefficient very close to the unit and significantly lower MAE and MSE values than the respective single-output versions. This suggests greater reliability of multi-output models in their ability to capture and represent the relationship between input variables and different power contributions, P_1 - P_4 .

In light of these results, the choice of the machine learning model to be used within the genetic algorithm definitely falls on a multi-output model. However, since the numerical performance reported by the three multi-output models are very close to each other, further analysis needs to be conducted to more consciously guide the final selection of the algorithm.

For this reason, the residual plots obtained for each multi-output model are compared. The graphical analyses of the residuals, shown in Figures 4.18, 4.19, 4.20 and 4.21, basically confirm what has already emerged from the numerical evaluation: all models show good predictive ability, however the differences are small and not sufficient to discriminate decisively between the three multi-output models. At this point, the feature importance analysis is performed in order to definitely choose for the genetic algorithm. This analysis is particularly useful in understanding whether and how each model was able to identify the most influential variables in the predictive process.

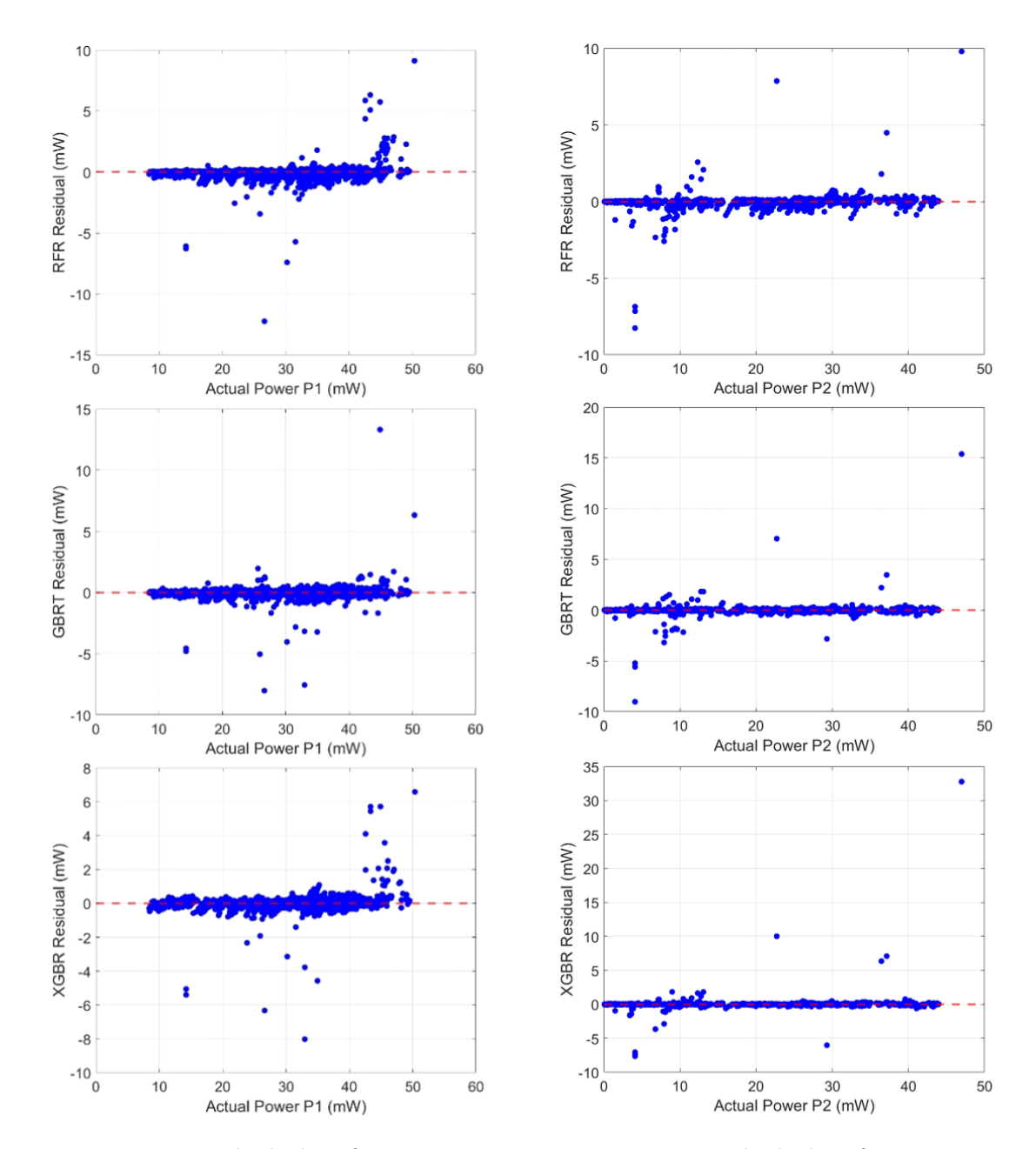


Figure 4.18: Residual plots for output P_1 performed with all the ML models.

Figure 4.19: Residual plots for output P_2 performed with all the ML models.

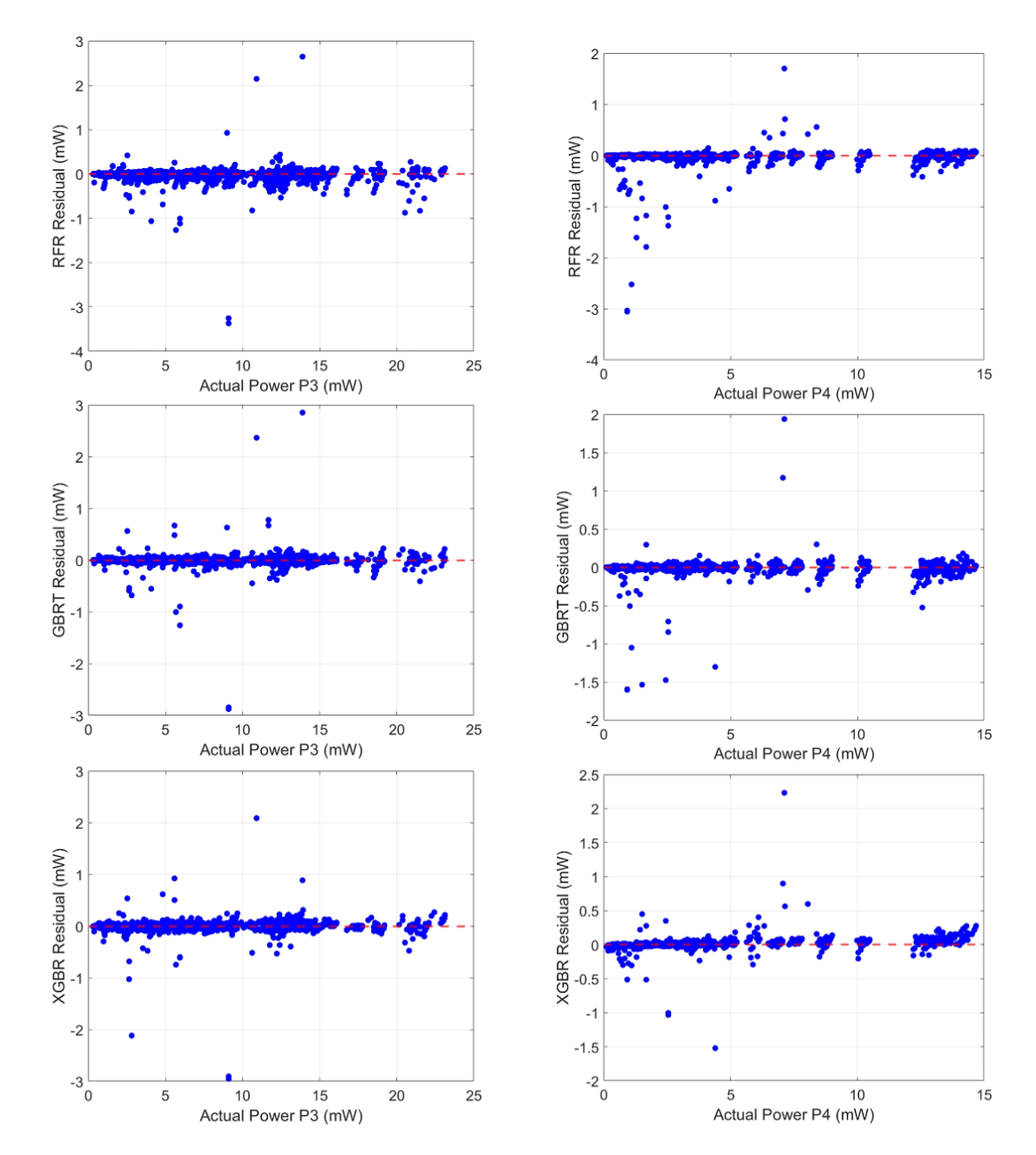


Figure 4.20: Residual plots for output P_3 performed with all the ML models.

Figure 4.21: Residual plots for output P_4 performed with all the ML models.

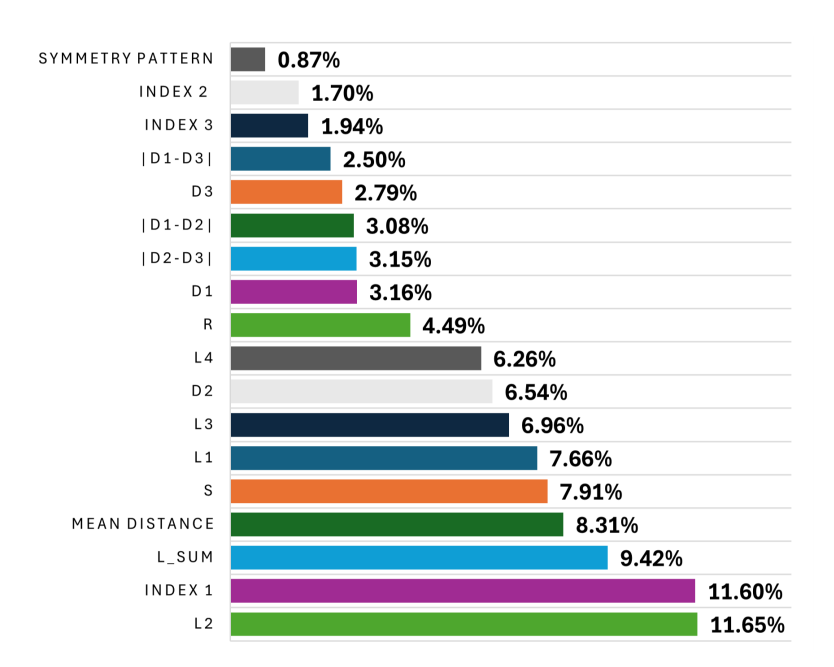


Figure 4.22: Feature importance for the Random Forest Regressor (multi-output).

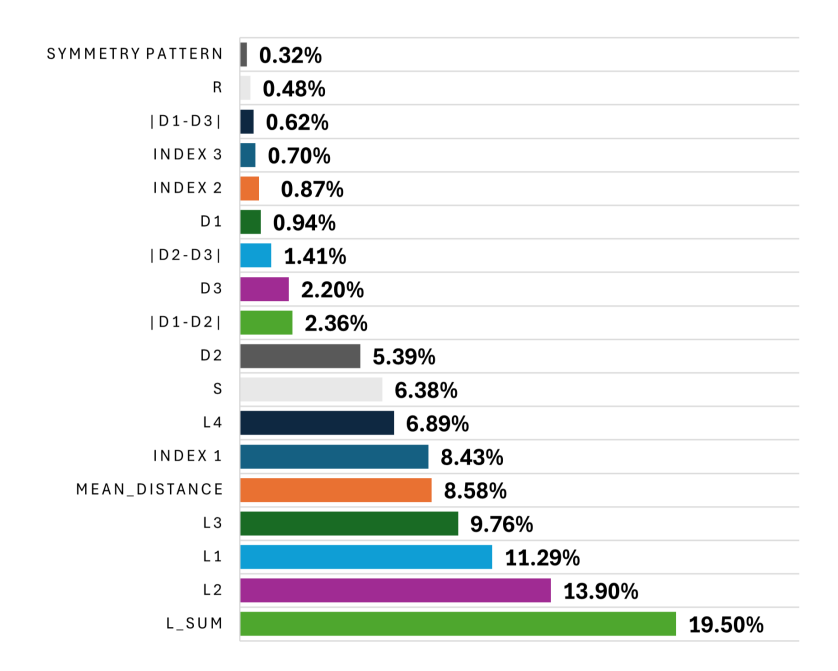


Figure 4.23: Feature importance for the Gradient Boosting Regressor (multi-output).

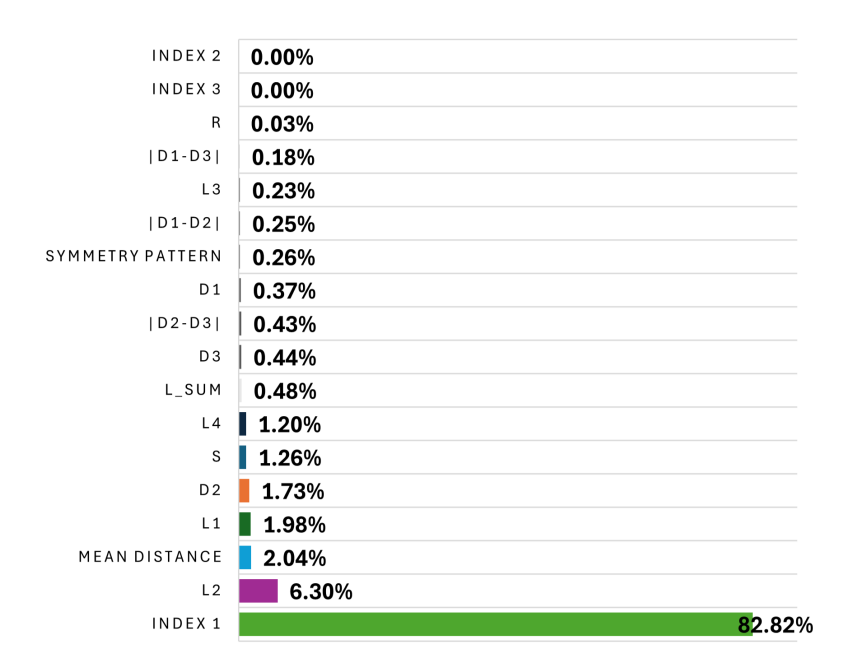


Figure 4.24: Feature importance for the XGBoost Regressor (multi-output).

Feature	RFR	GBRT	XGBR
Index1	12.47%	18.13%	89.11%
mean distance \bar{d}	12.33%	17.10%	3.76%
L_2	10.90%	22.83%	4.95%
L_sum	8.87%	9.93%	0.00%
d_2	7.75%	6.81%	0.58%
L_1	7.34%	5.29%	0.66%
L_4	6.25%	3.40%	0.00%
L_3	6.07%	2.44%	0.00%
R	4.53%	0.28%	0.01%
d_1	3.97%	0.60%	0.09%
$ d_2 - d_3 $	3.76%	1.21%	0.11%
d_3	3.59%	0.97%	0.01%
$ d_1 - d_2 $	3.46%	2.07%	0.32%
$ d_1 - d_3 $	3.18%	1.37%	0.03%
Index2	2.40%	2.38%	0.00%
Index3	2.04%	4.72%	0.00%
symmetry_pattern	1.09%	0.47%	0.37%

Table 4.12: Feature importance percentages (in %) for Random Forest Regressor (RFR), Gradient Boosting Regressor (GBRT), and XGBoost Regressor (XGBR) multi-output models, rounded to two significant figures.

Table 4.12 and Figures 4.22 4.23 4.24 show how XGBR model assign almost all importance to the "Index1" feature, which represents the central symmetry in beam lengths, while neglecting all other variables. This behavior indicates an oversimplification of the problem, where the prediction of outputs is mainly associated with lengths, at the expense of other potentially relevant features.

In contrast, both the RFR and GBRT model seem to more fully capture the expected behavior, assigning importance to both geometric length variables and distances between beams. This more balanced distribution of feature importance makes RFR and GBRT models more consistent with physical knowledge of the system. Additionally, it is consistent that the resistance value R has relatively low significance, since its range of variation is limited (between 200 and 400 k Ω). In fact, varying the resistive load in this limited range, the value of output powers have small relative variations for the same geometric configuration.

Considering all the results, it is noticed that RFR and GBRT models exhibit similar behavior in capturing the influence of variables on extracted powers, with a good ability to value both beam lengths and distances between them. However, GBRT shows slightly higher reliability metrics than RFR, especially in terms of predictive accuracy. For this reason, the prediction of GBRT model is chosen to be used as the objective function within the genetic algorithm, as it provides a good compromise between model predictive performance.

At this point, the genetic algorithm can be run using the multi-output GBRT model, selected for the previously explained reasons. Since the model can simultaneously predict the four outputs P_1 , P_2 , P_3 and P_4 , the adopted variant of the genetic algorithm is the second one described in Chapter 4.3.1. In fact, using the prediction of GBRT multi-output model, the sum of the four output powers needs to be performed within the fitness function. Summarizing, the chosen genetic algorithm has to generate a population with individuals characterized by a set of independent input variables (four beam lengths, three beam distances, and the load resistance) as a first step. Then within the fitness function, the derived input variables needed for prediction (e.g. average of distances, absolute differences, etc.) are calculated. Later, P_1 , P_2 , P_3 and P_4 are obtained for each individual through GBRT model prediction. Finally, the fitness function evaluates the sum of P_1 , P_2 , P_3 and P_4 named as P_{tot} . In this way, for each individual the fitness function returns its P_{tot} , which is the quantity to be maximized.

As discussed earlier, the goal of the process is to achieve a structural configuration that maximizes peak power at the first four eigenfrequencies. This makes it possible to take advantage of the multimodal nature of the system, extending its operational and energy-efficient range.

At the end of the optimization, an optimal configuration is obtained, shown in Table 4.13, accompanied by a fitness history graph (Figure 4.25) showing the evolution of the solution during the genetic algorithm iterations.

Parameter	Starting structure	Optimal configuration (GA)
$L_1 \text{ (mm)}$	80	100
$L_2 \text{ (mm)}$	90	92
L_3 (mm)	100	92
$L_4 \text{ (mm)}$	85	100
$d_1 \text{ (mm)}$	10	5
$d_2 \text{ (mm)}$	10	44.5
d_3 (mm)	10	6
$R(k\Omega)$	302	278
Predicted Power (mW)	23.02	108.05
Simulated Power (mW)	20.99	105.59

Table 4.13: Comparison between the initial and the optimized configuration using the third approach with the multi-output GBRT model. Power values refer to the sum of the extracted powers over the first four eigenfrequencies.

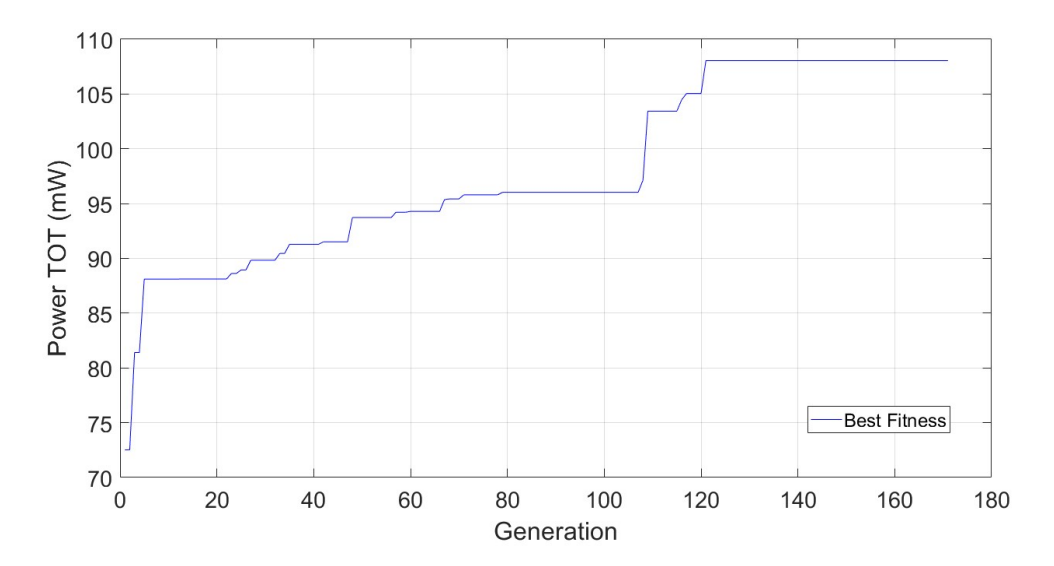


Figure 4.25: Third approach: Evolution of the best fitness value across genetic algorithm iterations.

From Table 4.13, it can be seen that once the optimized configuration is obtained through the genetic algorithm based on the GBRT multi-output model, it is decided to validate its performance through FEM simulations on COMSOL. In particular, the geometrical parameters and the resistive load of the optimized structure are set in COMSOL Multiphysics, and two consecutive studies are performed. The former, is an eigenfrequency study to find the first four eigenfrequencies of the structure. The latter, is a frequency domain study in which the excitation frequency is set to the first four previously found eigenfrequencies, so as to calculate the energy output for each mode. This numerical simulation is performed under a restricted resistance sweep to verify that the optimal value suggested by the optimization model for the resistive load $(278 \text{ k}\Omega)$ actually

corresponds to one that maximizes P_{tot} for that specific geometrical structure.

From the simulation, it is observed that, for the optimized configuration and at the resistance of 278 k Ω , the total power is 105.59 mW, compared with the GBRT model prediction of 108.05 mW. The relative error between the predicted and simulated value is equal to:

$$\frac{|108.05 - 105.59|}{105.59} \cdot 100 \approx 2.33\% \tag{4.5}$$

In addition, the variation of the sum of P_1 , P_2 , P_3 and P_4 , named as P_{tot} , with respect to the variation of the resistive is analyzed and reported in Figure 4.26. The resulting curve shows a maximum at 301 k Ω , with a sum of powers P_{tot} equal to 105.86 mW. Therefore, the optimization process experiences an error in the placement of the maximum of:

$$\frac{|301 - 278|}{278} \cdot 100 \approx 8.27\% \tag{4.6}$$

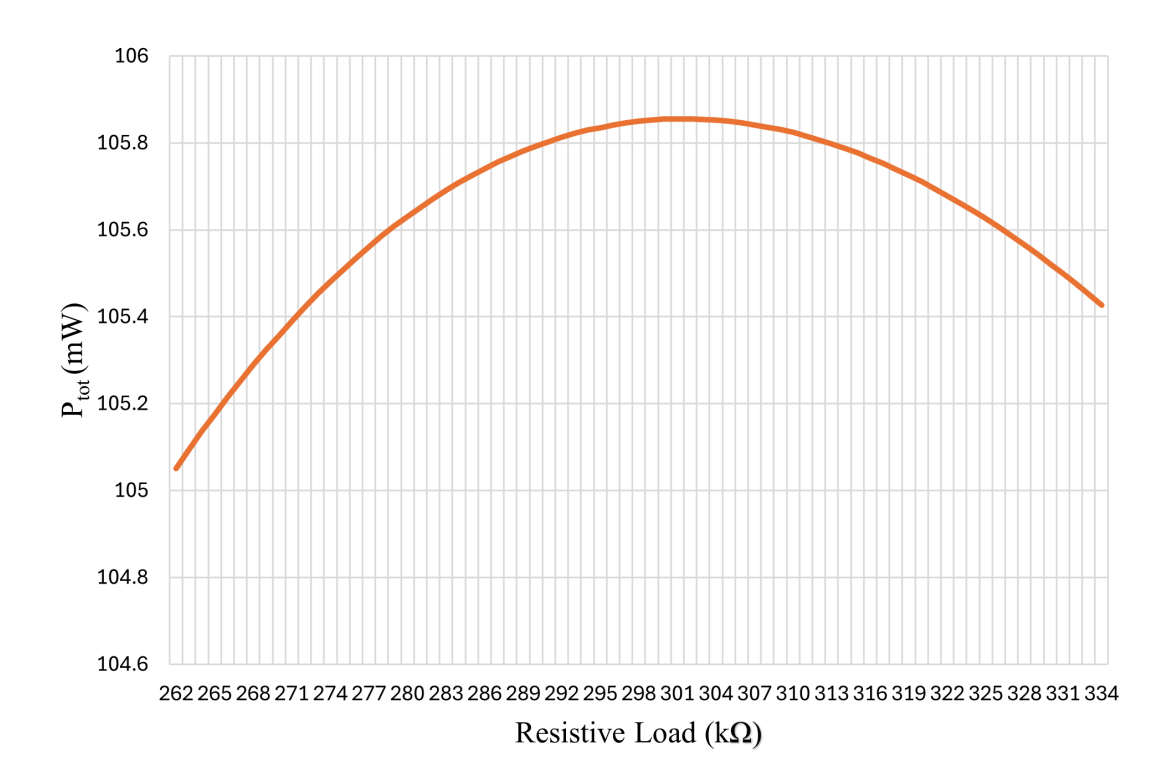


Figure 4.26: P_{tot} versus Resistive load of the optimized structure: vertical axis is P_{tot} expressed in mW and horizontal axis represents the resistive load R expressed in k Ω

Once the configuration optimized by the genetic algorithm is obtained and the errors between predicted and simulated powers are evaluated, some relevant considerations can be drawn.

First of all, the obtained configuration is consistent with the feature importance analysis (Figure 4.23) discussed above. Indeed, the multi-output GBRT machine learning model assigns greater importance to variables related to beam lengths (particularly Index1) than to the distances between them. It is therefore not surprising that the optimal configuration found with the third approach has the same lengths as the optimal structure already identified in the second approach. The ability to modify the spacing between the beams, enabled by the third approach, allows greater flexibility in further improving the performance of the system. In fact, comparing the optimized configuration obtained with the second approach and that obtained with the third approach, an increase in extracted power is observed in all four cases where the excitation frequency coincides with one of the first four eigenfrequencies, as shown in Table 4.14.

Variable	Second approach optimal structure	Third approach optimal structure
$L_1 \text{ (mm)}$	100	100
$L_2 \text{ (mm)}$	92	92
$L_3 \text{ (mm)}$	92	92
$L_4 \text{ (mm)}$	100	100
$d_1 \text{ (mm)}$	10	5
$d_2 \text{ (mm)}$	10	44.5
$d_3 \text{ (mm)}$	10	6
$R(k\Omega)$	320	301
P_1 (mW)	45.79	49.72
$P_2 \text{ (mW)}$	5.93	43.58
P_3 (mW)	1.45	7.79
$P_4 \text{ (mW)}$	0.49	4.75
P_{tot} (mW)	53.66	105.86

Table 4.14: Output powers comparison $(P_1, P_2, P_3, P_4, \text{ and } P_{tot})$ between the optimal structure obtained with the Second Approach and the one obtained with the Third Approach.

However, when analyzing the relative prediction errors calculated in the Equations 4.5 and 4.6, although they are relatively small, a significant limitation of the model emerges. In particular, considering that from the analysis of the feature importance the distance d_2 turns out to be among the most influential parameters, it is decided to test a configuration slightly modified from that proposed by the genetic algorithm. In this variant, the lengths are kept the same ($L_1 = 100$, $L_2 = 92$, $L_3 = 92$, $L_4 = 100$), but the value of d_2 is increased to 46 mm, fixing instead $d_1 = d_3 = 5$ mm. In this way, a maximization of the distance between the central beams d_2 is imposed and, at the same time, a central symmetry is also set for the spacing between the beams. This choice is consistent with the previously identified correlation between symmetry in beam lengths and increased output power, and it is therefore decided to test whether symmetry in spacing would also provide benefits. Specifically it is decided to set d_1 and d_3 at the same length to ensure the symmetry of the structure, and with a value corresponding the lower boundary value that is 5 mm. This constraint allows d_2 to reach the highest possible value. In fact, d_2 is maximized up to 46 mm, which is the maximum value compatible with the geometric constraint that

requires the four beams to be entirely contained within the plate, while still maintaining a space s of 1 mm between the extreme beams and the edges of the plate. This margin is necessary to avoid constructional problems in the practical realization of the device.

The same simulation process is carried out for this configuration: eigenfrequency study, followed by frequency domain study with sweep of the resistances. The maximum powers extractable from the structure are reported in Table 4.15.

Variable	Modified structure
$L_1 \text{ (mm)}$	100
$L_2 \text{ (mm)}$	92
$L_3 \text{ (mm)}$	92
$L_4 \text{ (mm)}$	100
$d_1 \text{ (mm)}$	5
$d_2 \text{ (mm)}$	46
$d_3 \text{ (mm)}$	5
$R(k\Omega)$	300
$P_1 \text{ (mW)}$	49.82
$P_2 \text{ (mW)}$	45.22
P_3 (mW)	7.89
$P_4 \text{ (mW)}$	5.03
P_{tot} (mW)	107.96

Table 4.15: Output powers $(P_1, P_2, P_3, P_4, \text{ and } P_{tot})$ of the modified structure.

From Table 4.15, it can be seen that the modified configuration provides higher overall power values than those obtained from the structure proposed by the genetic algorithm. This result shows that the optimization process is not reliable enough to ensure that the global optimal structure is found. This limitation can be attributed to the complexity of the structural behavior with respect to the number and nature of variables involved, which may not allow the model to fully learn the relationship between the geometry and the extracted power.

However, the algorithm demonstrates a good ability to capture the overall trend, leading toward a configuration capable of generating significantly more power than the initial structure. Although the globally optimal solution is not obtained, the result can still be considered extremely positive and useful in directing the design toward promising configurations.

Having obtained the modified structure, derived from that proposed by the optimization process using machine learning combined with genetic algorithm, a more in-depth analysis of its dynamic characteristics is performed. In particular, this analysis is in relation to the structure's modes of vibrations, frequency response and stress distribution.

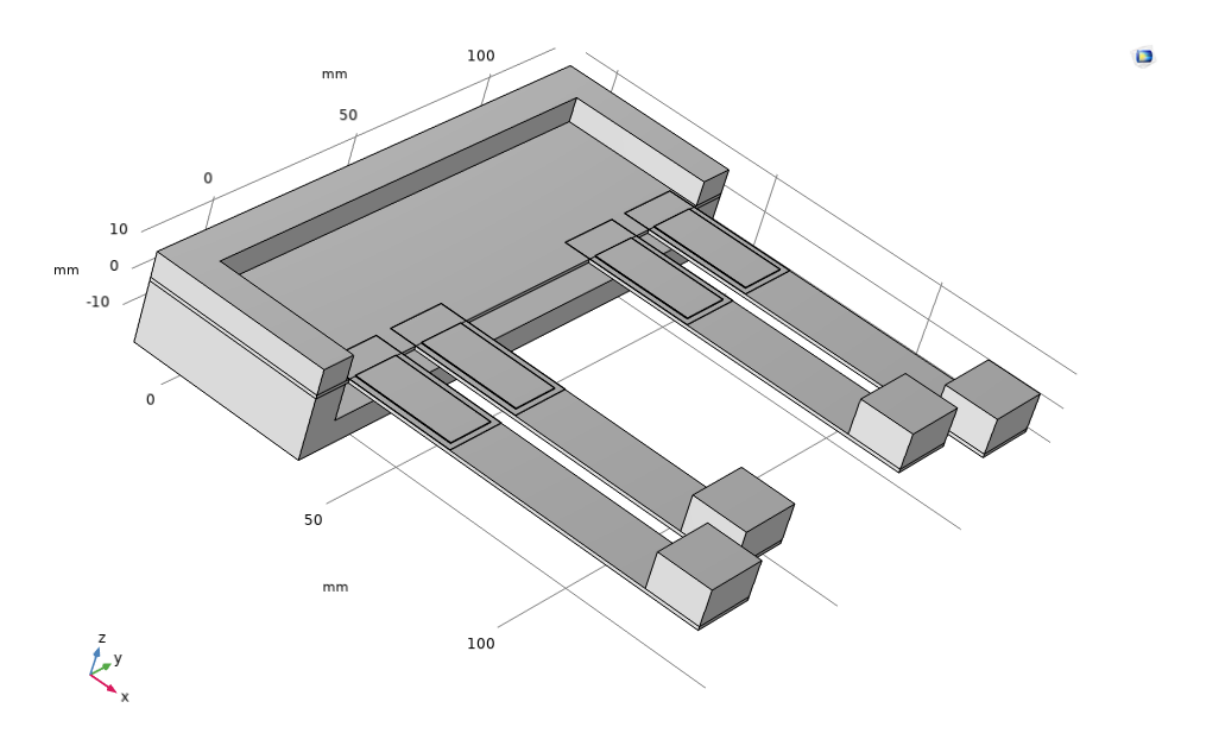
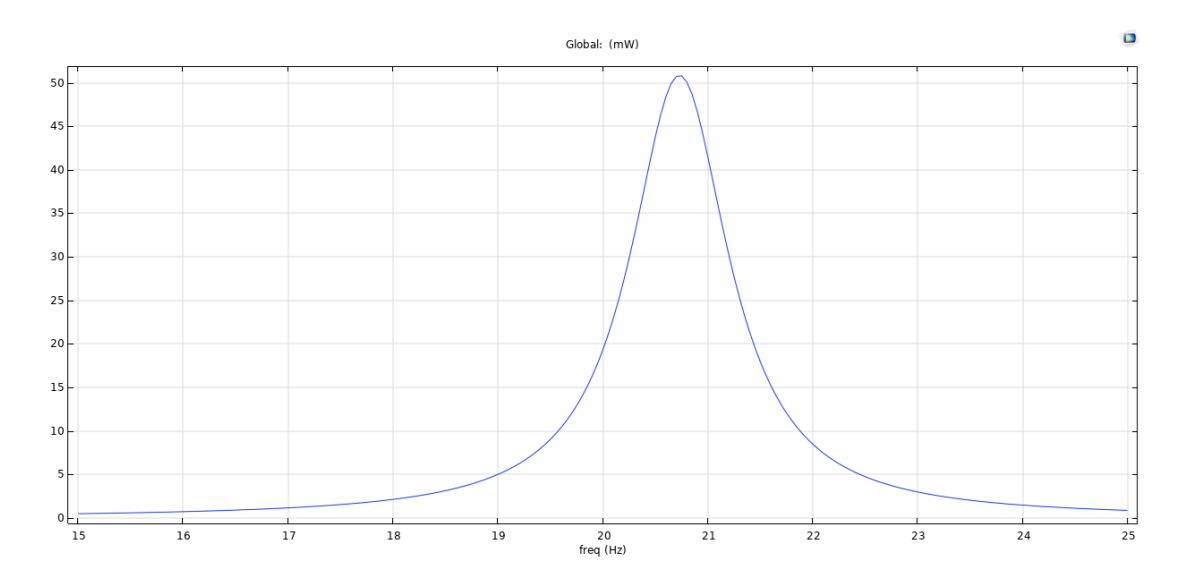


Figure 4.27: Geometrical configuration of the energy harvester obtained by modifying the structure obtained with the third approach optimization.

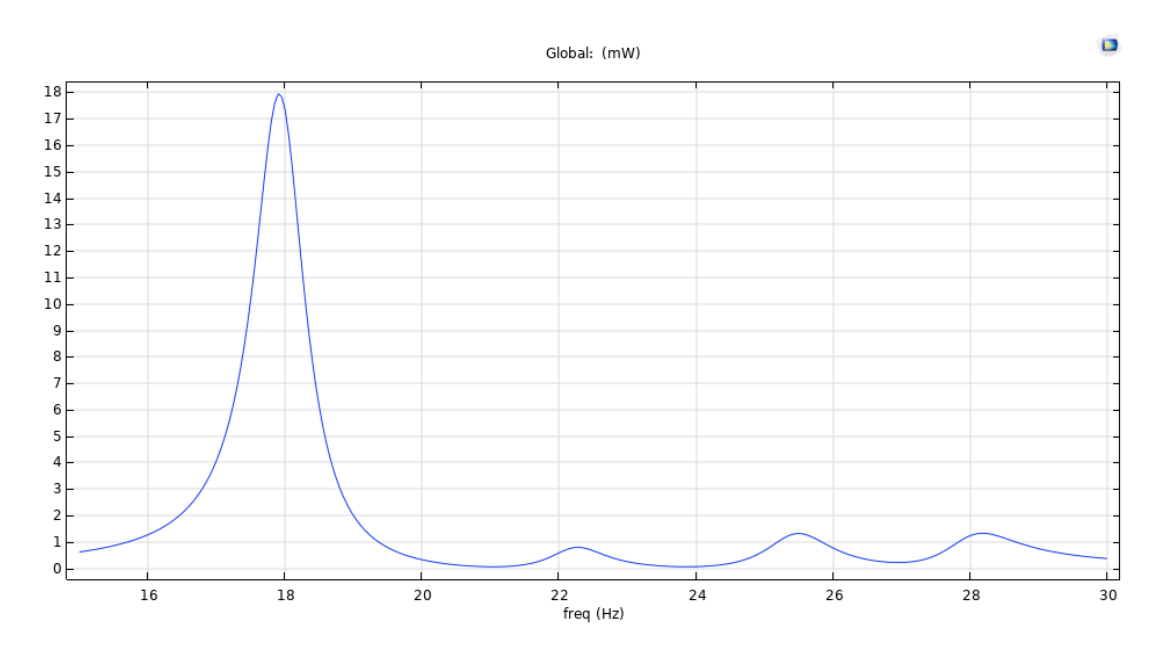
The first relevant observation concerns the first four eigenfrequencies of the structure, shown in Table 4.16. As can be seen, these frequencies are very close between each other, a characteristic that significantly affects the overall dynamic response of the system.

Variable	Modified structure	Starting structure
$L_1 \text{ (mm)}$	100	80
$L_2 \text{ (mm)}$	92	90
$L_3 \text{ (mm)}$	92	100
$L_4 \text{ (mm)}$	100	85
$d_1 \text{ (mm)}$	5	10
$d_2 \text{ (mm)}$	46	10
$d_3 \text{ (mm)}$	5	10
$R(k\Omega)$	300	302
$\lambda_1 \text{ (Hz)}$	20.811	17.90
$\lambda_2 \text{ (Hz)}$	20.93	22.20
λ_3 (Hz)	22.054	25.40
$\lambda_4 \; (\mathrm{Hz})$	22.44	27.90

Table 4.16: First four resonance frequencies (eigenfrequencies) of the modified and starting structure, namely λ_1 , λ_2 , λ_3 and λ_4 .



(a) Extracted power curve as a function of the excitation frequency of the modified final structure.



(b) Extracted power curve as a function of the excitation frequency of the starting structure.

Figure 4.28: Comparison between extracted power curves of the modified final structure (a) and the starting structure (b).

In order to better analyze this aspect, a frequency domain study in COMSOL Multiphysics is conducted, in which the harmonic excitation is varied from 15Hz to 25Hz with a very fine step of 0.05Hz, so as to precisely cover the entire range of the first four eigenfrequencies. Figure 4.28.(a) reports the extracted power curve as a function of the excitation frequency.

The behavior of the modified structure is then compared with that one of the initial structure (with lengths L = [80, 90, 100, 85] mm and distances d = [10, 10, 10] mm) subjected to the same type of study. The corresponding response curve is shown in Figure 4.28.(b). Comparing the two curves, substantial differences show up.

In particular, the starting structure shows four distinct peaks at the first four resonance frequencies, showing a broader range of application in terms of excitation frequency. However, only the first mode generates a significant amount of power, while the other three have much smaller peaks, as also numerically reported in Table 4.17.

Variable	Starting structure
$L_1 \text{ (mm)}$	80
$L_2 \text{ (mm)}$	90
$L_3 \text{ (mm)}$	100
$L_4 \text{ (mm)}$	85
$d_1 \text{ (mm)}$	10
$d_2 \text{ (mm)}$	10
$d_3 \text{ (mm)}$	10
$R(k\Omega)$	302
$P_1 \text{ (mW)}$	17.67
$P_2 \text{ (mW)}$	0.79
$P_3 \text{ (mW)}$	1.30
$P_4 \text{ (mW)}$	1.22
$P_{tot} \text{ (mW)}$	20.99

Table 4.17: Output powers $(P_1, P_2, P_3, P_4, \text{ and } P_{tot})$ of the starting structure.

On the other hand, the modified structure exhibits a different behavior: the four peaks associated with the vibration modes merge into a single continuous interval with high efficiency, due to the close proximity of the four eigenfrequencies, as reported in Table 4.16. Even though the multiple peaks are no longer found, the extracted power markedly higher. This observation is also confirmed by analyzing the modal shapes of the structure associated with the first four eigenfrequencies, shown in Figure ??.

Figure 4.29 and Figure 4.30 show that there are no radical differences as the excitation frequency changes. However, it is observed that the beams move synchronously, with coherent and coordinated oscillations. This synchronous behavior is particularly favorable in terms of maximizing the electrical power generated, as it allows minimizing the effects of voltage cancellation between the individual piezoelectric elements, thus maximizing the net contribution to the external load.

Nevertheless, although the overall value of the extracted power is significantly higher than in the initial structure, at first glance the frequency range of application appears to be narrower.

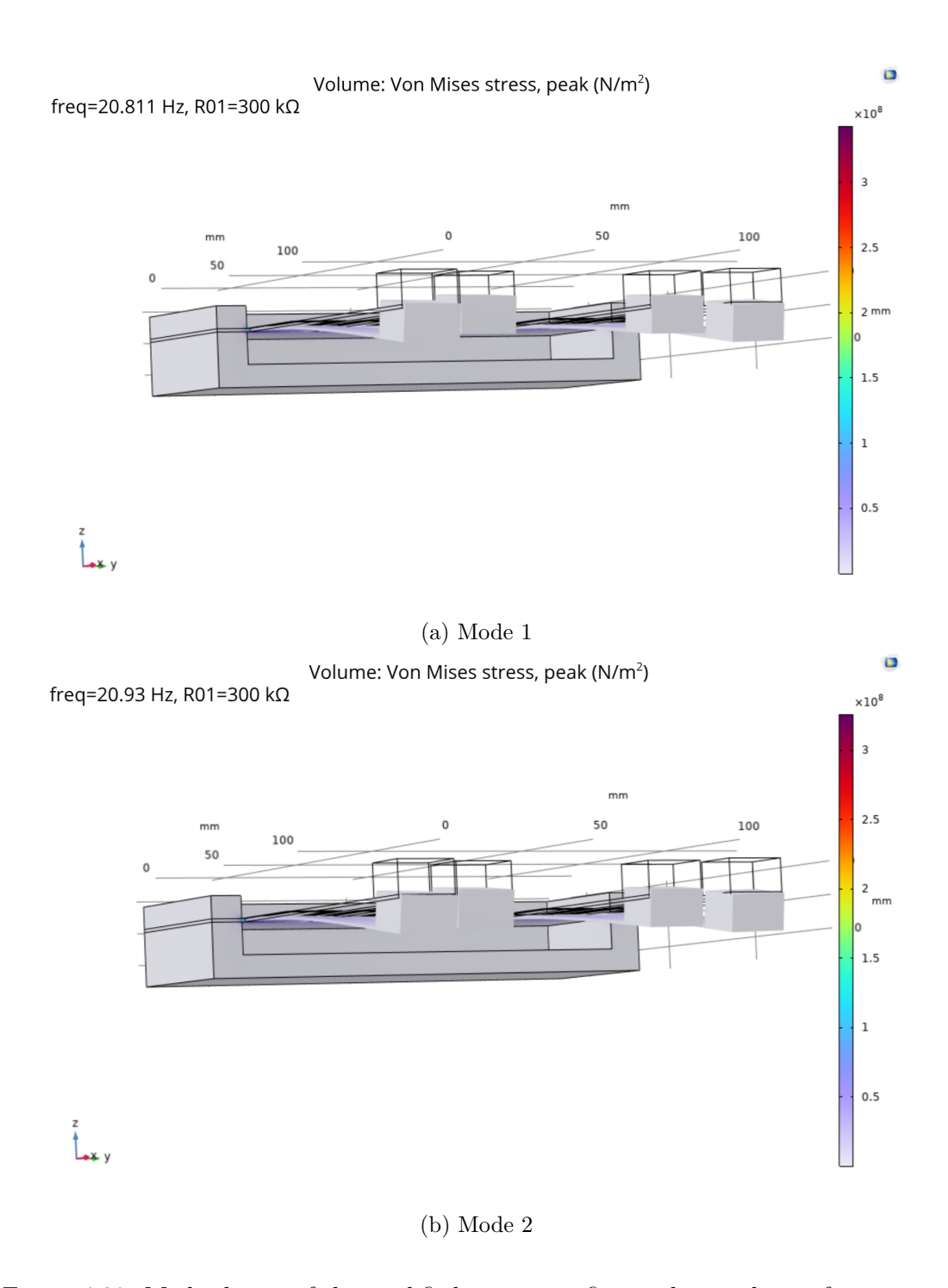


Figure 4.29: Mode shapes of the modified structure: first and second eigenfrequencies.

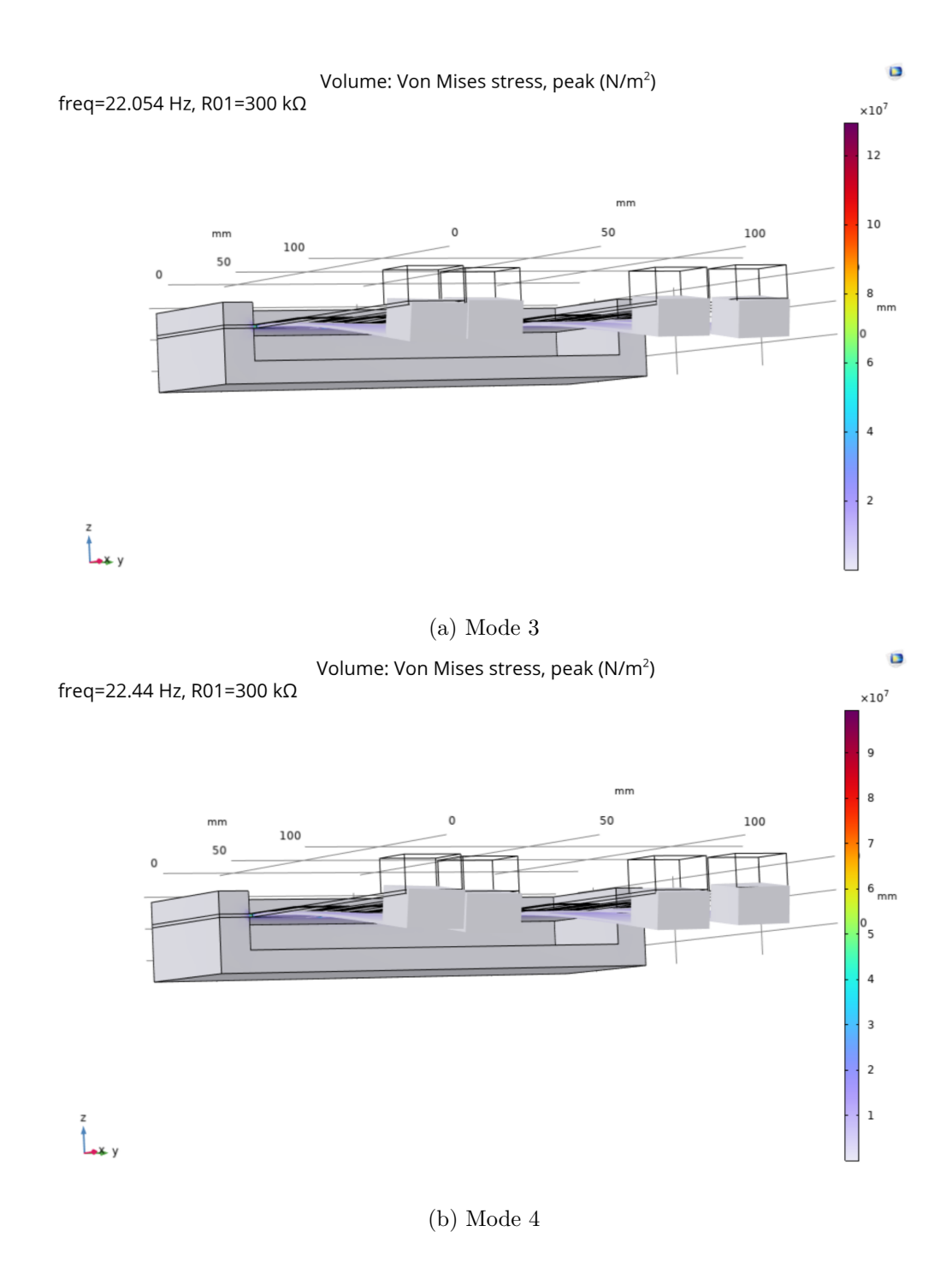


Figure 4.30: Mode shapes of the modified structure: third and fourth eigenfrequencies.

To deepen the analysis, the spectral amplitude of the power peaks is evaluated using the 3 dB criterion [35]. According to this method, the frequency range is defined as the interval in which the extracted power curve is above half of the peak power in linear scale, which corresponds to $P_{\rm max}-3$ dB in logarithmic scale.

In the case of the initial structure, the first peak is considered, since the other three are negligible in terms of output power. Instead, for the modified structure, the only visible broad peak, given by the superposition of the four modes, is analyzed.

So, once the maximum extracted power is extracted for both the curves shown in Figure 4.28, the threshold power is evaluated throw the following equation.

$$P_{threshold} = P_{max}/2 (4.7)$$

Subsequently, the frequencies f_1 and f_2 are evaluated. These frequencies are obtained by intersecting the power versus excitation frequency curve with an horizontal line equal to $P_{threshold}$.

$$P(f_1) = P(f_2) = P_{threshold} \tag{4.8}$$

Finally the frequency range $\Delta f = f_2 - f_1$ is evaluated for both the configuration, and results are reported in Table 4.18.

Variable	Starting structure	Modified structure
$L_1 \text{ (mm)}$	80	100
$L_2 \text{ (mm)}$	90	92
$L_3 \text{ (mm)}$	100	92
$L_4 \text{ (mm)}$	85	100
$d_1 \text{ (mm)}$	10	5
$d_2 \text{ (mm)}$	10	45
$d_3 \text{ (mm)}$	10	5
$R(k\Omega)$	320	300
f_1 (Hz)	17.61	20.30
f_2 (Hz)	18.2	21.10
Δf (Hz)	0.59	0.80

Table 4.18: Amplitude comparison of the power versus excitation frequency curves between the starting and the modified structure.

From these results it is clearly visible that, although the modified structure has a single main peak, the value Δf in which high efficiency is maintained is wider with respect to the starting structure.

Moreover, although the starting structure has power peaks at frequency values as high as 27.9 Hz, the output power at second, third and fourth peak is very low. In fact, by analyzing the power extracted from the modified structure when the excitation frequency is equal to the second, third and fourth eigenfrequencies of the initial structure, a direct comparison can be made between the two configurations.

From the table 4.19 some important considerations can be drawn. First, it is evident that the modified structure has a narrower practically usable frequency range than

Variable	Starting structure	Modified structure
$L_1 \text{ (mm)}$	80	100
$L_2 \text{ (mm)}$	90	92
$L_3 \text{ (mm)}$	100	92
$L_4 \text{ (mm)}$	85	100
$d_1 \text{ (mm)}$	10	5
$d_2 \text{ (mm)}$	10	46
$d_3 \text{ (mm)}$	10	5
$R(k\Omega)$	302	300
P at 17.9 Hz (mW)	17.67	1.98
P at 22.2 Hz (mW)	0.79	6.59
P at 25.4 Hz (mW)	1.30	0.71
P at 27.9 Hz (mW)	1.22	0.29

Table 4.19: Comparison of the power extracted from the two configurations (starting structure and modified structure) at the eigenfrequencies of the initial structure (17.9, 22.2, 25.4 and 27.9 Hz)

the initial structure. This is particularly evident at the excitation frequency of 17.9 Hz (the first eigenfrequency of the starting structure), where the power extracted by the modified structure is almost zero, while the initial structure reaches a maximum value of 17.67 mW. However, looking at the results at the subsequent frequencies (corresponding to the second, third and fourth resonance frequencies of the initial structure), an interesting behavior can be seen: even in the absence of a corresponding peak, the modified structure manages to maintain competitive, and in some cases higher, values of extracted power. Specifically, at 22.2 Hz (the second eigenfrequency of the initial structure), the power extracted by the modified structure is 6.59 mW, a value significantly higher than only 0.79 mW of the starting structure.

Overall, this comparison confirms that the optimization resulted in an increase in overall power extracted around the main peak, but at the price of increased spectral selectivity, with a less effective response away from the central range. Therefore, the versatility of the final structure in applications where environmental vibrations are variable in a larger range is reduced. However, since no precise application area has been defined in the present thesis project for the analyzed energy harvester, it is not possible to determine in absolute terms whether a more efficient but less versatile structure is preferable to one with lower power but wider operating bandwidth. Indeed, the final assessment depends on the specific context in which the device is used. Nevertheless, from a methodological point of view, it is important to note that if an application domain is defined, the entire optimization process can be adapted to take into account the desired operating range as well. For example, the objective function of the genetic algorithm could be modified by introducing a penalty for structures with narrow frequency ranges, thus improving the model's fit to real-world needs. Finally, the distribution of mechanical stresses in the modified structure is analyzed, focusing on the most critical condition, which is the one in which the excitation frequency coincides with the first eigenfrequency, since from Table 4.15 it turns out to be the one at which the maximum power is extracted.

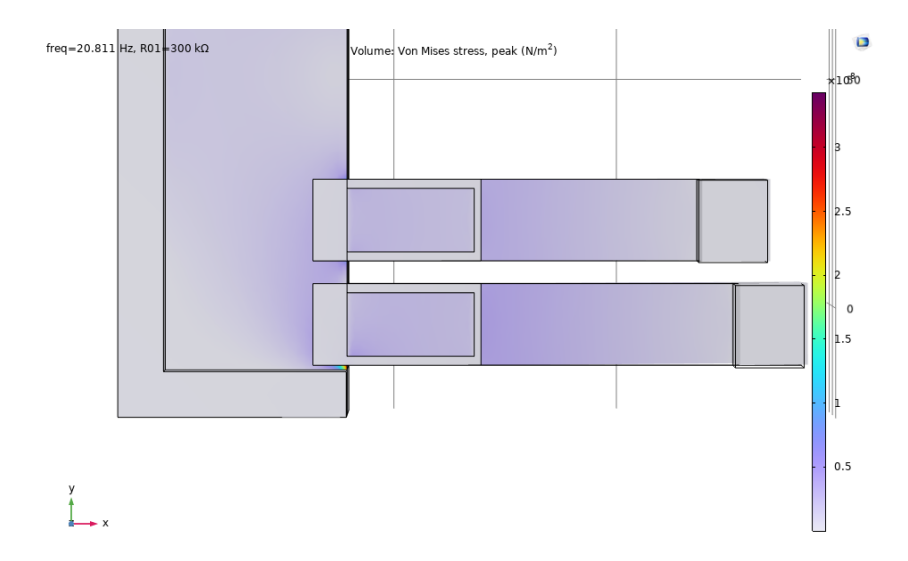


Figure 4.31: Von Mises stress distribution of the modified configuration when excited at its first eigenfrequency.

Figure 4.31 shows the stress map for that condition. It is observed that the maximum value is concentrated, as expected, near the junction between the extreme beams and the support plate, with a maximum value of about 200 MPa. As observed in the stress analysis of the structure optimized with the second approach in Chapter 4.2.2, this stress value is is within the yield strength limits of common structural aluminum alloy materials. Therefore, it can be reasonably concluded that, unless pure or high-purity aluminum is used, the structure is able to withstand the expected harmonic excitation while remaining in the elastic range, thus ensuring the mechanical safety of the system.

At the end, the final step is to perform the optimization with a reduced dataset. As already described in Chapter 4.3.1, the reduced dataset is obtained by randomly selecting a subset of the samples generated in the full dataset. Specifically, 8 random combinations of lengths are selected, each of which is associated with 20 different combinations of distances. For each configuration thus obtained, only four resistance values are considered, randomly chosen within the defined range. This process resulted in the generation of 640 configurations, which becomes 700 total samples by including symmetrical configurations.

Again, the reduced dataset is used to train the multi-output GBRT model directly, maintaining the same training settings adopted in the previous phase. The model accuracy is evaluated through the same evaluation metrics $(R_2, MAE \text{ and } MSE)$.

Model	\mathbb{R}^2	MAE	MSE
GBRT (Multi Output)	0.97	0.44	0.54

Table 4.20: Performance metrics for multi-output GBRT model trained with a reduced dataset: coefficient of determination (R^2) , Mean Absolute Error (MAE), and Mean Squared Error (MSE).

The performance results of the model reported in table 4.20, show satisfactory performance, with values of R^2 , MAE and MSE confirming the validity of the approach, despite the significant reduction in the number of samples.

However, as discussed earlier, such metrics can be misleading. This is because, for each geometric configuration, different values of the resistance R are considered, which often result in low variations in the value of power extracted. As a result, there may be configurations in the test set that are almost identical to those seen during training, but with slightly different resistance. This facilitates model predictions, positively influencing the metrics without necessarily reflecting a real ability to generalize. For this reason, rather than focusing exclusively on accuracy metrics, it is useful to analyze the distribution of feature importance. This analysis allows to check whether the model, despite using a reduced dataset, is still able to capture the same structural relationships learned in the case of training with the full dataset.

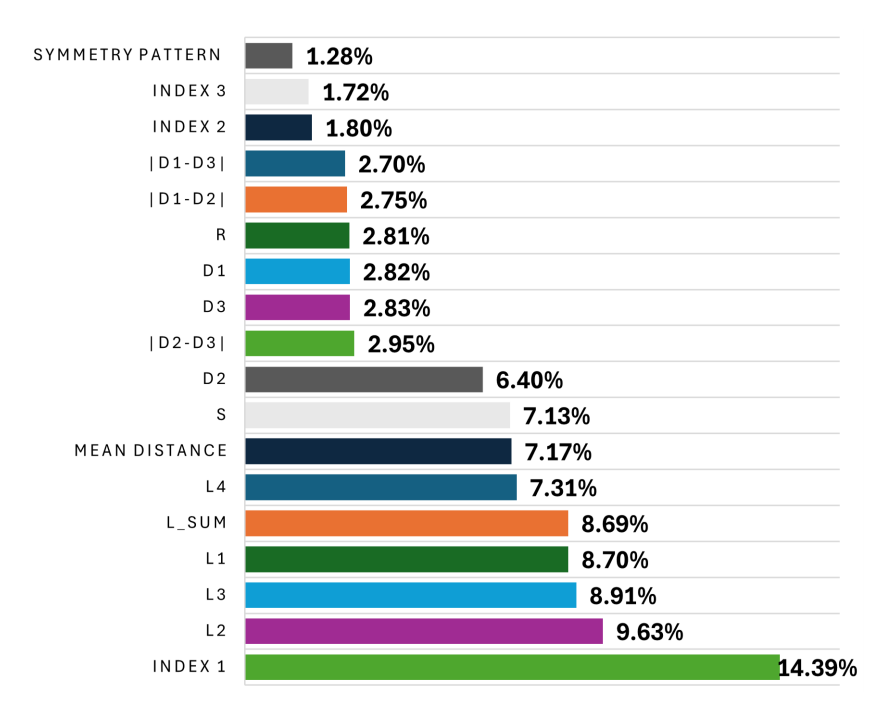


Figure 4.32: Feature importance for the Gradient Boosting Regressor (multi-output) trained with reduced dataset.

Figure 4.32 shows that the feature importance obtained during training is consistent with that observed in the full dataset, confirming the stability of the information learned by the model.

Subsequently, the genetic algorithm is applied using the GBRT model trained on reduced dataset. The objective function of the genetic algorithm is the same as the one previously described for the full dataset.

From Table 4.21 it can be observed that the optimized configuration using the machine learning model trained on the reduced dataset gives significantly incorrect prediction compared to the simulation of the same structure performed in COMSOL Multiphysics.

Variable	Optimal configuration with full dataset	Optimal configuration with reduced dataset
$L_1 \text{ (mm)}$	100	100
L_2 (mm)	92	91
L_3 (mm)	92	91
L_4 (mm)	100	100
$d_1 \text{ (mm)}$	5	18
d_2 (mm)	44.5	21.5
d_3 (mm)	6	18
$R(k\Omega)$	278	286
Predicted Power (mW)	108.05	115.96
Simulated Power (mW)	105.59	60.99

Table 4.21: Comparison between the optimized configuration through the use of full dataset and the one that uses the reduced dataset. Power values refer to the sum of the extracted powers over the first four eigenfrequencies.

Nevertheless, it can be seen that the final identified configuration has structural similarities with the one obtained through the full dataset. In particular, the beam lengths are very similar, with only slight differences, a sign that the model still captured the most effective geometric proportions. Regarding distances (d_1, d_2, d_3) , the model clearly identified the structural trend that leads to higher power extraction: namely, the presence of well-defined central symmetry and a high value of d_2 . Although the optimized configuration cannot actually be considered optimal in terms of absolute performance, it is still a useful indication. Indeed, even with a severely reduced dataset, the model is able to identify the design direction in which to move to achieve high efficiency configurations, significantly reducing the computational effort required in the initial phase of data collection.

4.4 Validation of the Hybrid Optimization Model

4.4.1 Methodology

After obtaining the results of the optimization process proposed in the present thesis, based on the joint use of ensemble machine learning models and genetic algorithms, it is crucial to validate the actual reliability of the optimized geometric and electrical configuration. The goal is to test the applicability of the proposed method in real-world applications, in which a reduction in computational time is a key element for the adoption of advanced optimization strategies.

As already concluded in Chapter 4.1.2, the first approach cannot provide sufficient reliability. For this reason, the validation phase starts directly from the second approach.

For this purpose, a traditional optimization process based on the integration of COMSOL Multiphysics and MATLAB is implemented through the use of the LiveLink for MATLAB module. This integrated environment allows the FEM model to be automatically checked and linked to the genetic algorithm implemented in MATLAB. Again, to avoid the risk of converging to local maxima, a genetic algorithm is implemented through the ga() package of the Global Optimization Toolbox on MATLAB.

Firstly, a simplified version of the optimization is performed to verify the proper functioning of the COMSOL-MATLAB environment and the link between the genetic algorithm and FEM simulations. In this step, three of the four beam lengths are set at the values obtained from the second approach shown in Chapter 4.2.2, leaving the last length and the resistive load value as variables to be optimized.

The boundaries of these two variables are defined consistently with those used in the hybrid optimization: 45 to 100 mm for the length and 100 to 400 k Ω for the resistance. For each individual generated by the genetic algorithm, the MATLAB code modifies the geometric and electrical parameters in the COMSOL model and two subsequent studies are carried out: 1. An eigenfrequency study to identify the first eigenfrequency of the selected geometric configuration. 2. A frequency domain study to evaluate the extracted power when the excitation frequency matches the first eigenfrequency just evaluated.

The objective function is defined as the negative value of the extracted electrical power, since MATLAB ga() function performs a minimization.

Once the objective function determined, it is necessary to set the main features of the genetic algorithm such as the selection, cross-over and mutation type. Following the line of reasoning explained in Chapter 4.2.1, the same features chosen for the previously outlined genetic algorithm are also selected for this validation. The only difference is in the size of the population, since it is reduced to 10 individuals because of the high computational time required for each simulation. This value, although limiting the initial variability, could be still sufficient in this simplified configuration to ensure good evolution and acceptable convergence times.

At the end of the optimization process, the optimized configuration, the fitness history of the genetic algorithm, and the total computation time are analyzed.

The match between the obtained structure with the simplified traditional method and the one with the hybrid method confirms the correct functioning of the model presented in this section.

Following validation of the simplified process, a full optimization is performed, considering the four beam lengths and electrical resistance as variables. The operating modes remain the same: at each generation, individuals are simulated in COMSOL according to the described procedure, and the extracted power is calculated with the excitation frequency set to the first natural frequency.

In this case, to compensate for the increased complexity and number of variables, the population is increased to 20 individuals in order to enhance the population variability.

Again, at the end of the optimization, the results obtained are analyzed and compared with those of the hybrid approach both in terms of the efficiency of the configuration found and in terms of computational time and quality of convergence.

Although the ultimate goal is to validate the third approach as well, the results obtained at this stage and discussed in 4.3.2 do not yet have a level of reliability that allows direct structural comparison. However, this approach has shown a good ability to describe the general trend in structure behavior, proving useful for identifying promising regions in the solution domain. Thus, validation of the second approach remains the main benchmark for testing the effectiveness of the proposed hybrid method.

4.4.2 Numerical Results

Once the methodology to carry out the validation on the project's alternative optimization method through a traditional optimization is outlined, it is possible to discuss the obtained results. This analysis is essential to assess the effectiveness and the reliability of the hybrid methodology proposed in the thesis.

The first step is to analyze the simplified optimization outlined in Chapter 4.4.1 Knowing from the results of the second approach that the obtained optimal configuration through the hybrid method corresponds to lengths L_1 , L_2 , L_3 , and L_4 respectively equal to 100, 92, 92, 100 mm, it is initially decided to test the proper functioning of the genetic algorithm coupled with COMSOL in a simplified scenario. In fact, in this analysis, variables L_1 , L_3 , and L_4 are kept fixed at the previously mentioned values, leaving as variables to be optimized only L_2 and the resistance R.

After a total computation time of 2 hours, 10 minutes and 6 seconds, the optimization leads to the configuration shown in Table 4.22 and with a history of the objective function with respect to the generations described in Figure 4.33.

Optimized Parameter	Value
L_2	92 mm
R	310 kΩ
Extracted Power	46.4271 mW

Table 4.22: Optimization results for the simplified validation case.

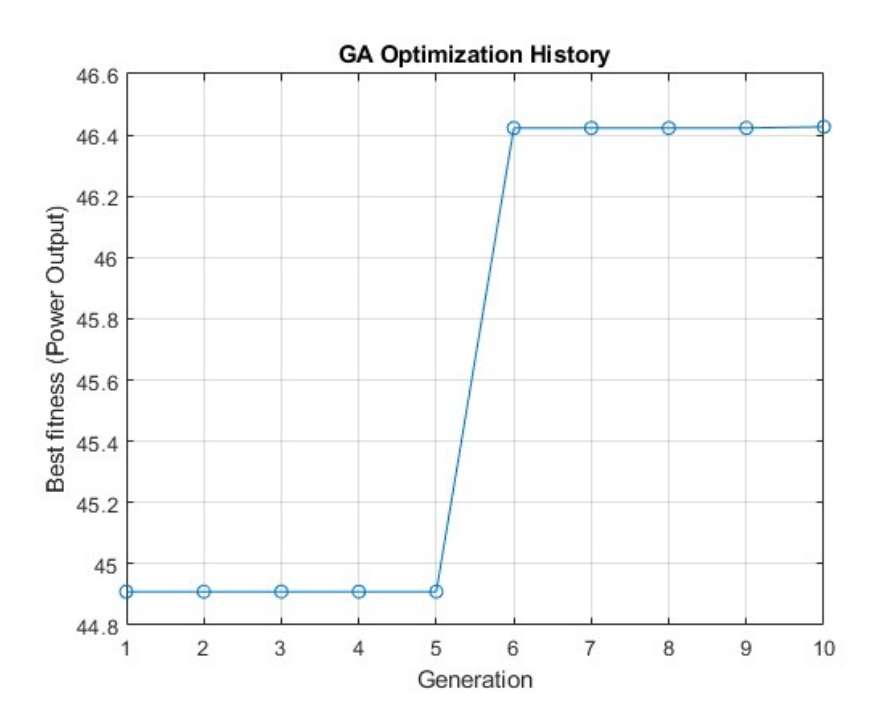


Figure 4.33: Fitness history of the simplified traditional optimization.

It is observed that the optimal length found for L_2 coincides with that identified by the hybrid method, while the resistance differs slightly: the hybrid method had identified $R = 340 \text{ k}\Omega$ (shown in Table 4.8 in Chapter 4.2.2), with a relative error of about 8.82%. As a consequence, the extracted power value is slightly higher than that obtained by the hybrid method (45,584mW), with a difference of about 1.85%.

To verify that the maximum extracted power for the 100-92-92-100 mm beam lengths configuration truly falls at the resistance value of 310 k Ω , a COMSOL simulation is carried out. A frequency domain study is performed with the excitation frequency coinciding with the first eigenfrequency and with a sweep of resistance value from 250 to 350 k Ω . The diagram showing how the extracted power varies with respect to the load resistance value is represented in Figure 4.34.

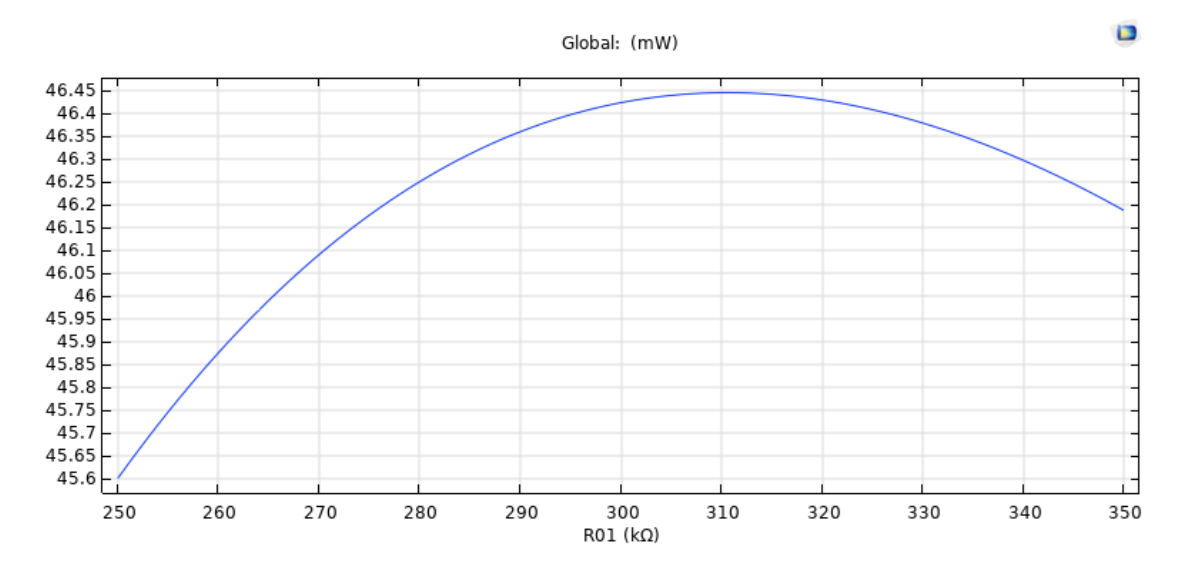


Figure 4.34: Extracted power versus resistive load diagram of the optimized structure.

From Figure 4.34, the presence of the peak extracted power at 310 k Ω is confirmed. Thanks to this, it can be concluded that the global optimization model implemented with COMSOL with MATLAB works accurately.

Subsequently, the whole structure is optimized, considering all four beam lengths and the resistive load as variables.

In a first attempt, the algorithm is run without providing as "injection" the structure already obtained in the result of the second approach optimization method. As can be observed in Figure 4.35, the optimization failed to converge naturally, but stopped when the maximum number of iteration is reached with a computational time of 11 hours, 33 minutes and 19 seconds.

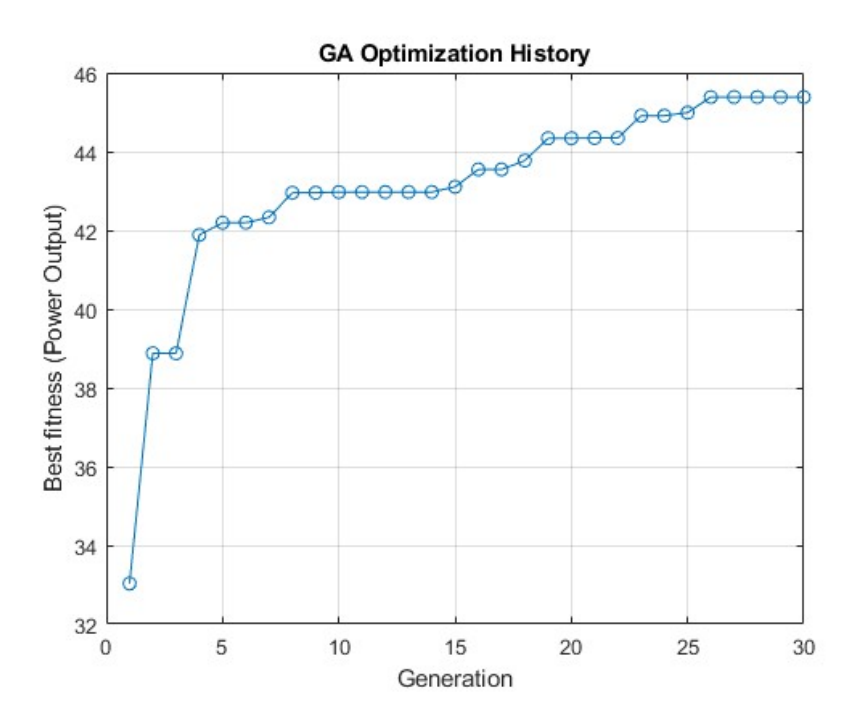


Figure 4.35: Fitness history of the traditional optimization without "injection".

The obtained result is shown in Table 4.23.

Optimized Parameter	Value
L_1	99 mm
L_2	91 mm
L_3	89 mm
L_4	99 mm
R	300 kΩ
Extracted Power	45.3838 mW

Table 4.23: Optimization results without injection of the hybrid approach solution.

As noted from Table 4.23, the power value obtained is slightly lower than that obtained from the simplified optimization and the hybrid method, confirming that the solution found does not represent the global maximum.

Analyzing the populations generated by the genetic algorithm generation after generation, there is a clear trend toward configurations similar to the known optimum (100-92-92-100). In fact, in the last few generations the individuals show central symmetry and longer extreme beams, a sign that the algorithm has identified a trend that could lead to the same solution of the hybrid approach, although without achieving convergence.

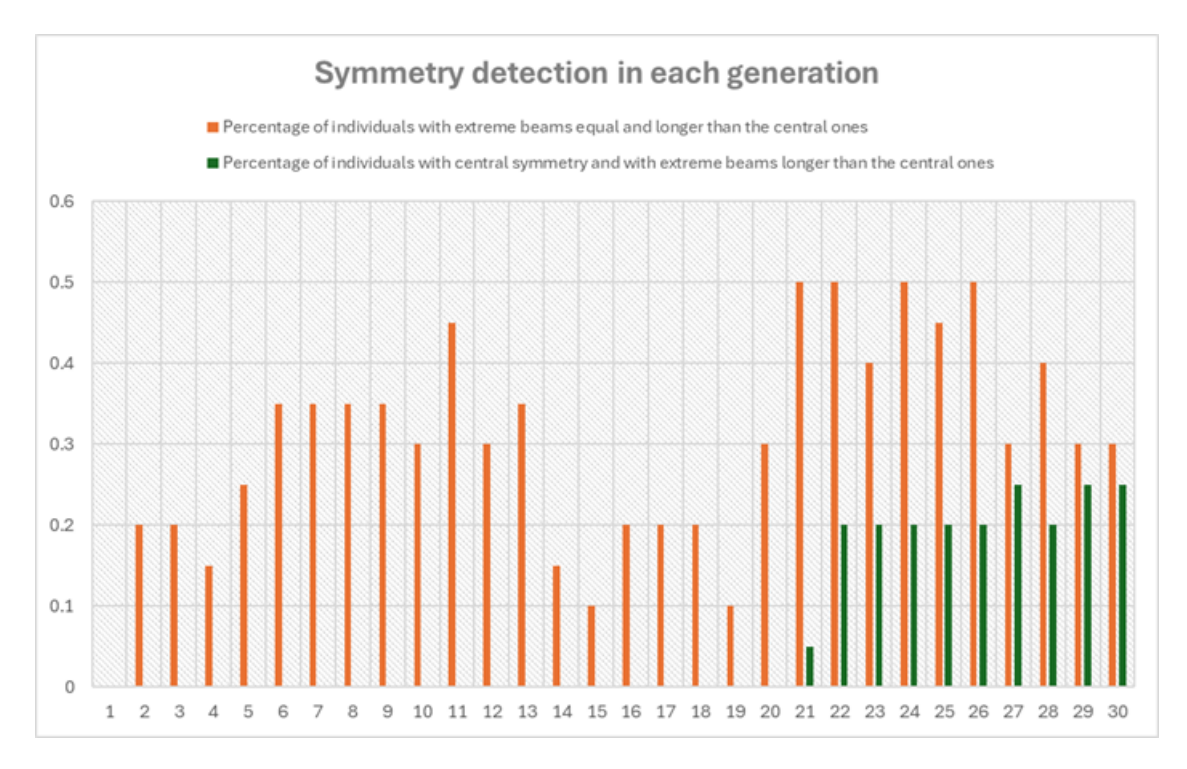


Figure 4.36: Symmetry detection in genetic algorithm generations. Horizontal axis represents the number of generation within the genetic algorithm. Vertical axis represent the percentage of symmetric individuals with respect to the total number of individuals within the generation.

This trend is illustrated in Figure 4.36, which shows the evolution of the percentage of symmetrical individuals within the population for each generation. In particular, a distinction is made between two levels of symmetry: 1. Partial symmetry, in which individuals have only the extreme beams of equal length and longer that the central beams, which are not necessarily equal to each other. 2. Complete central symmetry, in which both extreme and central beams are equal in pairs, maintaining the condition that the extreme beams are longer.

From the first to the last generation there is a gradual increase in the presence of both forms of symmetry, with a particularly marked increase in individuals showing complete central symmetry. This trend suggests that the algorithm is converging toward increasingly ordered and regular structures consistent with the solution identified by the hybrid method. This convergence is an indirect indication of the validity of the evaluation provided by the hybrid method itself.

To test whether the structure identified through the hybrid method, based on the conjugate use of machine learning and genetic algorithm, actually corresponds to a configuration close to the one that leads to the maximum extracted power, it is decided to accelerate the genetic algorithm in the traditional optimization. The idea consist on the "injection" of the solution obtained from the hybrid method at the 30^{th} generation. In addition, the maximum number of iterations is increased.

After a total optimization time of 15 hours, 34 minutes and 14 seconds, the configuration described in Table 4.24 is obtained.

Optimized Parameter	Value
L_1	100 mm
L_2	92 mm
L_3	92 mm
L_4	100 mm
R	310 kΩ
Extracted Power	46.4271 mW

Table 4.24: Optimized parameters and output power from the final traditional optimization.

This configuration exactly matches the one found through the hybrid method, except for the resistance, which has a negligible error of about 1.18% for the maximum extractable power compared to the one characterized by 340 k Ω obtained previously.

From Figure 4.37 that is the representation of the objective function versus the generations during the optimization process, it is possible to see that the maximum extracted power remains stuck at the same value after the "injection" at the 30^{th} generation. This shows that the final solution does indeed represent a global optimum.

This result confirms the reliability of the hybrid methodology, which provided the same optimal configuration in far less computational time (a few minutes on Python versus over 15 hours with COMSOL).

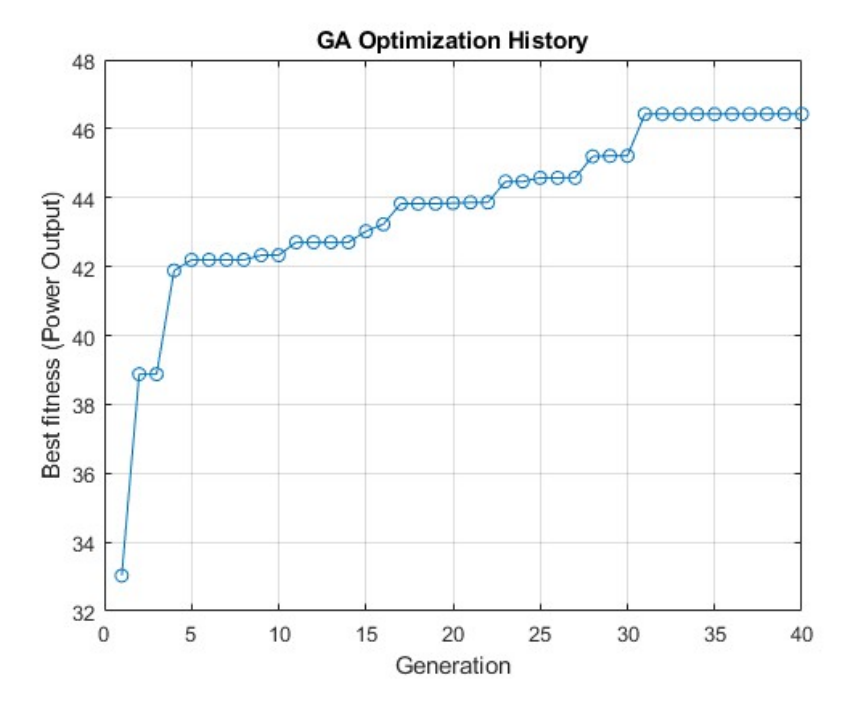


Figure 4.37: Fitness history of the final traditional optimization algorithm.

As discussed earlier, traditional optimization is not implemented to validate the third approach because of two main limitations.

The first limitation lies on the high computational cost. In fact, the change from 2 to 5 variables has already resulted in an increase in time from 2 to more than 15 hours. Increasing the number of variables to 8, including the distances d_1 d_2 d_3 between the beams, the computational time would be significantly higher. In fact, a proportional estimate suggests a time of more than 40 hours, making the process impractical.

In addition, the increase of variables has resulted in a loss in predictive accuracy, making the model more useful for identifying a general trend rather than a precise optimal configuration. Therefore, it is useless to compare the result of the third approach of the hybrid optimization with the one of the traditional optimization.

Chapter 5

Conclusion

The research and work presented in this thesis fits into the context of growing interest in energy harvesting systems, a field of study that has been gaining more and more relevance in recent years due to the need to find alternative solutions to traditional batteries. The increasing interest in this line of research is driven by two main factors. The first is the growing awareness of environmental issues related to both battery production and disposal, which is leading the scientific community to search for more sustainable and durable power sources. The other important factor is the limited lifespan of batteries. This limitation results in the constant need for periodic replacement, causing a reduction in their practicality in many applications, particularly in contexts where maintenance is costly or difficult.

Energy harvesters and piezoelectric energy harvesters (PEHs) in particular, perfectly fit in this scenario, as they represent a promising and inspiring perspective.

Over the past few years, PEHs have been widely studied and discussed in the literature. Particularly, in-depth studies have been developed to explore how the performance of such PEHs vary while changing piezoelectric materials, geometric or electric properties. However, in order to effectively implement these devices in practical applications, it is crucial to optimize them. Optimizing piezoelectric energy harvesting systems may consist of maximizing the extracted power, adapting the geometrical or electrical configuration to specific fields of application, or meeting other design requirements, depending on the context. In this direction lies the original contribution of the present thesis, the aim of which is to develop an optimization process to maximize the extracted power. The proposed process offers an alternative to traditional approaches, with the goal of significantly reducing the computational burden and time required, while maintaining a high degree of reliability.

In particular, this work proposes a hybrid optimization framework which combines machine learning techniques with genetic algorithms, applied to an experimentally validated Quad-Finger Piezoelectric Energy Harvester model. The basic idea of this approach is to take advantage of the ML prediction capability in order to estimate the electrical output as a function of geometric and operational parameters. In this way, it is possible to reduce the number of Finite Element simulations required. The ML predictions are subsequently integrated as the objective function explored by a Genetic Algorithm, with

the aim of investigating the configuration space and identifying the design that maximizes the electrical output.

The proposed process was organized into three progressive approaches, characterized by an increasing level of complexity.

A simplified dataset was considered in the first approach, featuring a reduced number of input parameters and only one output, the electrical voltage. In this case, the excitation frequency was included among the input variables to be optimized, but this proved unsuccessful. The obtained results actually indicated that the Machine Learning models are unable to reliably predict the electrical output due to huge variability induced by the frequency. The reason for this failure is that as the excitation frequency approaches the resonance frequency of the device, the extracted voltage increases sharply, while when it is far from it, the electrical output remains at low values. This enormous gap in the output made it difficult for ML models to accurately predict peak values, which are of primary interest. This highlighted a key point: it is not necessary to include frequency among the parameters to be optimized, since the focus is not on determining the resonance frequency, which is already intrinsically dependent on the geometry of the device, but rather on identifying the geometric configuration that maximizes the electrical output at its resonance.

From this awareness, the transition to the second approach was necessary. Here, the excitation frequency was excluded from the input parameters and the analyzed configurations already took into account the match with the first resonance frequency. This alternative way of creating the dataset has led the machine learning models to achieve a satisfactory reliability, with R^2 values approaching unity and extremely low MAE and MSE values, as further confirmed by the residual plots. Among the machine learning models used, Gradient Boosting Regression Trees (GBRT) emerged as the most reliable one and was therefore selected for the implementation of the genetic algorithm. Feature importance analysis also highlighted that structural symmetry (Index 1) was one of the most influential factors in power generation. This finding confirms the effectiveness of the optimization process, which led to an optimal configuration characterized by symmetrical beam lengths with respect to the center. The resulting optimal structure achieved an extracted power of 45.560 mW when subjected to an excitation frequency coinciding with its first eigenfrequency, compared to 17.603 mW for the starting configuration. "Therefore, the optimized structure delivered approximately 158% higher power output than the initial harvester design under the same base excitation, showing excellent agreement with FE-based results. To confirm the process reliability, the hybrid method optimized solution was then validated using FE-based optimization, and it demonstrated a perfect geometric match, with only one minor inconsistency related to the optimal resistance value, equal to 1.18%.

The third approach represented the final analysis for the hybrid optimization process, in which all the target input parameters and the multimodal nature of the harvester were considered. From the results of this stage, it was observed that increasing the number of input parameters to be optimized caused an exponential growth of data to provide a satisfactory level of reliability for ML predictions. This implies a proportional increase in data collection time and computation costs, which do not likewise translate to enhanced

performance. In fact, even if the dataset approximately reached 5,500 individuals, the obtained reliability was lower than in the second approach, although still at generally high levels. Differently from the second approach, according to the evaluation metrics, the multi-output ML models proved to be more reliable with respect to single-output ones. Again, the most effective model was the multi-output GBRT, subsequently integrated with the genetic algorithm. Feature importance analysis further revealed that structural symmetry (Index 1) and the central gap between the second and the third beam (d_2) are the most influential factors in power generation of the Quad-Finger harvester, with larger d_2 leading to higher output power. The genetic algorithm confirmed this evidence, identifying an optimal configuration with central symmetry and maximized gap. With this final optimization process, the increase of complexity has led to less reliable results, but nevertheless, this hybrid approach demonstrated to be capable of robustly capturing the trend and direction towards the optimal configuration. The obtained numerical results are particularly relevant: the sum of the power generated at the first four resonance frequencies of the optimized structure reached 105 mW, with a prediction error of 2.33% compared to FE simulations. This final power output, compared to 53.66 mW for the starting structure, corresponds to an increase of approximately 470%. However, as already discussed, the increase in the number of input parameters resulted in significantly longer data collection times, which partially contradicts the initial objective of the thesis, namely reducing the computational burden and time required compared to traditional optimization processes. Despite this limitation, even with reduced datasets, although at the expense of reliability, the feature importance analysis showed that machine learning models are still able to correctly identify the most relevant features.

The latter result is significant for the practical application of the proposed hybrid optimization process. In fact, it demonstrated that even at the cost of some accuracy comparable to FEM-based optimizations, the proposed process yielded a considerable time benefit, providing reliable indications on trends and promising design areas. In other words, the hybrid framework can be seen as a kind of map that allows the region of the solution space where the optimal configuration is located to be identified in a short time. Once this area has been determined, it is possible to narrow down the field and, if need be, use conventional techniques for a better analysis.

A further analysis was performed on the optimized configurations, leading to an interesting outcome from a dynamic point of view. The final harvester structure, characterized by a central symmetry and a huge central gap, is no longer characterized by four distinct modes of vibration, one for each beam, like the starting structure. On the contrary, the first four resonance frequencies turned out to be very close between each other, no longer exhibiting strongly multimodal behavior. Therefore, the optimal configuration has led to a significant increase in the extracted power, but, on the other hand, caused a reduction in the range of applicability. In fact, having a narrower frequency range of efficiency reduces the feasibility for real-world applications compared to the initial model.

This consideration opens the way for future investigations that could focus optimization not only on maximizing power, as done in this thesis, but also on adaptability to specific frequency ranges, depending on the environmental vibrations to which the device is targeted. With a view to the future, several developments can be considered to broaden the research. One possibility is to investigate how the hybrid optimization process reacts by adding new design parameters of the Quad-Finger harvester to optimize, such as the structure thickness.

Another direction for future research concerns not only from a geometric optimization perspective but also from an electrical one, i.e., piezoelectric patch position, resistance values, and circuit connections. In this case, data collection could take place not only through FEM simulations but also experimentally, completely eliminating the computational burden or allowing a direct comparison between numerical and experimental approaches.

Other developments could include the use of more advanced machine learning models, like deep neural networks, which could further improve predictive capabilities, especially in complex and multimodal scenarios.

Overall, the thesis showed how the combination of numerical simulations, machine learning techniques, and genetic algorithms is a powerful strategy to find new optimization methods. These methods have been shown to greatly reduce time of computation without sacrificing much on reliability and providing insightful information on design trends. The originality of the contribution of the research is in proposing and validating a hybrid solution to the Quad-Finger PEH that forms an adequate basis for future investigations and realizations in the engineering field of energy harvesting and generally in designing complex electromechanical systems.

Bibliography

- [1] Ieee standard on piezoelectricity. ANSI/IEEE Std 176-1978, pages 1–58, 1978.
- [2] Alexandru Agapie and Alden H. Wright. Theoretical analysis of steady state genetic algorithms. *Applications of Mathematics*, 59(5):509–525, 2014.
- [3] Charu C. Aggarwal. Outlier Analysis. Springer, 2nd edition, 2017.
- [4] J Ajitsaria, S Y Choe, D Shen, and D J Kim. Modeling and analysis of a bimorph piezoelectric cantilever beam for voltage generation. *Smart Materials and Structures*, 16(2):447, feb 2007.
- [5] Arborwind. Vertical axis wind turbines. https://arborwind.com/vertical-axis-wind-turbines/. [Accessed: 2025-03-22].
- [6] M. Askari, M. Ghandchi Tehrani, E. Brusa, A. Carrera, and C. Delprete and. Design, fabrication and evaluation of a quad-finger multimodal vibration energy harvester utilizing mfc generators. *Mechanics of Advanced Materials and Structures*, 0(0):1–21, 2025.
- [7] Mahmoud Askari. Electromechanical Modelling and Analysis of Piezoelectric Smart Structures: Energy Harvesting, Static and Dynamic Problems. PhD thesis, Politecnico of Torino, Torino, Italy, 2022. PhD in Mechanical Engineering.
- [8] Mahmoud Askari, Eugenio Brusa, and Cristiana Delprete and. Design and modeling of a novel multi-beam piezoelectric smart structure for vibration energy harvesting. *Mechanics of Advanced Materials and Structures*, 29(28):7519–7541, 2022.
- [9] ASM International. Aluminum and aluminum alloys subject guide. Accessed: 2025-06-22.
- [10] Shahriar Bagheri, Nan Wu, and Shaahin Filizadeh. Application of artificial intelligence and evolutionary algorithms in simulation-based optimal design of a piezoelectric energy harvester. *Smart Materials and Structures*, 29, 08 2020.
- [11] Satyaranjan Bairagi, Shahid ul Islam, Mohammad Shahadat, Daniel M. Mulvihill, and Wazed Ali. Mechanical energy harvesting and self-powered electronic applications of textile-based piezoelectric nanogenerators: A systematic review. *Nano Energy*, 111:108414, 2023.
- [12] Howie Baum. Energy harvesting. https://www.uc.edu/content/dam/refresh/cont-ed-62/olli/newtech2.pdf, 2021. University of Cincinnati.
- [13] Simon Bernard, Laurent Heutte, and Sébastien Adam. Influence of hyperparameters on random forest accuracy. In Jón Atli Benediktsson, Josef Kittler, and Fabio Roli, editors, *Multiple Classifier Systems*, pages 171–180, Berlin, Heidelberg, 2009. Springer Berlin Heidelberg.

- [14] S Boisseau, G Despesse, B Ahmed Seddik, et al. Small-scale energy harvesting. Electrostatic Conversion for Vibration Energy Harvesting, 2012.
- [15] Min-Chie Chiu and Ho Cheng. Optimizing efficiency of a shipâs two-magnet energy harvesting device using the cuckoo search algorithm. *Journal of Low Frequency Noise*, Vibration and Active Control, 43:1910–1938, 12 2024.
- [16] Deborah Chung. Composites get smart. Materials Today, 5:30–35, 01 2002.
- [17] Smart Material Corporation. [Accessed: 2025-03-26].
- [18] Jinxu Du, Haobin Chen, Yaodong Yang, and Wei-Feng Rao. Optimize output of a piezoelectric cantilever by machine learning ensemble algorithms. *Materials Today Communications*, 31:103688, 2022.
- [19] Tara energy. Everything you need to know about wind energy. https://taraenergy.com/blog/everything-you-need-to-know-about-wind-energy/. [Accessed: 2025-03-22].
- [20] Tara energy. Helical wind turbine. https://windcycle.energy/helical-wind-turbine/. [Accessed: 2025-03-22].
- [21] R. Fernandez Nieto. Comparison of beam theories for cross sectional deflection: Parameter analysis of euler, timoshenko and reddy beam theories. *Journal of Mechanics Research*, July 2023.
- [22] Nader Ghareeb and Mohamad Farhat. Smart materials and structures: State of the art and applications. *Nanotechnology Applications*, 1:1–5, 12 2018.
- [23] Wang Hua, Ma Cuiqin, and Zhou Lijuan. A brief review of machine learning and its application. Proceedings - 2009 International Conference on Information Engineering and Computer Science, ICIECS 2009, pages 1 – 4, 01 2010.
- [24] Jozef Jenis, Jozef Ondriga, Slavomir Hrcek, F. Brumercik, MatúÅ¡ Äuchor, and Erik Sadovsky. Engineering applications of artificial intelligence in mechanical design and optimization. *Machines*, 11:577, 05 2023.
- [25] A. Kabil. PyGAD Python Genetic Algorithm. https://pygad.readthedocs.io/en/latest/, 2025. [Accessed: 2025-04-10].
- [26] Abay I. Medeubayev A. Nurpeissova A. Adair D. Bakenov Z. Kalimuldina G., Turdakyn N. A review of piezoelectric pvdf film by electrospinning and its applications. *Sensors* (*Basel*), 09 2020.
- [27] M. E. Kiziroglou and E. M. Yeatman. Materials and techniques for energy harvesting. *Imperial College London*, UK, 17, 2013.
- [28] Ricardo A. Lebensohn and Anthony D. Rollett. Spectral methods for full-field micromechanical modelling of polycrystalline materials. *Computational Materials Science*, 173:109336, 2020.
- [29] Masoumeh Mohammadi and Insoo Sohn. Ai based energy harvesting security methods: A survey. *ICT Express*, 9(6):1198–1208, 2023.
- [30] Henry A. Sodano Mohsen Safaei and Steven R. Anton. A review of energy harvesting using piezoelectric materials: state-of-the-art a decade later (2008â2018). Smart Materials and Structures, 28, 10 2019.
- [31] Kenneth B. Lazarus Napolitano and Kevin L. Smart structures, an overview. Technical report, CSA Engineering, Palo Alto, CA 94303, 1993.

- [32] Rachael Ndung'u. Data preparation for machine learning modelling. *International Journal of Computer Applications Technology and Research*, 11:231–235, 06 2022.
- [33] Nils J. Nilsson. The Quest for Artificial Intelligence. Cambridge University Press, 2009.
- [34] Hari Mohan Pandey. Performance evaluation of selection methods of genetic algorithm and network security concerns. *Procedia Computer Science*, 78:13–18, 2016. 1st International Conference on Information Security Privacy 2015.
- [35] Jae-Hwan Park and Jae-Gwan Park. Uncertainty analysis of q-factor measurement in cavity resonator method by electromagnetic simulation. SN Applied Sciences, 2(5):996, 2020.
- [36] Rupesh Patel. Modelling analysis and optimisation of cantilever piezoelectric energy harvesters. PhD thesis, University of Nottingham, 2012. PhD in Mechanical Engineering.
- [37] Physik Instrumente (PI). Fundamentals of piezo technology. [Accessed: 2025-03-22].
- [38] E.L. Pradeesh and S. Udhayakumar. Effect of placement of piezoelectric material and proof mass on the performance of piezoelectric energy harvester. *Mechanical Systems and Signal Processing*, 130:664–676, 2019.
- [39] Philipp Probst, Anne-Laure Boulesteix, and Marvin Wright. Hyperparameters and tuning strategies for random forest. 2018.
- [40] Lior Rokach. Ensemble Methods in Supervised Learning, pages 959–979. Springer US, Boston, MA, 2010.
- [41] Mahidur Sarker, Sabariah Julai, Mohd Faizul Mohd Sabri, Suhana Mohd Said, Md Mainul Islam, and Muhammad Tahir. Review of piezoelectric energy harvesting system and application of optimization techniques to enhance the performance of the harvesting system. Sensors and Actuators A: Physical, 300:111634, 10 2019.
- [42] scikit-learn developers. sklearn.metrics: Metrics and scoring. https://scikit-learn.org/stable/api/sklearn.metrics.html, 2025. [Accessed: 2025-04-11].
- [43] Kyrillos Selim, Logina Mostafa, and Sameh Abdellatif. Machine learning-driven optimization of piezoelectric energy harvesters for low-frequency applications. *Mi*crosystem Technologies, 31:2599–2615, 05 2025.
- [44] Ralph C. Smith and Zoubeida Ounaies. A domain wall model for hysteresis in piezoelectric materials. *Journal of Intelligent Material Systems and Structures*, 11(1):62–79, 2000.
- [45] Jan G. Smits, Susan I. Dalke, and Thomas K. Cooney. The constituent equations of piezoelectric bimorphs. Sensors and Actuators A: Physical, 28(1):41–61, 1991.
- [46] N. Srivastava and G.J. Weng. A dual-phase homogenization theory for the hysteresis and butterfly-shaped behavior of ferroelectric single crystals. *Mechanics of Materials*, 38(8):945–957, 2006. Advances in Disordered Materials.
- [47] Deliang Sun, Haijia Wen, Danzhou Wang, and Jiahui Xu. A random forest model of landslide susceptibility mapping based on hyperparameter optimization using bayes algorithm. *Geomorphology*, 362:107201, 04 2020.

- [48] Rujie Sun, Qinyu Li, Jianfei Yao, Fabrizio Scarpa, and Jonathan Rossiter. Tunable, multi-modal, and multi-directional vibration energy harvester based on three-dimensional architected metastructures. *Applied Energy*, 264:114615, 2020.
- [49] Richard S. Sutton and Andrew G. Barto. Reinforcement Learning: An Introduction. MIT Press, Cambridge, Massachusetts, second edition, 2018. https://web.stanford.edu/class/psych209/Readings/SuttonBartoIPRLBook2ndEd.pdf.
- [50] R.M. Toyabur, M. Salauddin, and Jae Y. Park. Design and experiment of piezoelectric multimodal energy harvester for low frequency vibration. *Ceramics International*, 43:S675–S681, 2017. The 10th Asian Meeting on Electroceramics (AMEC-10).
- [51] Tpoint Tech. Machine learning decision tree classification algorithm. https://www.tpointtech.com/machine-learning-decision-tree-classification-algorithm, 2025. [Accessed: 2025-04-16].
- [52] Luigi Tresca. Basics of machine learning for hybrid electric vehicles, 2024. Hybrid and Electric vehicles, Politecnico of Torino.
- [53] U.S. Environmental Protection Agency. Exploratory data analysis. https://www.epa.gov/caddis/exploratory-data-analysis. [Accessed: 2025-05-22].
- [54] Vittorio Verda. Introduction to optimization in energy engineering, 2024. Energy Department (DENERG), Politecnico of Torino.
- [55] Zhengbao Yang, Shengxi Zhou, Jean Zu, and Daniel Inman. High-performance piezo-electric energy harvesters and their applications. *Joule*, 2(4):642–697, 2018.
- [56] Xue Ying. An overview of overfitting and its solutions. *Journal of Physics: Conference Series*, 1168(2):022022, feb 2019.
- [57] Chengyun Zhang, Gang Hu, Pengfei Lin, Shanghao Gu, Song Dongran, H.Y. Peng, and Junlei Wang. Machine learning based prediction of piezoelectric energy harvesting from wake galloping. *Mechanical Systems and Signal Processing*, 160:107876, 11 2021.
- [58] A. Zheng and A. Casari. Feature Engineering for Machine Learning: Principles and Techniques for Data Scientists. O'Reilly Media, 2018.